AD-A062 257   RAYTHEON CO SUDBURY MASS EQUIPMENT DIV   F/G 17/7
MULTIOSCILLATOR RING LASER GYRO.(U)
SEP 78 A ZAMPIELLO, D PASIK   F33615-76-C-1218
UNCLASSIFIED   AFAL-TR-78-133   NL

1 OF 2
AD
A062257

AFAL-TR-78-133

MULTIOSCILLATOR RING LASER GYRO

RAYTHEON COMPANY
EQUIPMENT DIVISION
528 BOSTON POST ROAD
SUDBURY, MASSACHUSETTS 01776

SEPTEMBER 1978

TECHNICAL REPORT AFAL-TR-78-133
Final Report for Period May 1976 – January 1978

AIR FORCE AVIONICS LABORATORY
AIR FORCE WRIGHT AERONAUTICAL LABORATORIES
AIR FORCE SYSTEMS COMMAND
WRIGHT-PATTERSON AIR FORCE BASE, OHIO 45433

NOTICE

When Government drawings, specifications, or other data are used for any purpose other than in connection with a definitely related Government procurement operation, the United States Government thereby incurs no responsibility nor any obligation whatsoever; and the fact that the government may have formulated, furnished, or in any way supplied the said drawings, specifications, or other data, is not to be regarded by implication or otherwise as in any manner licensing the holder or any other person or corporation, or conveying any rights or permission to manufacture, use, or sell any patented invention that may in any way be related thereto.

This report has been reviewed by the Information Office (OI) and is releasable to the National Technical Information Service (NTIS). At NTIS, it will be available to the general public, including foreign nations.

This technical report has been reviewed and is approved for publication.

David W. Pleva

DAVID W. PLEVA
Project Engineer
Reference Systems Technology Group

Ronald L. Ringo

RONALD L. RINGO, Chief
Reference Systems Branch
Reconnaissance & Weapon Delivery Div.

FOR THE COMMANDER

R E Deal

R. E. DEAL, Asst Chief
Reconnaissance and Weapon
Delivery Division

"If your address has changed, if you wish to be removed from our mailing list, or if the addressee is no longer employed by your organization please notify AFAL/RWA *,W-PAFB, OH 45433 to help us maintain a current mailing list".*

Copies of this report should not be returned unless return is required by security considerations, contractual obligations, or notice on a specific document.

AIR FORCE/56780/1 December 1978 — 100

UNCLASSIFIED

This is for publication in report

SECURITY CLASSIFICATION OF THIS PAGE (When Data Entered)

⑲ **REPORT DOCUMENTATION PAGE**		READ INSTRUCTIONS BEFORE COMPLETING FORM
1. ~~REPORT NUMBER~~ ⑱ AFAL-TR-78-133	2. GOVT ACCESSION NO.	3. RECIPIENT'S CATALOG NUMBER
4. ~~TITLE (and Subtitle)~~ ⑥ Multioscillator Ring Laser Gyro.		5. ~~TYPE OF REPORT & PERIOD COVERED~~ ⑨ Final Technical Report, May 76-Jan 78,
		6. PERFORMING ORG. REPORT NUMBER
7. AUTHOR(s) ⑩ Allen Zampiello Donald Pasik		8. CONTRACT OR ~~GRANT NUMBER(s)~~ ⑮ F33615-76-C-1218
9. PERFORMING ORGANIZATION NAME AND ADDRESS Raytheon Corp. Equipment Division 528 Boston Post Road Sudbury, MA 01776		10. PROGRAM ELEMENT, PROJECT, TASK AREA & WORK UNIT NUMBERS PE62204F ⑯ 6095-11-02 ⑰ 11
11. CONTROLLING OFFICE NAME AND ADDRESS Air Force Avionics Laboratory (RWA) Air Force Systems Command Wright-Patterson AFB, OH 45433		12. REPORT DATE ⑪ September 1978
		13. ~~NUMBER OF PAGES~~ 138
14. MONITORING AGENCY NAME & ADDRESS (if different from Controlling Office) ⑫ 149p.		15. SECURITY CLASS. (of this report) Unclassified
		15a. DECLASSIFICATION/DOWNGRADING SCHEDULE

16. DISTRIBUTION STATEMENT (of this Report)

Approved for public release, distribution unlimited.

17. DISTRIBUTION STATEMENT (of the abstract entered in Block 20, if different from Report)

18. SUPPLEMENTARY NOTES

19. KEY WORDS (Continue on reverse side if necessary and identify by block number)

Ring Laser
Multioscillator

20. ABSTRACT (Continue on reverse side if necessary and identify by block number)

The reported study developed information on design and fabrication methods peculiar to the multioscillator (four-frequency) ring laser gyro, with study emphasis on ~~(1)~~ gyro cavity sealing problems, and ~~(2)~~ gain medium characterization. Sealing methods were studied for attachment of anode pins, cathode, and pumpout to the Cer-Vit block. With reasonably cautious procedures, a tri-metal metalization of the Cer-Vit, with pure tin solder, was found to be adequate. Experiments and analytic procedures were used to characterize the

→ next page

DD FORM 1473 1 JAN 73 EDITION OF 1 NOV 65 IS OBSOLETE

UNCLASSIFIED

SECURITY CLASSIFICATION OF THIS PAGE (When Data Entered)

1B

405 037

79 12 07 043

Block 20: ABSTRACT (Continued)

AC small signal behavior of the gain medium in terms of equivalent electronic circuits. This was done successfully for specific cases, but more work is needed to relate model parameters to actual gain medium parameters. Other experiments were done to relate power output and stability to various cavity parameters. An analysis was performed relating thermal effects and Fresnel-Fizeau drag as an error source. Verification data was taken on a particular ring laser gyro, showing scale factor linearity of 0.6 ppm, random drift of 0.003ϕ/hour ½, and turn-on repeatability of 0.05ϕ/hour.

deg deg

Preface

This final report describes work performed by Raytheon Company under contract F33615-76-C-1218 (Multioscillator Ring Laser Gyro). The work was performed under the cognizance of Raytheon's Equipment Division (ED) with contributions from the Research Division (RD) and Microwave and Power Tube Division (M&PTD) as indicated below. Responsibility for writing and/or coordinating the various sections of this report was assigned to the individuals named below.

1.	J. B. Matthews (ED)
2.	J. B. Matthews (ED)
3.	W. Prifti (ED)
4.1	R. Dyer (M&PTD)
4.2	A. Zampiello/M. Perlmutter (ED)
4.3	I. Smith (RD)
5.1	I. Smith (RD)
5.2	D. Pasik (ED)
6.	D. Pasik (ED)

TABLE OF CONTENTS

TABLE OF CONTENTS (Cont'd)

LIST OF ILLUSTRATIONS

LIST OF ILLUSTRATIONS (Cont'd)

LIST OF ILLUSTRATIONS (Cont'd)

LIST OF ILLUSTRATIONS (Cont'd)

SECTION 1

INTRODUCTION AND BACKGROUND

1.1 INTRODUCTION

This report details the efforts and results achieved by Raytheon in performance of the Multioscillator Ring Laser Gyro technology development contract to the Air Force Avionics Laboratory, Wright-Patterson Air Force Base. The results have been tested in particular application to the Raytheon multioscillator ring laser gyro design. For convenient reference, the design considerations for multioscillator (four-frequency) laser gyros are compared below (Section 1.2) with the two-frequency design. In Section 2, further design details for the Raytheon RB-25 Multioscillator Gyro are presented. The work performed under contract is described in detail in Sections 3, 4, and 5. Section 3 describes methods developed and tested for sealing mirrors and electrical components to the gyro cavity block. Section 4 describes the gain medium investigation, including cathode development work, gain medium characterization in terms of equivalent electronics components, and power parametrization. Section 5 describes other design considerations, including readout optics and gyro output stability as influenced by thermal and magnetic effects. Finally, sample performance data for the Raytheon gyro, incorporating these methods, are presented in Section 6.

1.2 BACKGROUND

Since the ring laser gyroscope is basically a solid state sensor, with no moving parts to achieve inertial sensing capability, it has great potential for widespread application.

Further, since the device is inherently rugged and has a wide dynamic range it lends itself ideally to strapdown or gimballess mechanizations. Strapdown guidance and navigation implementations are now currently technically feasible and should be less costly than the mechanical isolation approaches normally required by the "rotating mass" instruments.

Extensive strapdown system study and testing work has been accomplished at Raytheon which is applicable to the more conventional gyro sensors as well as its own ring laser gyro. These studies included the development of algorithms for alignment, erection, calibration, and dynamic filtering typical of modern inertial system applications. Verification of the accuracy and the validity of these algorithms has been shown in the testing of two different strapdown systems in both the laboratory and a company-owned mobile van.

The first system involved an early vintage ring laser triad coupled with a digital navigation computer while the second system was a strapdown version of conventional single degree of freedom floated gyros in a three-axis inertial measurement unit similarly interfaced with the digital navigation computer. Over 10,000 hours of mobile testing provided early indications of good performance potential for strapdown systems.

Currently two fundamental laser gyro mechanizations are under very active development. The first and most mature implementation is designated as the dithered or two-frequency approach. Numerous organizations are actively pursuing the refinement of this technique and considerable test data has been published to show much progress to date. The second basic approach called the multioscillator or four-frequency ring laser gyro is a relatively new development but has the promise of high accuracy potential and appears to be ideally suited to monolithic multiaxis redundant sensor configurations anticipated in future applications. Each of these gyro approaches is discussed later but of most interest here are the technology efforts described in this report which are primarily aimed at solutions to the problems related to life, reliability, accuracy potential, and the fabrication and processing of the Raytheon four-frequency gyro.

1.2.1 CHARACTERISTICS OF RING LASER GYROS

As of this date many of the desired performance characteristics in inertial system have not been attained to the degree desired. These include:

- Inertial grade performance, but low cost
- Mechanical simplicity and small size
- Digital output
- High dynamic range
- Instant reaction
- Low power
- Flexible form factor
- High "g" environment
- Reliability - low life cycle cost.

The need for a reliable, small and low cost unit can be satisfied by the development of new instrument technology such as the laser gyro which eliminates the need for complex mechanical subsystems peculiar to current operational systems. Through the development and refinement of strapdown inertial techniques, the mechanical gimbals, slip rings and torque motors of inertial platforms can now be reliably replaced by inexpensive computational capability. Accelerometers are being improved and simplified. Finally, and most importantly, the promising advances in laser gyro technology make it apparent that a strapdown inertial measurement unit (IMU) containing laser gyros can be developed with performance comparable to conventional, gimballed inertial platform systems. The inherent simplicity of the laser gyro promises breakthroughs in both cost and reliability. The development of a laser gyro with size, cost and performance comparable to mechanical instruments can, therefore, have a decisive effect on the realization of a low cost inertial system having the desired characteristics.

The solid state laser gyro has many advantages. Being inherently a digital device, it is ideally suited to strapdown applications. In addition, since it has no moving parts and its sensitivity is derived from rotating light, it has essentially no "g" sensitivity thereby avoiding the necessity for complicated computational g-related unbalance compensations. This "g" insensitivity minimizes a major error source in computing "miss distance" in any navigation or guidance system.

The laser gyro also has a wide dynamic range, being essentially linear from 0 to greater than 600 degrees per second, and may provide both angle and angular rate outputs. These characteristics make it suitable for multipurpose use on missiles, such as midcourse guidance, tracking head stabilization and autopilot functions, thereby replacing several other conventional instruments normally required for these individual functions.

Other key features of the laser gyro are its low power and low thermal environment sensitivity. The need for temperature control elements is eliminated. This fact, coupled with the gyro's low operating power, reduces power supply requirements which further reduces system size, weight and cost. The elimination of any thermal control for the gyro means that it is essentially an "instant on" device, providing useful output information immediately, making it ideally suited for fast reaction time applications.

The degree to which current laser gyro approaches have the potential for meeting the goals and requirements of future inertial systems is believed to be dependent on the approach taken. Raytheon is convinced that highest accuracy potential, fastest self-alignment time and most rapid transfer alignment characteristics will be provided by the low noise ring laser sensor. The design goals of the Raytheon RB-25 gyro and its derivatives are aimed at optimizing this low noise characteristic.

1.2.2 THE TWO-FREQUENCY GYRO

A laser gyroscope consists of a medium with gain located in a ring resonator, as shown in Figure 1-1. Such a combination can oscillate with a traveling wave going around the ring in a clockwise (CW) and counterclockwise (CCW) direction. In the absence of rotation of the structure, these two waves oscillate at identical frequencies and so is called a two-frequency gyro. When the structure rotates about an axis perpendicular to the figure the two frequencies become different, the difference being proportional to the rotation rate.

At low frequency differences (low angular rate) the two waves tend to remain locked at a common frequency because the system behaves as two coupled oscillators. This phenomenon is usually referred to as lock-in. It causes loss of information at low roation rates and departure from linearity outside the range of lock-in.

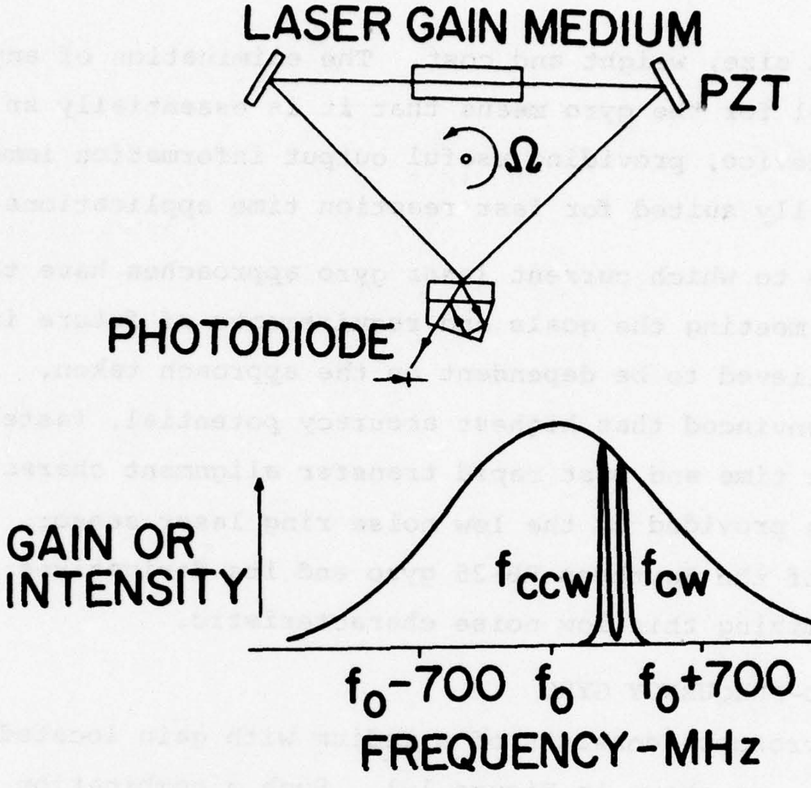

$$\Delta f = f_{CW} - f_{CCW} = \frac{4A\Omega}{L\lambda}$$

Figure 1-1 Two-Frequency Laser Gyro

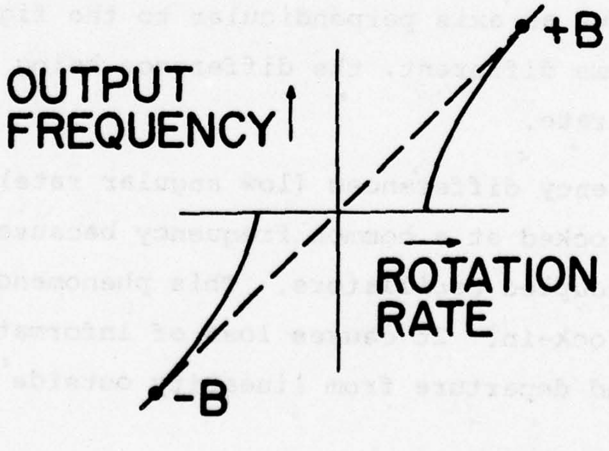

Figure 1-2 Bias Switching through Lock-In

There are two common practices used to avoid this lock-in. One is to angularly dither the gyro cavity about the input axis relative to the case. The second is to optically bias the gyroscope in such a way that the two frequencies are unequal in the absence of rotation. In this second approach any drift in bias will be interpreted as a rotation rate, and it is necessary to switch (periodically dither) between two bias points (+B and -B in Figure 1-2). If this switching takes place in a completely symmetric way any drift in the bias averages to zero as in the mechanically dithered case. Because of the gyro output's forced transition through the "lock-in" region, required by both approaches, some angular information is lost, causing a noise source to be introduced into the output.

The gyro output is usually obtained by simply counting the output beat frequency. As this is essentially a process of integration, each cycle represents an incremental change in input angle, and the sum will represent the angle the instrument has been rotated through since the counting process was initiated. The relationship of a cycle of the output frequency to a change in angle is the instrument's "scale factor" and may be derived from the expression in Figure 1-2. Frequency jitters or pulses lost due to transition through lock-in will therefore be interpreted as angular disturbances.

The importance of this noise source is at first not obvious but if considered, reveals that a laser gyro mechanized in a way that requires transitions through this region, results in an instrument incapable of realizing the potential of the very narrow line width (or high beat frequency stability) of the laser cavity. It is possible to construct a gyro cavity having a Power Spectral Density of beat frequency fluctuations of the order of 1×10^{-6} Hz^2/Hz

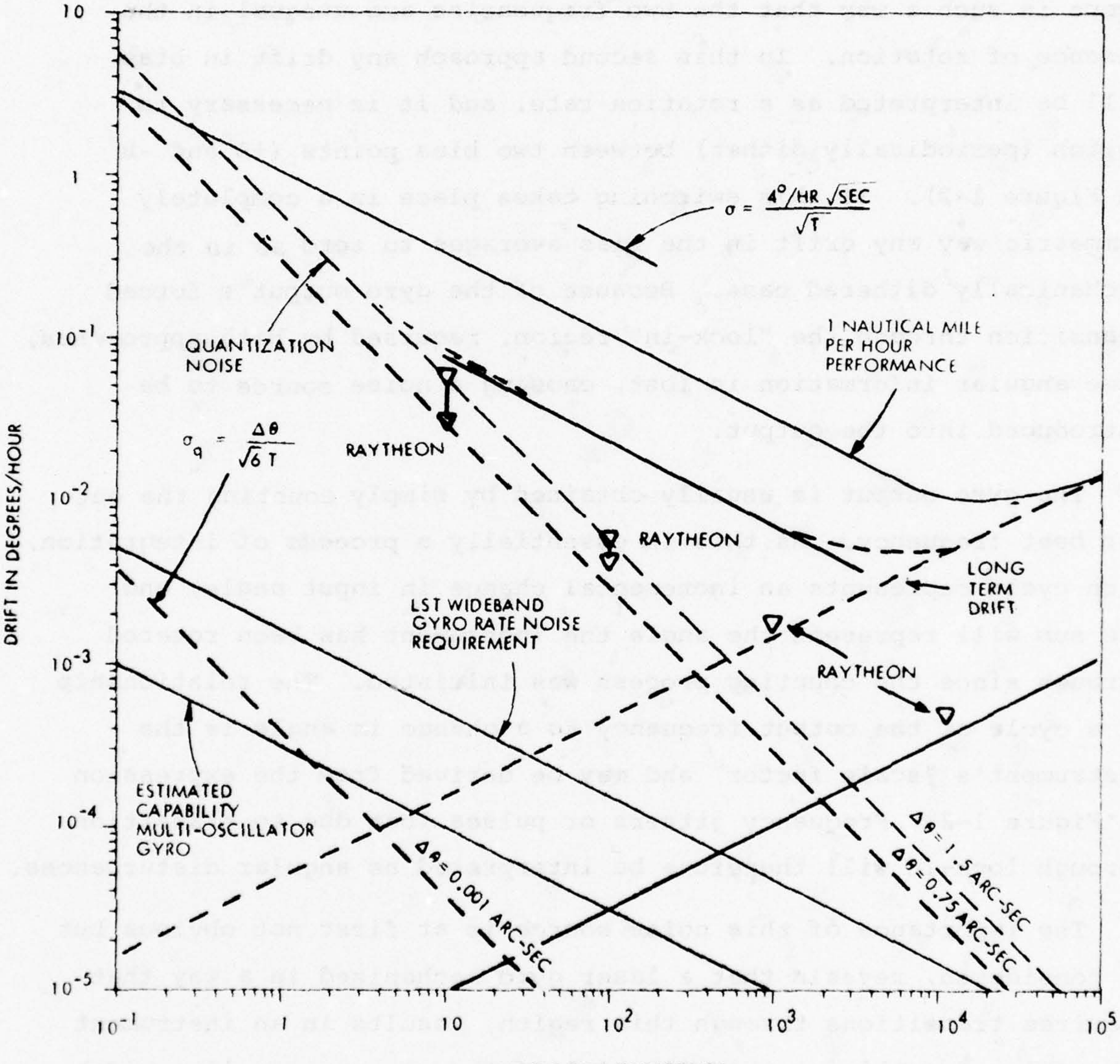

Figure 1-3 Standard Deviation of Rate Measurement as a Function of Sample Time

whereas dithering the same cavity will increase noise resulting from transition through lock-in that is typically of the order of 1×10^{-2} Hz^2/Hz or greater.

This wide band noise phenomenon increases with the square as the size of the gyro diminishes. This is primarily true because the output pulse size (angular quantization) is inversely proportional to the ring size thus changing both the effective size of the deadband and the value of the pulse. The effect of the noise on navigation, alignment and gyrocompassing is to limit accuracy and increase the alignment time for a given accuracy.

In Figure 1-3 these considerations are illustrated. The figure represents "gyro drift" in terms of the standard deviation of estimates of gyro output rate derived by simply summing output cycles for a period of time and computing:

$$\dot{\theta} = \frac{1}{\Delta\theta} \Sigma \Delta\theta$$

where θ is the rate estimate, ΔT is the sample time, $\Sigma \Delta\theta$ is the sum of the gyro output pulses. The curves can apply equally well to a dynamic situation in which the actual rate is zero or some known rate. The figure is used to illustrate the verification of gyro error models and to relate gyro drift requirements to system performance.

In order to calculate predicted system performance for a particular application, a gyro error model must be available for the sample time (that is, bandwidth) of interest. Analysis of the various error causing mechanisms of the gyro leads to postulated statistical error models that specify the gyro error growth in equations suitable for use in system simulations to predict performance. Before such error models can be used with confidence, they should be verified by gyro testing. This can be accomplished by examining the behavior of actual gyro test data as a function of sample time (ΔT). Figure 1-3 is useful to illustrate this process. Types or sources of gyro drift considered are:

- Wide Band Noise, with $1/\sqrt{\Delta T}$ behavior typical of the dithered gyro, and also other frequency fluctuations.
- Pulse Quantization Noise, with $1/\ \Delta T$ behavior.
- Long term drift, with $\sqrt{\Delta T}$ behavior due to thermal and other long term drift sources.

Shown also are the curves representing the requirement for one nautical mile per hour performance, and the requirement for precision pointing of the Large Space Telescope (LST) program.

Although compensation techniques or new methods for minimizing the output switching transient inherent in any dithered instrument can improve a two-frequency gyro's performance, the capability of this approach for meeting the most stringent performance requirements is questionable.

1.2.3 MULTIOSCILLATOR OR FOUR-FREQUENCY GYRO

In the Raytheon multioscillator approach, the low rate lock-in problem is avoided by employing cavity and bias techniques which rely on maintaining circular polarization of the oscillating laser light beams. In addition, the bias technique is passive so that the gyro rate measurement becomes insensitive to any drift in that bias, as will be discussed.

Raytheon has proven the feasibility of an alternate mode of ring laser gyro operation, in which the application of a fixed magnetic bias leads to cavity oscillation at four different frequencies and yields a four-frequency gyro. These oscillations occur in traveling waves of two mutually orthogonal polarizations, one frequency at each polarization traveling around the ring in a clockwise direction, and one of each polarization traveling in a counterclockwise direction.

With the appropriate read-out system a signal can be obtained from this four-frequency gyroscope, the frequency of which is proportional to rotation rate. This frequency is also insensitive to bias instabilities and bias drifts, making the switching of bias polarity as used in two-frequency gyroscope unnecessary.

A description of the device as it was first implemented follows. We start with a ring laser geometry which places no constraints on the polarization of the traveling waves which can oscillate. In the absence of any bias or rotation all polarizations are equivalent, and only one frequency can oscillate.

A fourth mirror or reflecting surface is added to the resonator path of the two-frequency gyro system to provide an even number of light reflections and insure that there is no net phase reversal in traversing the cavity path.

Then we place an element in the ring which has rotary birefringence such as properly oriented crystalline quartz. See Figure 1-4. The birefringence uniquely polarizes the light into orthogonal components. This means that the ring now had a different length for a light wave of right-hand circular polarization (RHCP) than

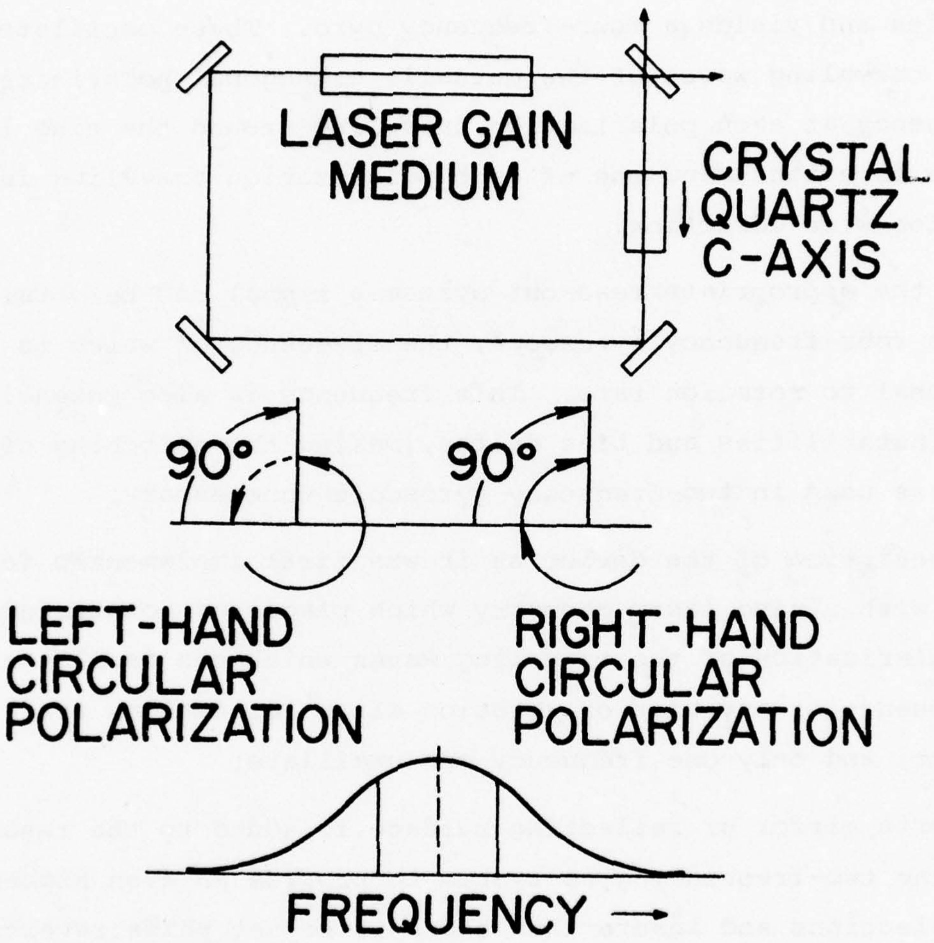

Figure 1-4 Multioscillator Ring Laser Gyro

for a light wave of left-hand circular polarization (LHCP). The result is that the ring can now sustain oscillation of circularly polarized modes only and the frequencies of RHCP and LHCP are different by an amount determined by the birefringence and size of the quartz.

Subsequently a Faraday rotator is added to the ring as shown in Figure 1-5. Its function is to remove the frequency degeneracy between the circular polarization traveling CW and CCW. With a fixed magnetic field applied, the frequency spectrum now consists of four frequencies as indicated. We now monitor the frequency

$$\Delta f = (f_4 - f_3) - (f_2 - f_1)$$

It can be readily proven that this frequency can be expressed as

$$f = \frac{8A}{\lambda L} \cdot \omega$$

The attractive feature of this approach is that neither the bias provided by the rotary birefringence nor the bias introduced by the Faraday rotator enter into this quantity, and no bias drifts are of importance. Furtherm[illegible]k-in which exists in two-frequency laser gyros will occur when $(f_4 - f_3)$ and $(f_2 - f_1)$ approach zero. With proper choice of components this can be made to occur at very high rotation rates, which is not usually a problem.

A typical embodiment of the gyro device is shown in Figure 1-6. Similar laboratory units have been used to demonstrate that output noise is significantly lower than in the classic dithered approaches

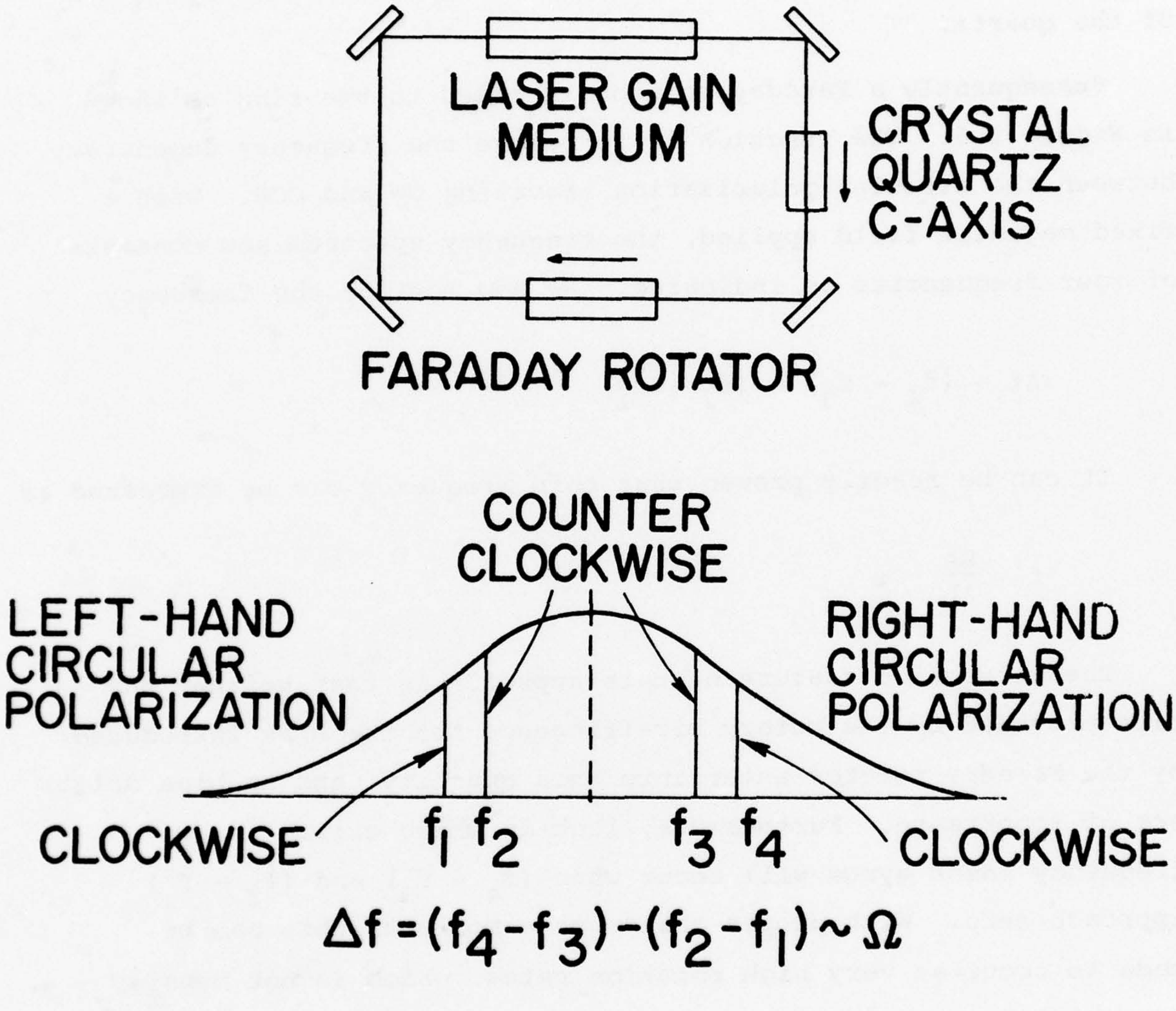

Figure 1-5 Multioscillator Ring Laser Gyro

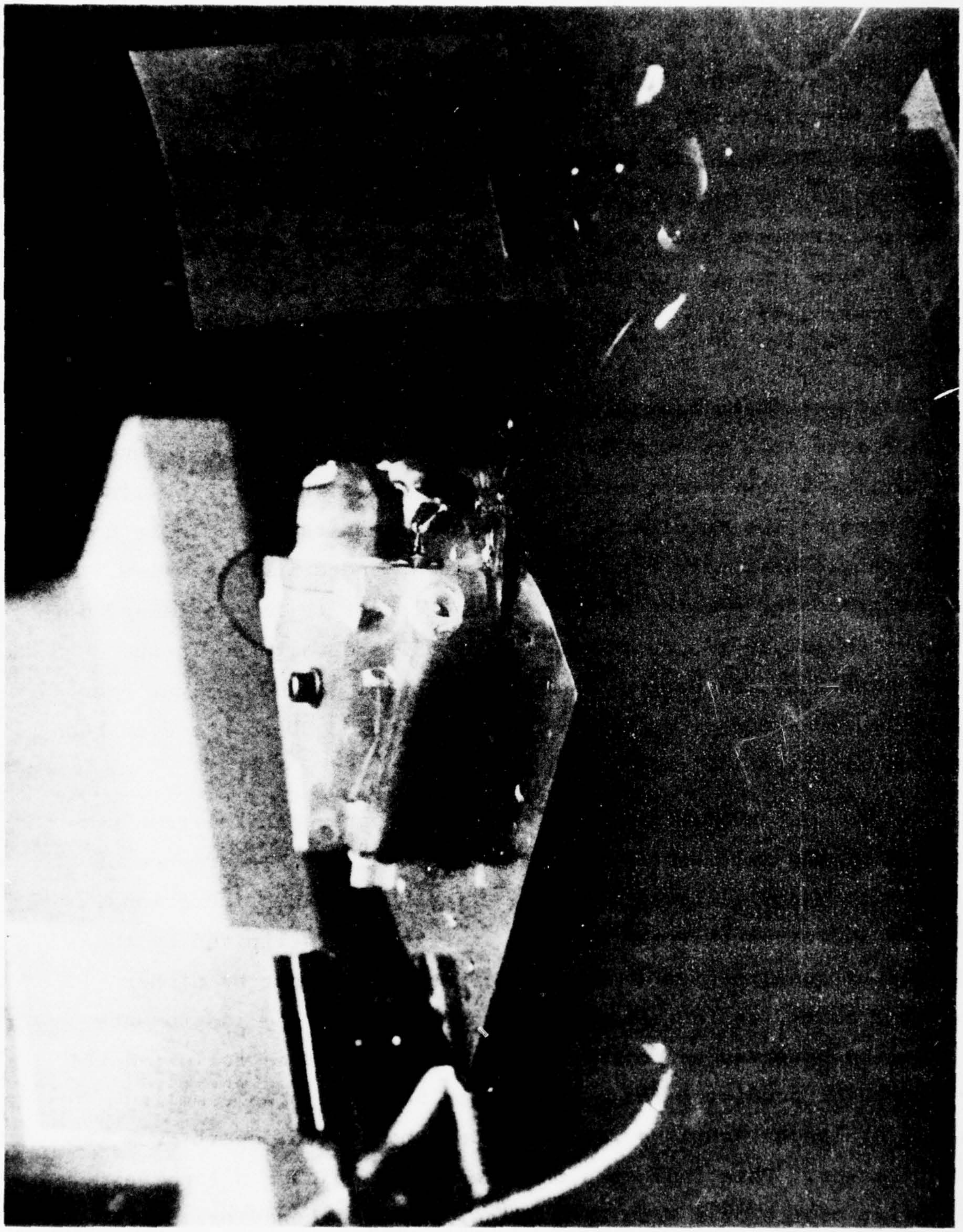

Figure 1-6 Multioscillator Ring Laser Gyro Cavity

to lock-in avoidance. Analysis and data have shown that the gyro noise is (as predicted) proportional to 1/t (where t is the sampling or summing interval), is limited by quantization. This quantization limitation can be reduced by external electronics to meet special system requirements such as for a high performance stabilization system. This data is summarized in Figure 1-7. The dashed lines in the lower left hand corner represent quantization recently achieved.

The Raytheon Multioscillator Gyro output frequency versus input rotation rate data is compared to data from a typical two-frequency gyro cavity at low rotation rates, Figure 1-8. The superior linear performance of the multioscillator through zero rate should be noted. The rectangle near zero rotation rate is expanded in Figure 1-9. Here data is presented showing that this fine linearity is maintained down to rates as low as 1/3 degrees per hour. The data taken in the region marked by the dashed lines (i.e., below one degree per hour) is limited in accuracy by the test table. No deadband has ever been observed at these low rates.

Figure 1-3 summarizes the data and compares the relative performance of the multioscillator gyroscope with the performance of the two-frequency dithered instrument for various configurations. The data indicates that the Raytheon instrument is limited by the gyro output quantization (a design parameter) and not by dither generated noise, as is the case for the two-frequency instruments. This can be observed by noting that the gyro noise is following the $1/\Delta T$ behavior predicted for quantization noise at high sampling rates. At longer sampling rates the data begins to depart from the $1/\Delta T$ behavior. This indicates the presence of either a long term $\sqrt{\Delta T}$ drift source or a Wide Band Noise, $(1/\sqrt{\Delta T})$ behavior, due to

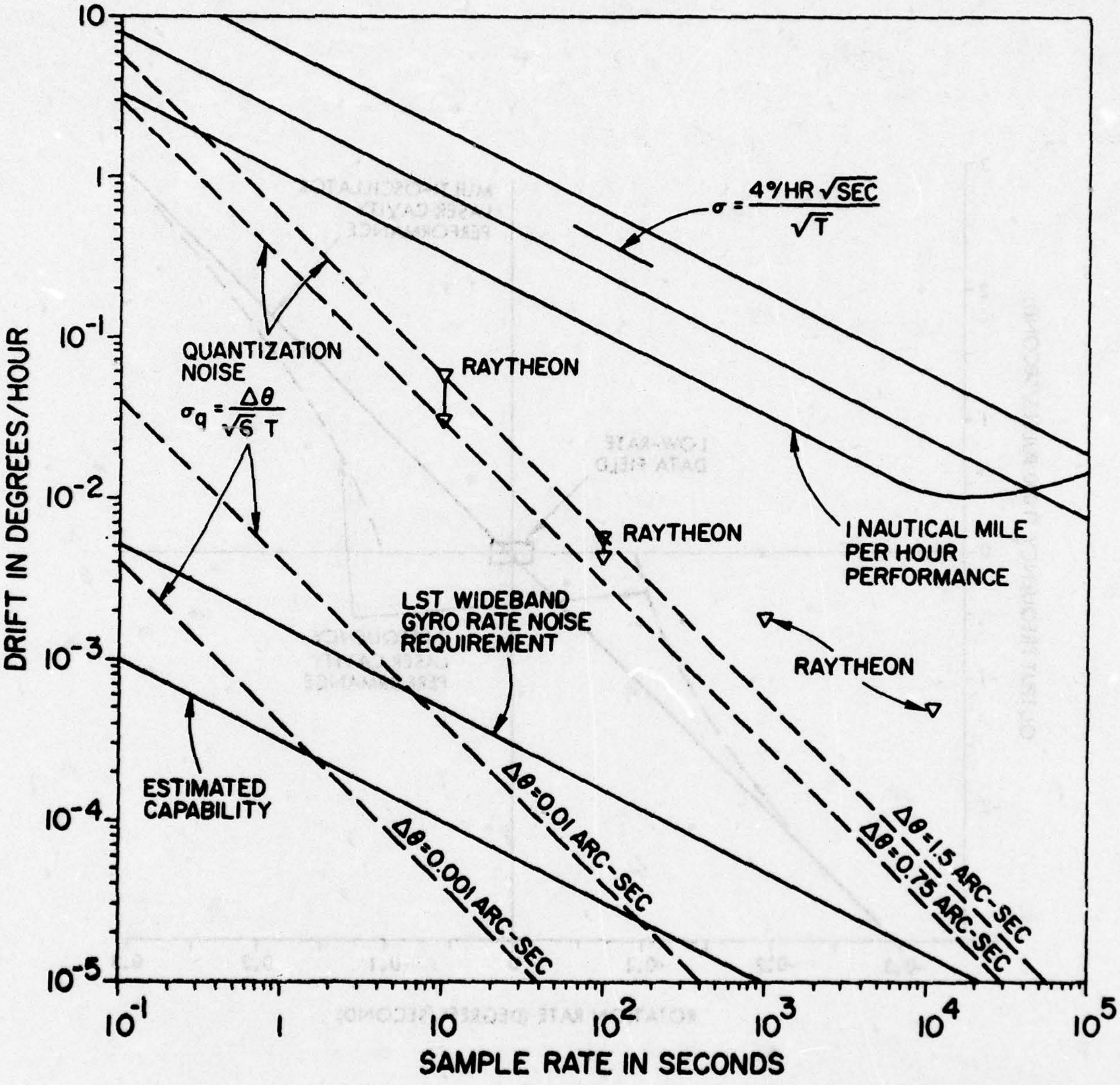

Figure 1-7 Standard Deviation of Rate Measurement as a Function of Sample Time

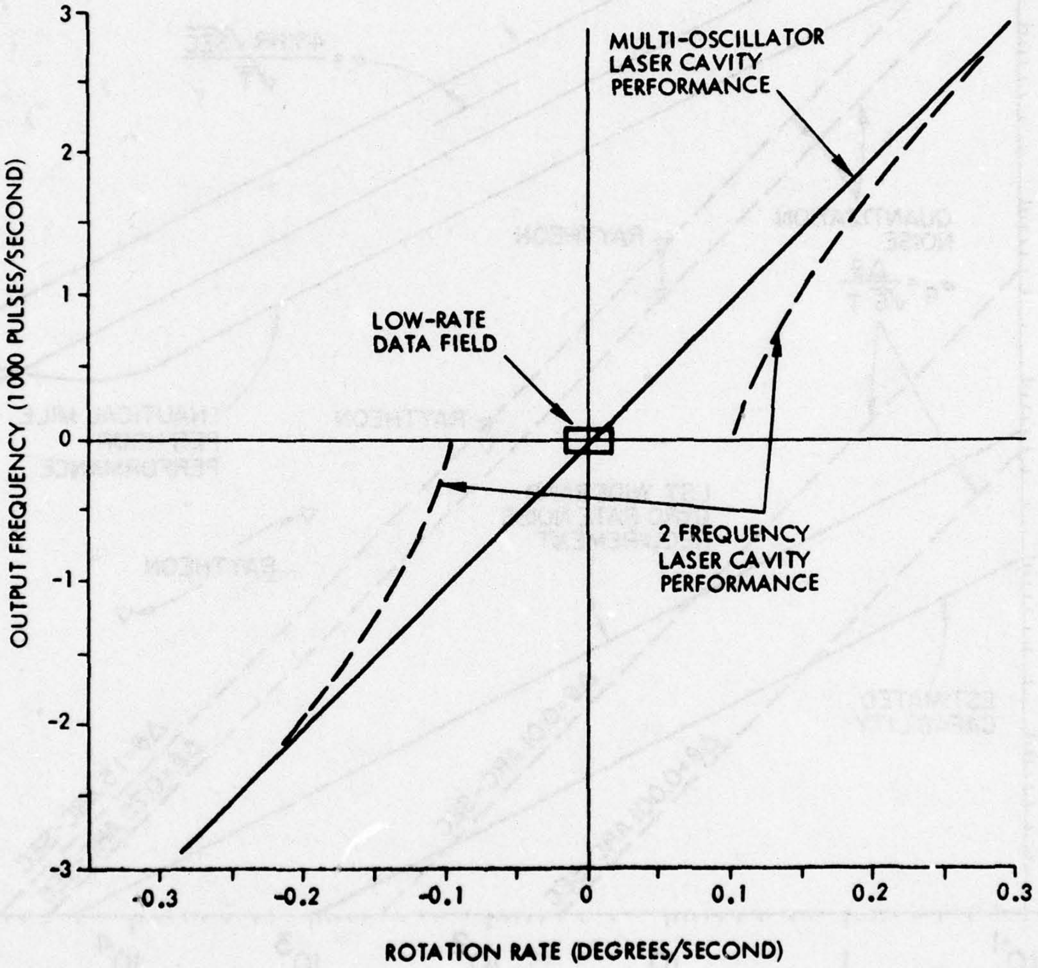

Figure 1-8 Output Frequency versus Rotation Rate

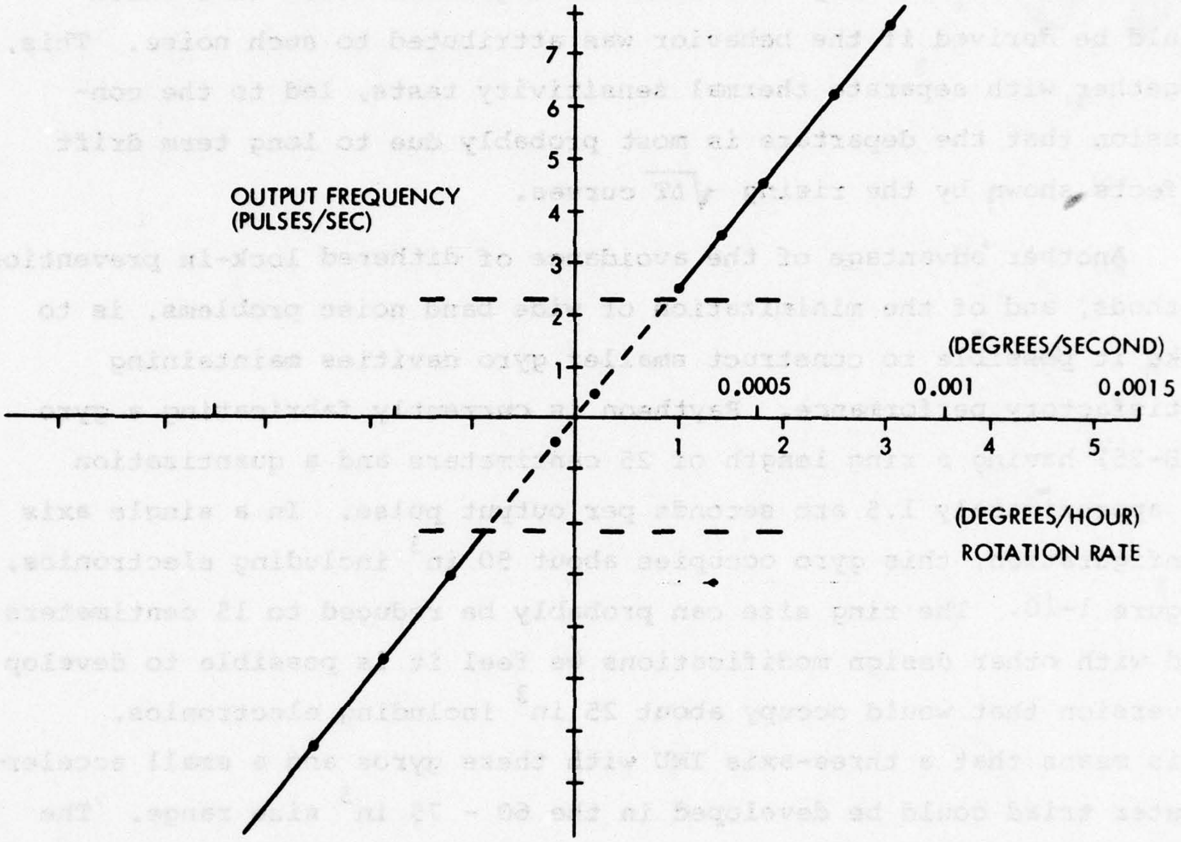

Figure 1-9 Low Rate Scale Factor Data
Multioscillator Laser Cavity

frequency fluctuations arising from residual effects preventing complete correlation in the fluctuations of counter-directed modes, or by the fundamental line width of the optical frequencies. Analysis of these factors indicates the noise limit of the multioscillator to be nearly two orders of magnitude below that which would be derived if the behavior was attributed to such noise. This, together with separate thermal sensitivity tests, led to the conclusion that the departure is most probably due to long term drift effects shown by the rising $\sqrt{\Delta T}$ curves.

Another advantage of the avoidance of dithered lock-in prevention methods, and of the minimization of wide band noise problems, is to make it possible to construct smaller gyro cavities maintaining satisfactory performance. Raytheon is currently fabricating a gyro (RB-25) having a ring length of 25 centimeters and a quantization of approximately 1.5 arc seconds per output pulse. In a single axis configuration, this gyro occupies about 50 in^3 including electronics, Figure 1-10. The ring size can probably be reduced to 15 centimeters and with other design modifications we feel it is possible to develop a version that would occupy about 25 in^3 including electronics. This means that a three-axis IMU with these gyros and a small accelerometer triad could be developed in the 60 - 75 in^3 size range. The possibility of such small units with navigation grade performance should be considered for the potential impact on future systems.

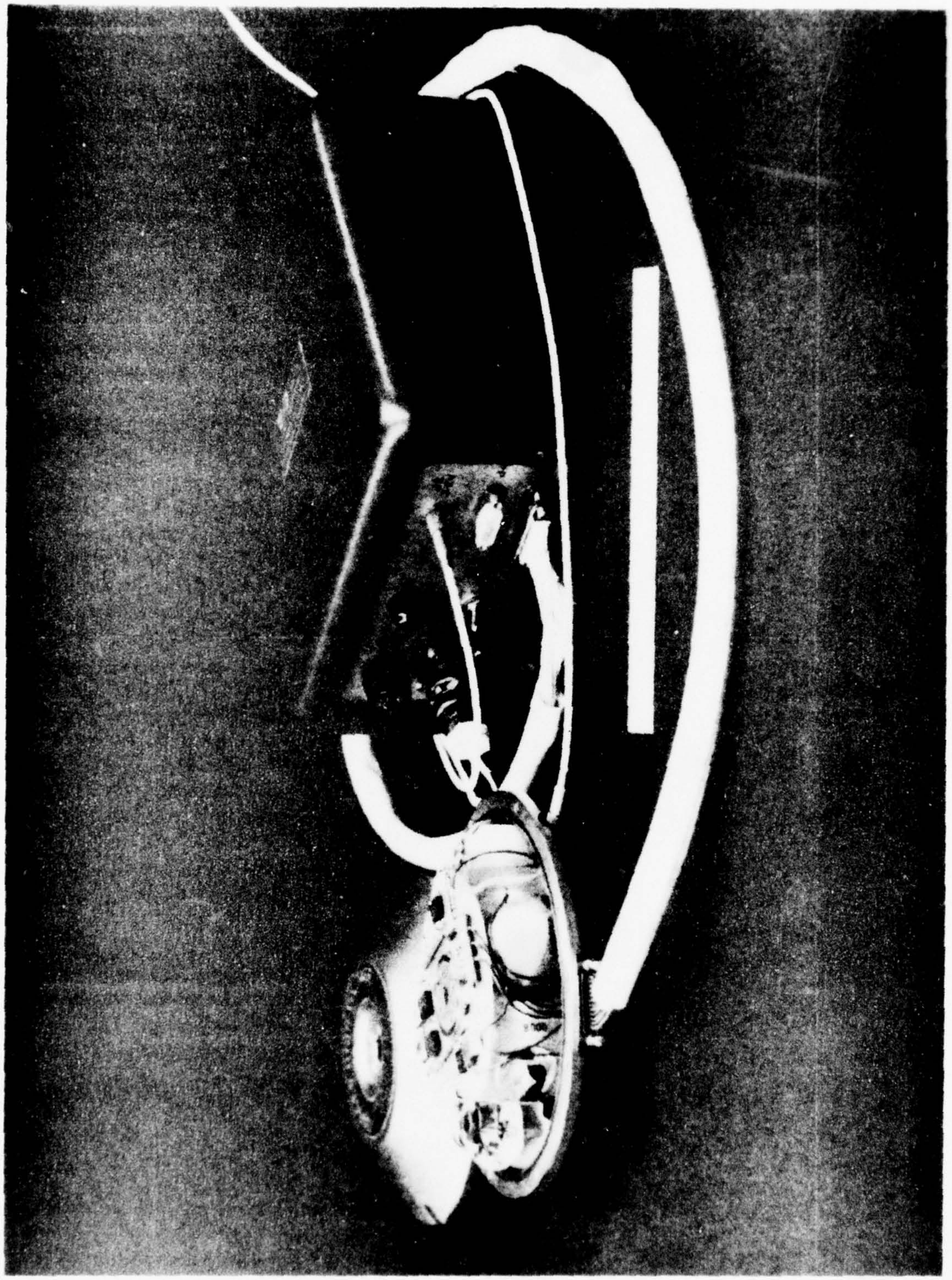

Figure 1-10 Raytheon Multioscillator Ring Laser Gyro RB-25 Shown with Power Supply and Instrumentation Interface Module

SECTION 2

MULTIOSCILLATOR LASER GYRO DESCRIPTION

2.1 INTRODUCTION

Many of the technical investigations conducted in this sponsored effort have yielded results having application in the current design of the Raytheon gyro. For this reason a description of the gyro assembly, designated RB-25, is included in this report. The -25 designation refers to the cavity pathlength of 25 centimeters. A complete gyro unit for test normally consists of two major components - the RB-25 gyro and a power supply assembly shown in Figure 2-1.

These assemblies are electrically connected by the High-Voltage Starter Cable and the Power/Signal Cable.

The total weight of these assemblies is less than 6.0 pounds including cables. Individual specifications are:

	Gyro Assembly	Power Supply Assembly
Weight	2.50 lbs., max	3.25 lbs., max
Size	5.65 dia. max x 2.26 high	5.2 x 4.9 x 2.3
Volume	40 in.^{3} max	60 in.^{3} max
Power	9 watts	7 watts

The form factor of the gyro assembly evolved from the anticipated requirement to cluster three gyros into an orthogonal triad configuration occupying a minimal volume.

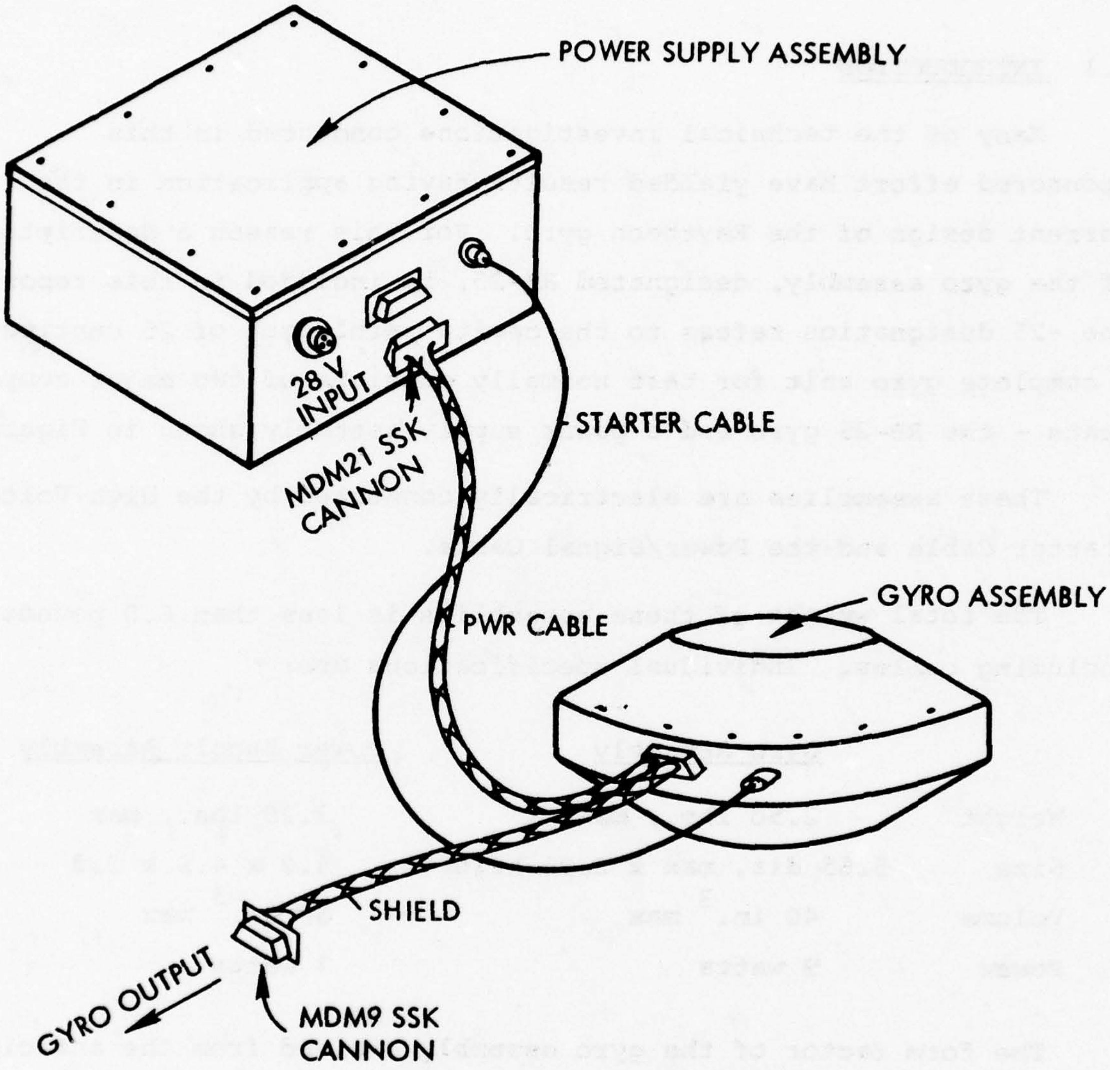

Figure 2-1 Gyro Unit

2.2 GYRO ASSEMBLY

The gyro assembly consists of three major subassemblies: the optical cavity, the electronics and the housing. (See Figure 2-2).

2.2.1 OPTICAL CAVITY

The optical cavity assembly consists of a block that supports mirrors, electrodes, mount, getter, tubulation, a Faraday rotator and an optical rotation system.

The optical cavity is fabricated from Cervit C-101, a ceramic/ vitreous material produced by Owens-Illinois. This material has a particular characteristic that provides an excellent surface for mounting mirrors. Its coefficient of thermal expansion is essentially zero from 0°C to 300°C. Four mirrors are mounted to the block by optically contacting. This not only provides a gas-tight joint, but also precisely aligns the mirrors with respect to each other.

Electrodes, consisting of two anodes and a cathode, are soldered to the block. A getter and tubulation assembly are also soldered within bores provided in the block.

The gyro mount is aligned by fixturing and then the sleeve is bonded into the center of gravity area of the Cervit block. This mount assembly and the adhesive are designed to support the block primarily in compression and mitigate shock loads into the block. The mount material Invar was selected to closely approach the coefficient of expansion of the Cervit block.

The Faraday Rotator Assembly consists of an optical rotator and a pair of magnets held in place with a retaining ring.

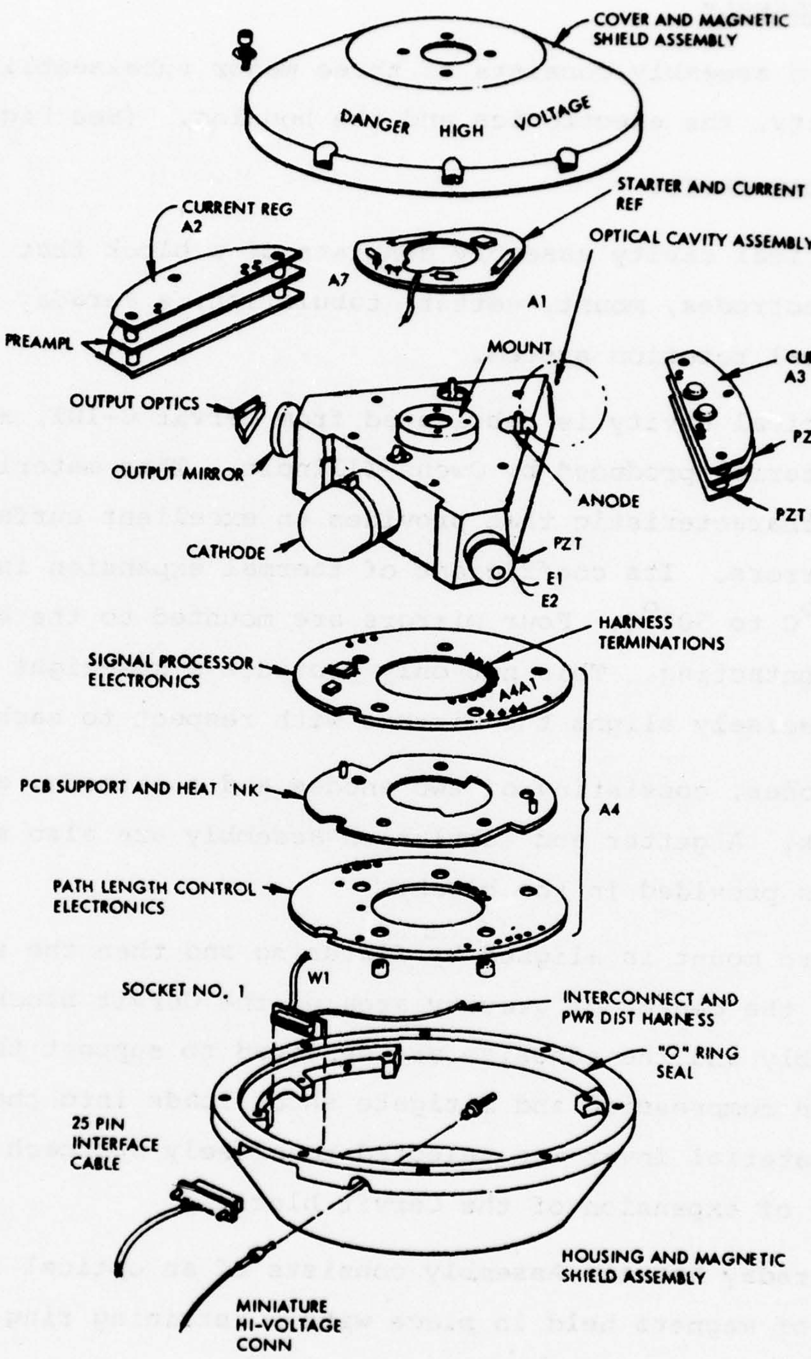

Figure 2-2 Gyro Assembly

2.2.2 OPTICS

The optical components of the RB-25 laser gyro consist of the four dielectric mirrors, a Faraday rotator, an output prism, a quarter-wave plate, polarizing material and a photodiode package.

2.2.2.1 Dielectric Mirrors

There are four types of mirrors on the RB-25 laser gyro: spherical, PZT (transducer), output and flat. All the mirror substrates are made of fused quartz. The dielectric coatings are of a standard type, employing quarterwave of SiO_2 and TiO_2. The spherical, PZT and flat mirrors have a maximum reflectivity coating which typically results in reflectivities (for unpolarized light) that are greater than 99.9% as measured with Raytheon's reflectometer. The output mirror employs a similar coating as the maximum reflectivity mirrors with fewer quarterwave layers.

2.2.2.2 PZT Pathlength Compensator

The pathlength compensator is comprised of a mirror diaphragm which is fabricated from quartz. An annular slot is machined into the quartz disc to provide sufficient compliance that the inner disc which is the actual mirror surface can move axially with respect to the outer washer (which is the mounting or reference surface). The force to provide this displacement is obtained from a stack of piezo-electric discs which are mechanically in series but wired to be electrically in parallel.

2.2.2.3 Faraday Rotator Assembly

The Faraday rotator assembly consists of a thin piece of solid material in an axial magnetic field. The rotator glass has an antireflection coating on both sides.

2.2.2.4 Output Optics

A portion of the optical energy is coupled out of the ring laser gyro and properly heterodyned to indicate the rotation rate. Optical output coupling which will give maximum power output (max signal-to-noise) is given by

$$T_{opt} = -L_i + (g_o L_i)^{\frac{1}{2}}$$

where T is the intensity transmissivity of the mirror, g_o is the single pass gain and L_i the residual cavity loss (total cavity loss minus the output mirror transmission). For the RB-25 laser gyro, T_{opt} is about one-third percent.

Differential operation of the four-frequency gyro requires processing the four cavity frequencies to give the output rate

$$\Omega \sim \frac{L}{8A}\Big((f_1 - f_2) - (f_3 - f_4)\Big) .$$

where A is the effective enclosed area and L is the pathlength (about 25 cm for the RB-25 gyro). For the RB-25 this is achieved using a specially designed output processing system.

2.2.3 GYRO ELECTRONICS

The development trend of the Raytheon Laser Gyro Program has been toward a reduction in the complexity of the gyro electronics and power requirements while improving signal output, discharge control, pathlength control, circuit performance and reliability. This has been made possible to a great extent by the development of the solid block gyro cavity. The following is a simplified description of the electronics currently in use on the RB-25.

Five categories of electronics are required by the laser gyro. These are:

1. Regulated Power
2. Signal Detection
3. Signal Processing
4. Pathlength Control
5. Starter

In addition, low voltage (for electronics) and high voltage (for the block) power are provided by the power supply assembly. Figure 2-3 summarizes the functional relationship.

a. <u>Regulated Power</u> - In particular, the laser requires current regulated power. The matched anode currents are generated from the 1KV power supply through precision current division.

b. <u>Signal Detection</u> - Signal detection is achieved by two trans-impedance amplifiers which convert the current induced in photodiodes by the impinging beams, into useful voltage levels.

c. <u>Signal Processing</u> - Signal processing is essentially the threshold determination of the AC component laser output. The processor develops a digital pulse train at the light modulation frequency in the beam.

d. <u>Pathlength Control</u> - Pathlength control is achieved by appropriate comparison of the two beams generating an error signal which in turn is translated up to useful PZT drive levels.

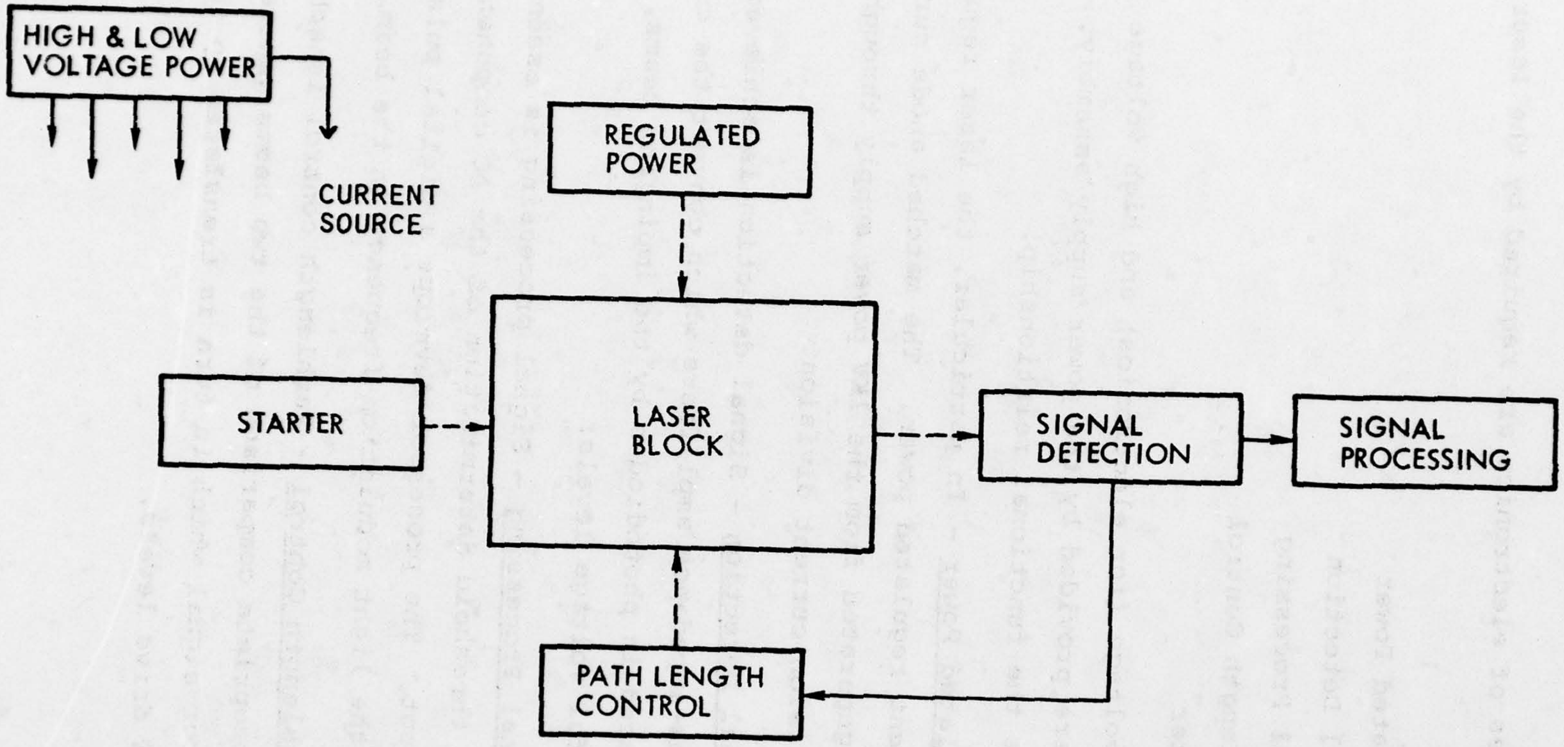

Figure 2-3 Laser-Electronics Block Diagram

e. Start and Power - Basically, a free running oscillator is used to pulse a 5KV power supply which continues to apply high voltage pulses to the laser until start has been determined.

2.2.4 ELECTRONIC PACKAGING

The gyro electronics have been partitioned in nine printed circuit board assemblies.

Two-sided circuit boards are interconnected with plated-through holes that are on a 0.025 in. grid. Artwork was generated on a plotter and a tape was generated for automatic hole drilling. All boards are solder-plated and reflowed. Components selected for these assemblies are mil-spec or equivalent. The assemblies contain a mixture of discrete components, chip capacitors, chip resistors, flat packs, TO-5 and TO-18 cans and packaged resistor networks.

The printed circuit assemblies are bolted together through metal spacers to the bottom housing which provides a thermal path to the gyro mount.

2.2.5 HOUSING

The gyro housing is a machined aluminum structure consisting of two saucer-shaped parts, one carrying the block and electronics while the other serves as a cover. (See Figure 2-2). Both cover and bottom housing fasten together at their periphery and at their center to the gyro mount. This forms a stiff structure and minimizes deflections on internally mounted printed circuit board assemblies. The housing clears the optical cavity assembly.

The bottom housing and top cover are fitted externally with a conforming magnetic shield. This shields the gyro from earth's magnetic and other stray fields and minimizes radiated interference.

2.3 POWER SUPPLY ASSEMBLY

The gyro power supply assembly consists of MIL-SPEC power supplies mounted in a machined housing. The housing not only structurally supports these units but also provides a conductive path to transfer heat to the mounting surface. Two PCB assemblies supported on spacers and an interconnecting harness complete the assembly.

All interface connectors are mounted on one side of the enclosure.

The enclosure is not sealed, therefore special attention is addressed to the insulation of the two high voltage supplies. The terminals are potted to eliminate the voltage breakdown at high altitudes.

The power supply case is fitted with a deformable RF gasket which provides EMI shielding when the cover is fastened down.

SECTION 3

GYRO SEALING STUDIES

3.1 INTRODUCTION

The objective of the sealing studies program is to devise and implement a means of bonding the various electrical and vacuum components to the Cervit gyro block with hermetic seals that have a reasonable degree of mechanical strength.

Subsequent processing of the block normally performed after these components are attached have placed many constraints on the choice of materials and procedures compatible with this processing. In order of their importance, these requirements are:

- Hermeticity
- Minimum out-gassing
- Mechanical strength
- Low seal temperature
- Reproducibility
- Long term stability
- Repairability

Various seal types were assembled during 1977 and from the laboratory evaluations of test samples of these seals, it was determined that fusion seals offered the best combination of properties from the above list of requirements.

Once fusion seals were chosen as the best choice there still remained a large number of metalizations, joining materials (solders) and assembly techniques to be selected. Six most likely metalizations were R.F. sputtered on Cervit discs and various solder types were processed in a conductivity heated, inert soldering apparatus (I.S.A.) to investigate wetting action, hermeticity, intermetallic formation and ease of assembly. From a matrix, the combination with the best performance was a trimetal system.

Most of the effort in assembling blocks has been concentrated on this trimetal/solder system; designing, assembling and deploying the various types of soldering fixtures that must be used in the I.S.A., and developing a reproducible technique to produce acceptable seals.

Many problems arose during the program that affected one or more of the seal requirements. Some of these, covered in detail in the following sections, are: 1) pump-out configuration and attachment; 2) metalization cleanliness; 3) thermal expansion differences; 4) Cervit cracking; 5) solder cracking; 6) uneven temperature distribution; and 7) instrumentation.

3.2 GYRO BLOCK SOLDERING PROCEDURE

Figure 3-1 illustrates the electrical, mechanical and optical components associated with the gyro block itself. Of concern to the present sealing studies effort is the attachment of the two anode pins, the pump-out and the cathode.

The anode pins and pump-out are located on one surface of the block and are bonded to the block simultaneously in the I.S.A. using pure Sn. The cathode is attached using a fixture which orients the cathode vertically to assist in flowing molten solder around its base.

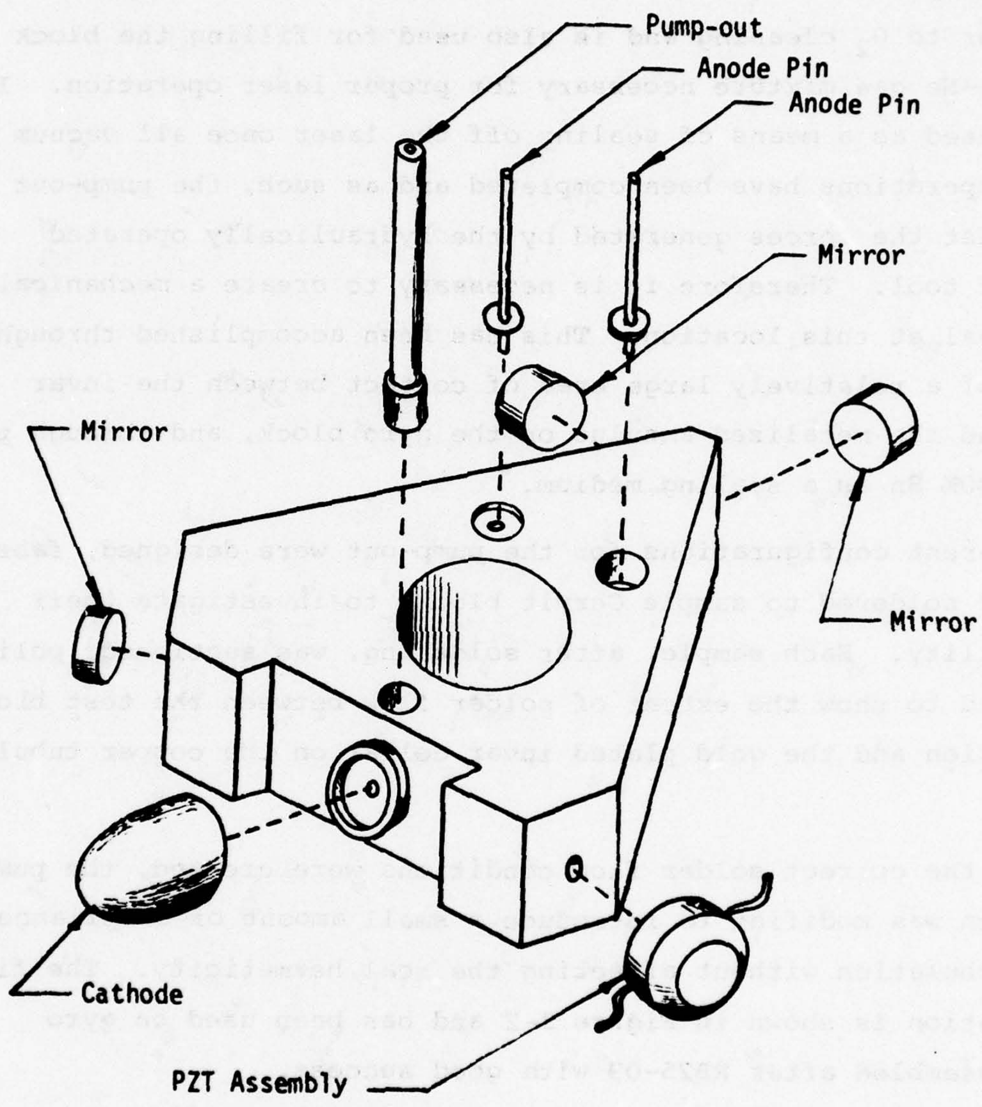

Figure 3-1 Block Components

3.2.1 PUMP-OUT ATTACHMENT

The pump-out serves as a means for evacuating the laser discharge path prior to O_2 cleaning and is also used for filling the block with a He-Ne gas mixture necessary for proper laser operation. It is also used as a means of sealing off the laser once all vacuum station operations have been completed and as such, the pump-out must resist the forces generated by the hydraulically operated pinch-off tool. Therefore it is necessary to create a mechanically strong seal at this location. This has been accomplished through the use of a relatively large area of contact between the invar collar and the metalized annulus on the gyro block, and through the use of 100% Sn as a sealing medium.

Different configurations for the pump-out were designed, fabricated and soldered to sample Cervit blocks to investigate their acceptability. Each sample, after soldering, was sectioned, polished and etched to show the extent of solder flow between the test block metalization and the gold plated invar collar on the copper tubulation.

Once the correct solder flow conditions were created, the pump-out design was modified to introduce a small amount of compliance in the tubulation without affecting the seal hermeticity. The final configuration is shown in Figure 3-2 and has been used on gyro blocks assembled after RB25-09 with good success.

3.2.2 ANODE PIN ATTACHMENT

The anode pins, also located on the upper block surface, are used only to maintain the laser discharge and do not require the degree of mechanical strength required by the pump-out. The pins are also attached to the gyro block metalization using Sn and are

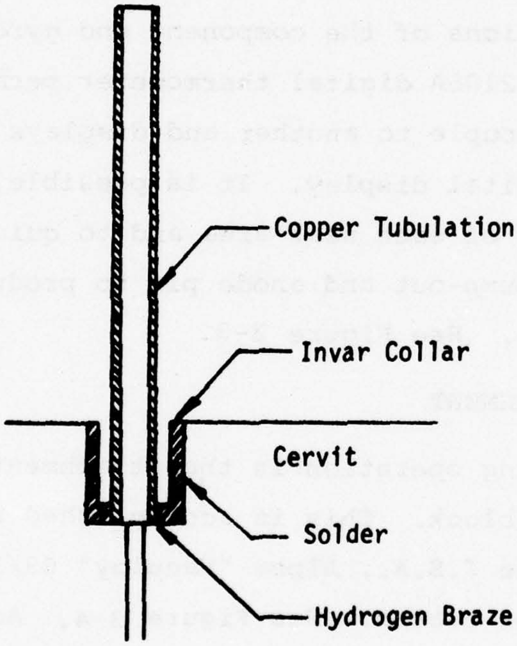

Figure 3-2 Pump-Out Configuration

normally sealed along with the pump-out in the I.S.A. at the same time. By the careful application of heat through nichrome coils located around the pump-out and the anode pin located in the shallower of the two anode pin holes, all three seal areas may be brought to the proper Sn alloying temperature of approximately 245°C.

Temperature monitoring of these seal areas is accomplished by precisely locating chromel-alumel thermocouples on the metalized surface at the junctions of the component and gyro block. A ten-station Fluke model 2106A digital thermometer permits rapid switching from one thermocouple to another and displays the location temperature on a digital display. It is possible, therefore, to know the temperature of each seal area and to quickly adjust each heater coil at the pump-out and anode pin to produce the desired alloying temperature. See Figure 3-3.

3.2.3 CATHODE ATTACHMENT

The next soldering operation is the attachment of the aluminum cathode to the gyro block. This is accomplished using a specially designed fixture, the I.S.A., Alpha "Vaculoy" 63/37 SnPb eutectic solder and a nichrome heater. See Figure 3-4. Again, temperature monitoring is critical during this operation since the melting temperature of the 63/37 solder, being 183°C is not far from that of the pure Sn (231°C)used on the previously attached pump-out and anode pins. Care must be taken to carefully heat the gyro block with the I.S.A. and the cathode using the nichrome coil to produce a fully wetted solder seal without affecting the Sn seals. This has proven to be a difficult task, but with proper attention, the seal can be reproduced successfully.

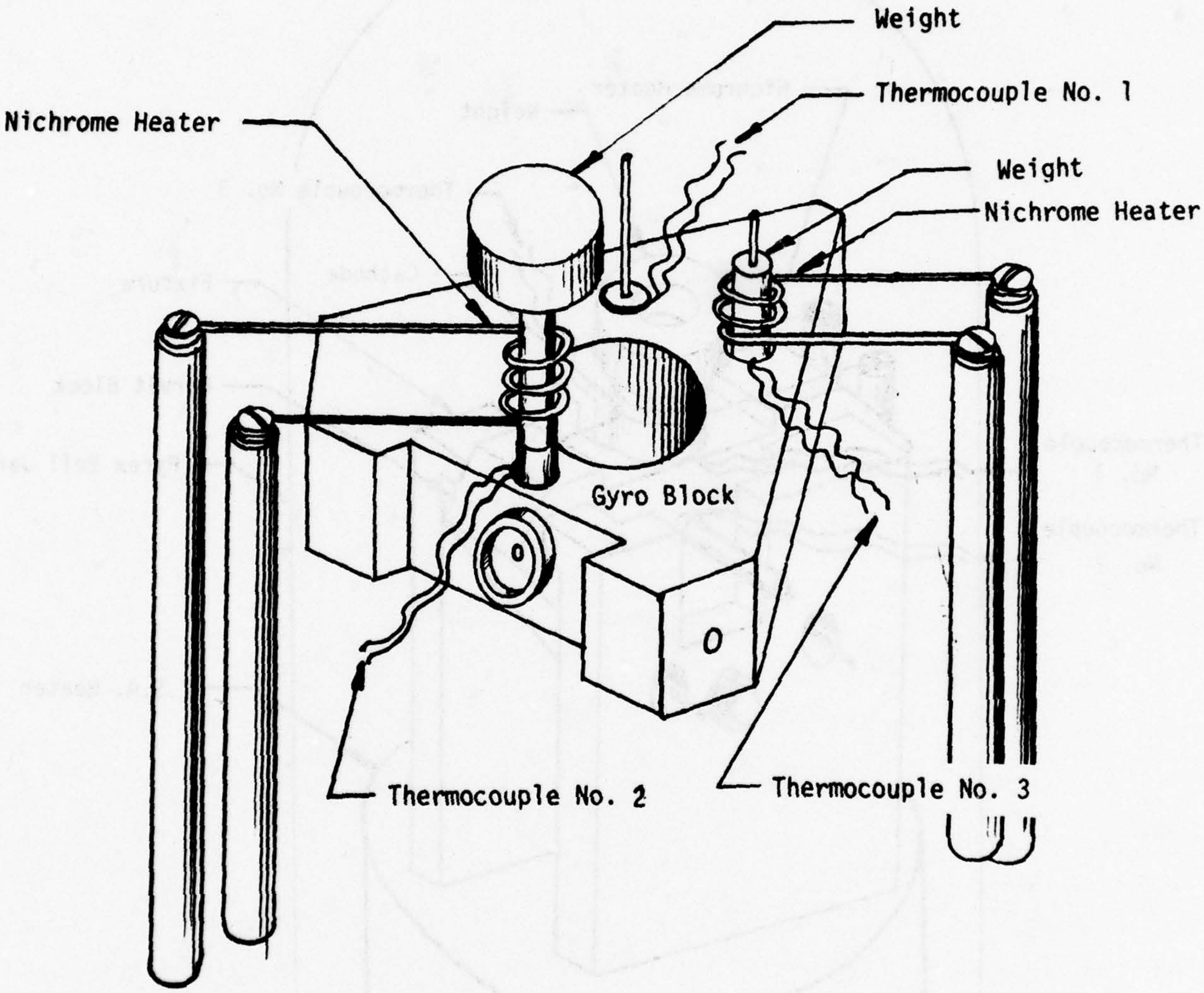

Figure 3-3 Thermocouple and Heater Locations

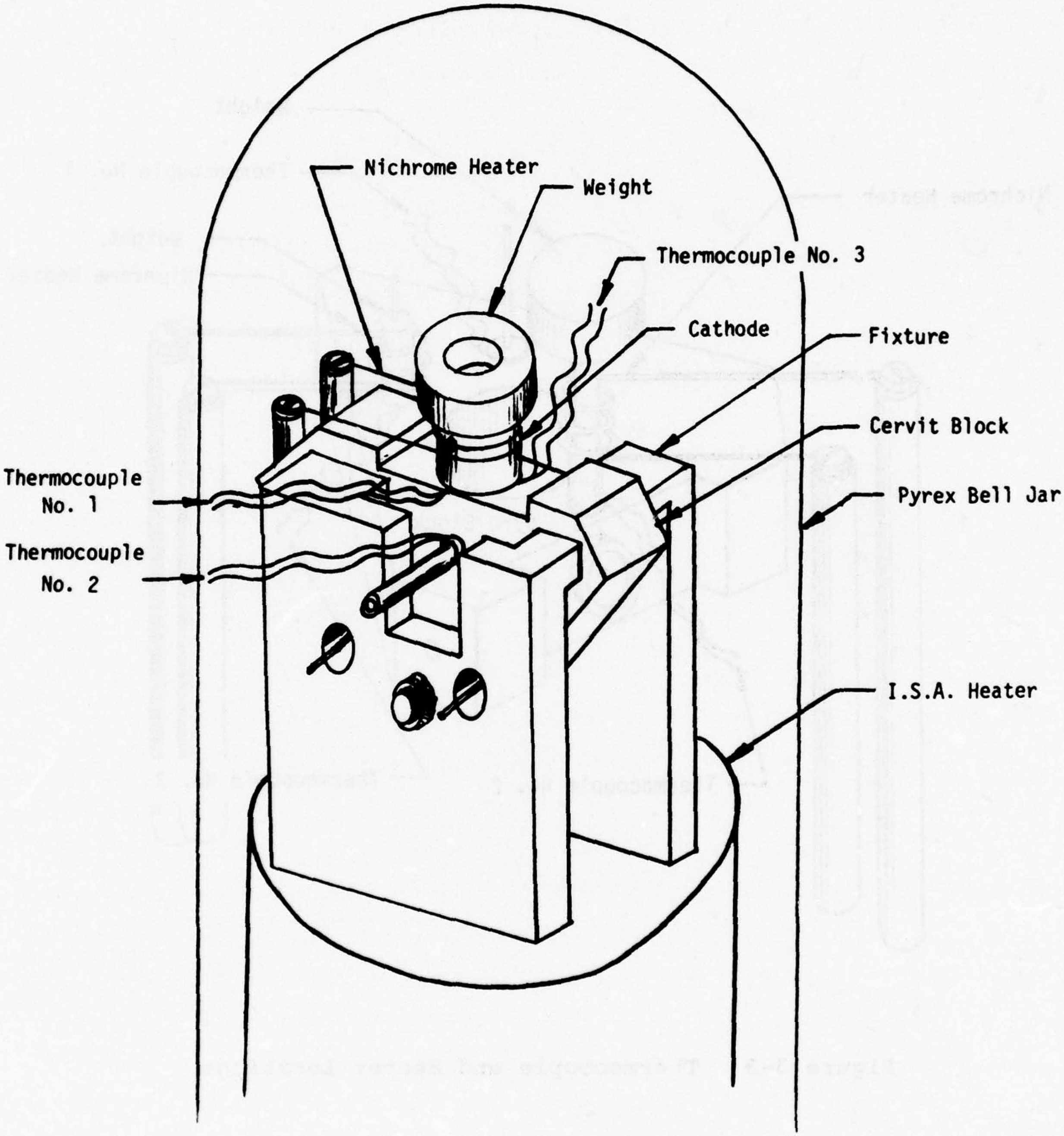

Figure 3-4 Inert Soldering Apparatus

3.2.4 METALIZATION CLEANLINESS

Because soldering is performed in an inert atmosphere (He) without solder flux in the I.S.A., absolute block and component cleanliness is essential to produce hermetic seals. The block is usually vacuum baked at 400°C prior to R.F. sputtering and great care is exercised during this and the soldering operation to prevent contamination. Sealed poly-bags are used whenever the block or its components leave the class 100 clean room area. Whenever the block is in process, it is in a class 100 environment and is handled only on non-critical areas with finger cots and surgical gloves.

These procedures, carefully followed, have produced excellent solder seals using 60/40 solder, 63/37 solder and Sn. Inattention to these procedures can result in de-wetting or lack of solder flow as shown in Figure 3-5 and usually produces leaky seals.

3.2.5 THERMAL EXPANSION PROBLEM

When the aluminum cathode is heated in the I.S.A. during the sealing process, the cathode expands. This expansion causes a problem during the cool-down cycle due to the large differences in the thermal expansion coefficients of aluminum and Cervit. The heated solder at the seal solidifies at 183°C and attempts to restrain the aluminum cathode as it shrinks during its cool-down cycle. As the aluminum continues to shrink, tensile stresses in the solder and Cervit increase until either or both the solder and Cervit fail, producing a gross leak in the seal (i.e., a leak rate greater than 1×10^{-5} cc's He/sec).

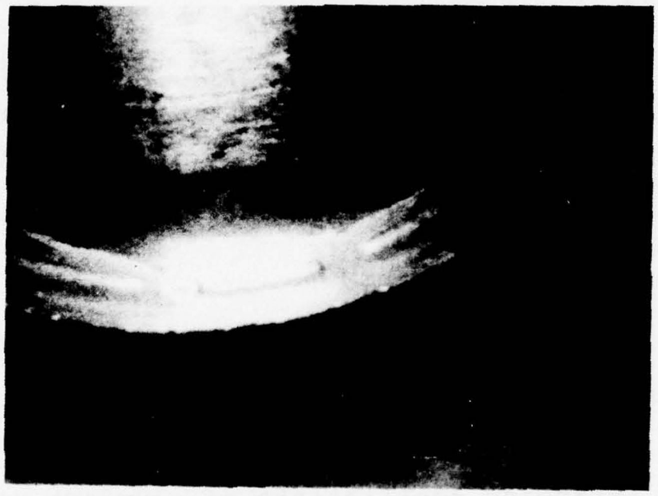

Figure 3-5 Cathode Seal De-Wetting

Analysis of the thermal stresses produced by the shrinkage of the aluminum and the consequent tensile failure of the solder and/or Cervit have shown that this failure could be avoided by machining away the edge of the cathode to 10 or 15 mils at its base and by drastically reducing the solder content of the seal. This reduction of the solder seal content was accomplished by reducing the diameter and thickness of the preform used for sealing.

Both of these modifications were made on test cathodes and preforms and a number of acceptable, crack-free solder assemblies have been made in the I.S.A. In addition, gyro block RB25-10 has been assembled using this approach with good results.

3.3 TEST VEHICLE ASSEMBLY

To investigate the electrical parameters of the laser discharge, a test vehicle was devised which simulates the discharge characteristics of interest. The components required for one assembly are shown in Figure 3-6.

Because of the satisfactory results obtained when soldering Cr/Ni/Au metalizations on the Cervit gyro block and its components, it was decided to use the same tri-metal system on the pyrex tubulation, Cervit disc and aluminum cathode.

Cr/Ni/Au used in combination with 60/40 SnPb, 63/37 SnPb eutectic and 100% Sn produced good seals at the interface between two metalized surfaces, but, because of the choice of the other materials used in the assembly, many of the solder seals assembled were not leak tight.

The basic problem encountered in soldering the test vehicle was the large difference in the thermal expansion of the pyrex tubulation and the Cervit (32×10^{-7}) in/in°C vs. zero). As the solder cooled during the processing cycle, the solder solidified

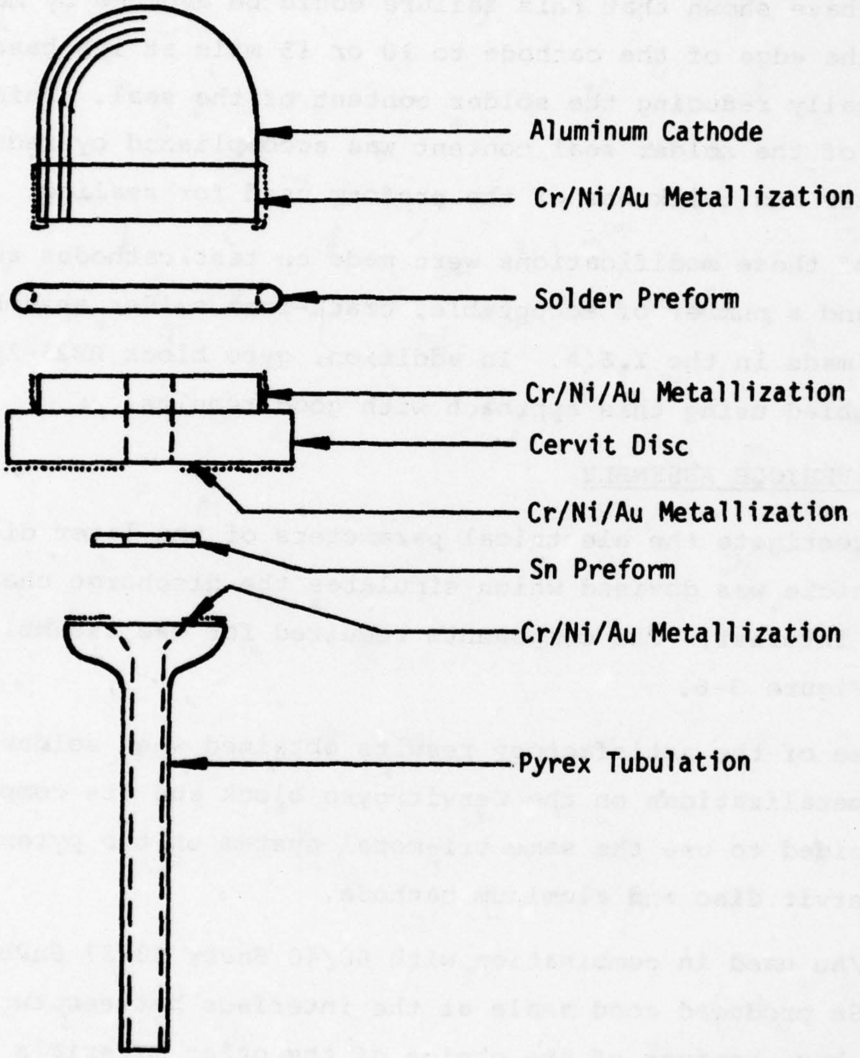

Figure 3-6 Test Vehicle Assembly

at 231°C, firmly trapping the pyrex in its expanded state. Upon further cooling, the pyrex continued to shrink and the tensile stresses increased until a maximum of approximately 10,000 psi was reached and at that point, the pyrex, being inelastic and relatively weak in tension, failed, producing a leaky seal. This situation is not unlike the problem experienced when the aluminum cathode shrinks on the gyro block and either cracks the solder or the Cervit.

An extensive redesign was undertaken so these seal failures could be avoided but at the same time, produce a vehicle capable of producing useful data.

3.4 CONCLUSIONS AND RECOMMENDATIONS

As mentioned earlier in this section, fusion seals were chosen because they offer the best compromise of mechanical and other properties necessary to effectively seal the gyro block. The combination of Cr/Ni/Au metalizations and either 63/37 "Vaculoy" eutectic or pure Sn was chosen to be a workable system for producing fusion seals assembled in an inert gas, conductively heated soldering apparatus. An important consideration when the decision was made to employ fusion seals and the materials selected in the preceding paragraph was that this system should be compatible with a future sealing program, Phase II soldering.

Phase II soldering relies on a far less labor-intensive scheme for the component attachment than the bonding technique used with inert gas soldering.

This procedure requires a specially designed soldering fixture (see Figure 3-7) and an inert gas, convectively heated, partial

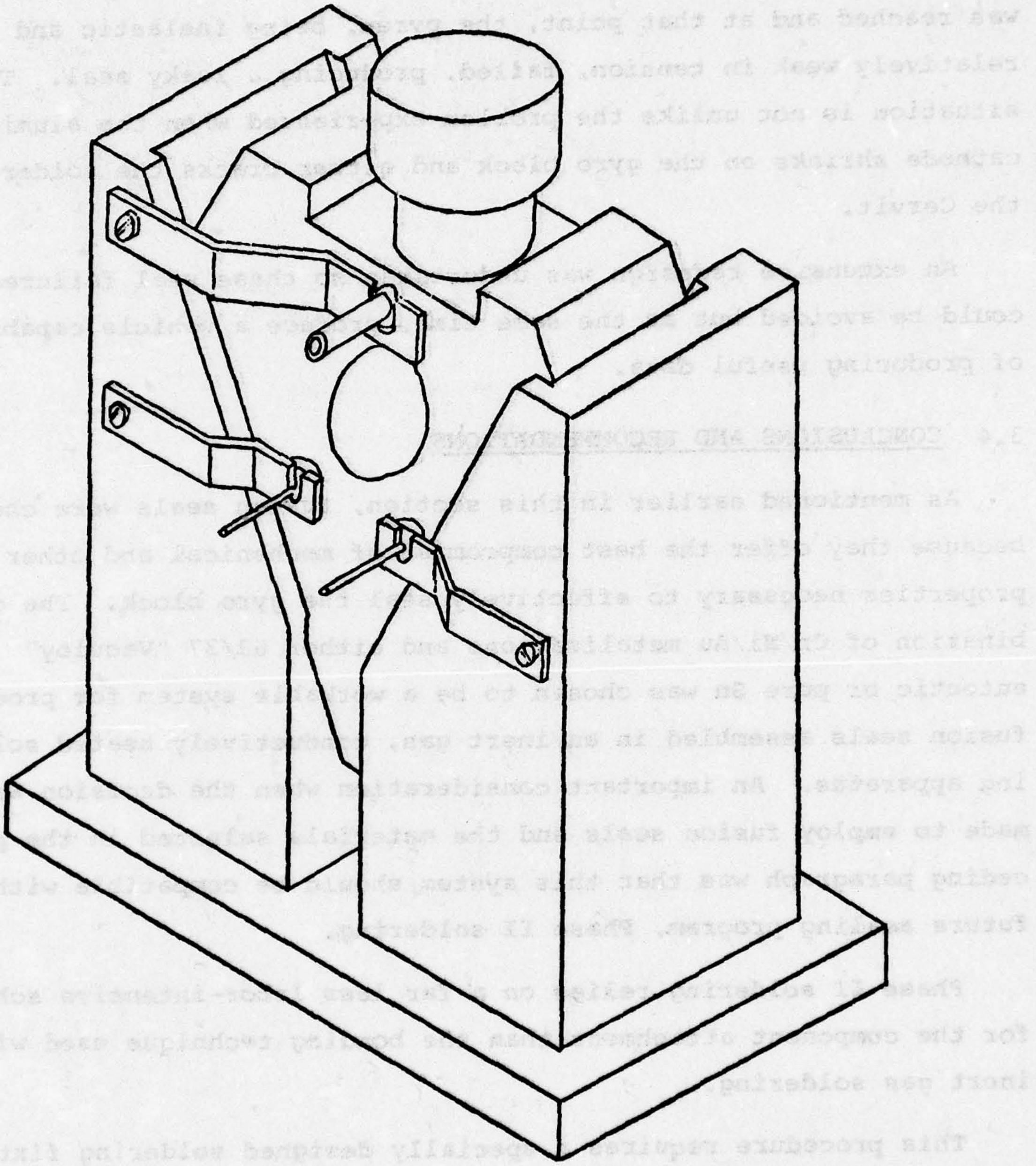

Figure 3-7 Phase II Soldering Fixture

vacuum oven. Solder preforms, of appropriate size, are loaded onto the gyro block. Then the anode pins, cathode and pump-out are placed over them, under spring tension. The fixture, gyro block components and preforms as a unit are then placed in the oven, thermocouples attached and then heated by inert gas and thermal radiation from the oven walls to the precise alloying temperature needed to form an effective seal. It is important to note that since the maximum alloying temperature may be set by oven controls to within $\pm 1^{\circ}F$, careful inspection of the process is not required. An operator merely loads the oven and returns when the joining process is completed.

Phase II soldering also lends itself to the tasks mentioned earlier in this section -- test vehicle assembly and magnet soldering, while at the same time allowing a wide choice of soldering materials and metalizations to be employed without changing the basic procedure outlined above.

It should be emphasized that all the joining tasks detailed in this section, used with the I.S.A., are compatible with the procedures to be used in the Phase II soldering program and because of the technical improvements and the labor-saving aspects of the program, it is a logical choice for expansion of the expertise required for effective gyro block sealing.

SECTION 4

GAIN MEDIUM INVESTIGATION

4.1 CATHODE DEVELOPMENT

This report summarizes the work carried out in 1976 by the Microwave Tube Operation (MTO) on the forming of aluminum laser gyro cathodes. The work was done for the laser optics group of Sudbury.

This task was initiated to study hobbing as a means of fabricating a laser cathode having a mirror-like interior surface and free of contaminants. Previously, cathodes had been fabricated using a lathe and the resulting surface was irregular; it was felt that retention of residual foreign matter which could affect laser operation was likely.

A hob was designed by the tool engineering department of MTO and fabricated. The shape of the hob duplicated the interior of the cathode. The hob was fabricated from high speed tool steel. A blank of the 2024 aluminum alloy was contained in a thick-walled steel "bull" ring and hobbed with the tool. It was found that the material would not extrude at full pressure which was 100 tons. Another similarly shaped aluminum blank was annealed at 800°F for 2-1/2 hours and slow cooled for eight hours to effect a complete annealing. Brinell hardness was measured as being 43. A hobbing run was made with material using a 400 ton Verson press. Extrusion occurred but a side wall tear was evidenced at a depth of about 0.5 inches. In an attempt to correct this problem another aluminum blank annealed in the same manner was bored to a depth of 0.5 inches with a 0.990 diameter drill. Hobbing was carried out again in the Verson press but tearing and roughness of the inside surface was noted. At this point it was felt that 2024 aluminum could not be hobbed to the desired shape. However, a final experiment was carried out whereby the aluminum blank was machined with a formed tool to within 10 mils of its desired final shape, then, finished with the hob. The resulting surface was of a quality poorer than that of the initial machine surfaces due to roughness.

The conclusion of the Tool Design Engineering Department was that aluminum type 2024 does not have the characteristics which make it acceptable for the hobbing process. Its main drawback is the resistance to extrusion. This is due in part to its poor ductility. Type 6061 aluminum could have been easily fabricated in the desired shape using the hobbing tool.

<u>Conclusion</u> Type 2024 aluminum alloy can not be hobbed by conventional techniques.

<u>Recommendation</u> No further work should be carried out in an attempt to hob this material. Work should be carried out on the machining process to produce a smooth surface. Also, a cleaning process should be devised for the treatment of the machined aluminum surface to assure complete removal of the contaminants which would inhibit uniform thin layer oxidation on the inside of the cathode.

4.2 GAIN MEDIUM CHARACTERIZATION

4.2.1 INTRODUCTION

Parametric studies involving the laser gain medium were conducted to define the performance of the gain medium as it affects the Multi-oscillator Ring Laser Gyro. In order to define the gain medium as an electronic device, i.e., a system design element, the relationship between its electrical characteristics and discharge geometry, gas fill parameters, and laser gain needed to be established. The work described in this section was conducted in an effort to realize this goal. The discharge geometries and gas fill parameters investigated were consistent with current Raytheon gyro cavity designs and wherever possible data was taken utilizing actual gyro cavities.

Significant effort was expended in studying the AC small signal behavior of the plasma to develop an understanding of the dynamics of the discharge with respect to operating stability. Treating the discharge as a single-port, two-terminal active device, its frequency response was analyzed and a small signal equivalent circuit developed. Frequency data was taken on the cathode region as well as on the cathode region plus positive column in order to provide insight into model partitioning. Stability of the resulting topology was analyzed and related to laboratory investigations of plasma stability.

4.2.2 TEST VEHICLES

Two multi-anode, dual cathode test models were fabricated to provide part of the data base for the gain medium investigations. These units were designed as linear tubes with AR-coated windows mounted near normal to the tube bore. The loss characteristics of the windows used were accurately determined so that laser performance of the gain medium could be characterized. Cleaning and assembly procedures used during the fabrication process were the same as those used in the fabrication of the solid block laser cavities. The bore is 0.075" diameter machined out of Cervit. Anodes (Tungsten) were placed at the ends, at the center, and midway between each end and the center. Two pyrex cathode bulbs are attached to the block at the center; one bulb housing a 5-mA cold aluminum cathode, the other a 10-mA cold aluminum cathode. Additional anode pins are provided in the neck of each bulb to provide additional test points near the cathode region. Epoxy was used to seal the anodes, windows, and cathode bulbs to the Cervit block. A separate pump port is provided at the center of the block to enable connection to the fill stand through a vacuum valve. A photograph of these units is shown in Figure 4-1.

An additional test fixture was designed and fabricated to enable the evaluation of other cathode and bore geometries on the discharge electrical characteristics. This fixture allows for the insertion of different cathodes via a flange assembly into a glass cathode bulb. Attached to the neck of this bulb are five glass capillaries in a spoke arrangement each of a different inside diameter (0.040", 0.050", 0.060", 0.080", 0.100") and each with an anode pin at the capillary end and at the midpoint. An additional anode is placed in the cathode bulb neck. Three of these capillary "Jacks" were fabricated and assembled. These units were not available in time for experimentation, however, due to delays encountered in fabrication and cleaning. The glass to metal seals had to be reworked when the originals fractured during final assembly. The closed capillary design made it impossible to get the cleaning solution to the outer anode pins. This problem was corrected by adding to the capillary ends temporary exit tubes for the cleaning

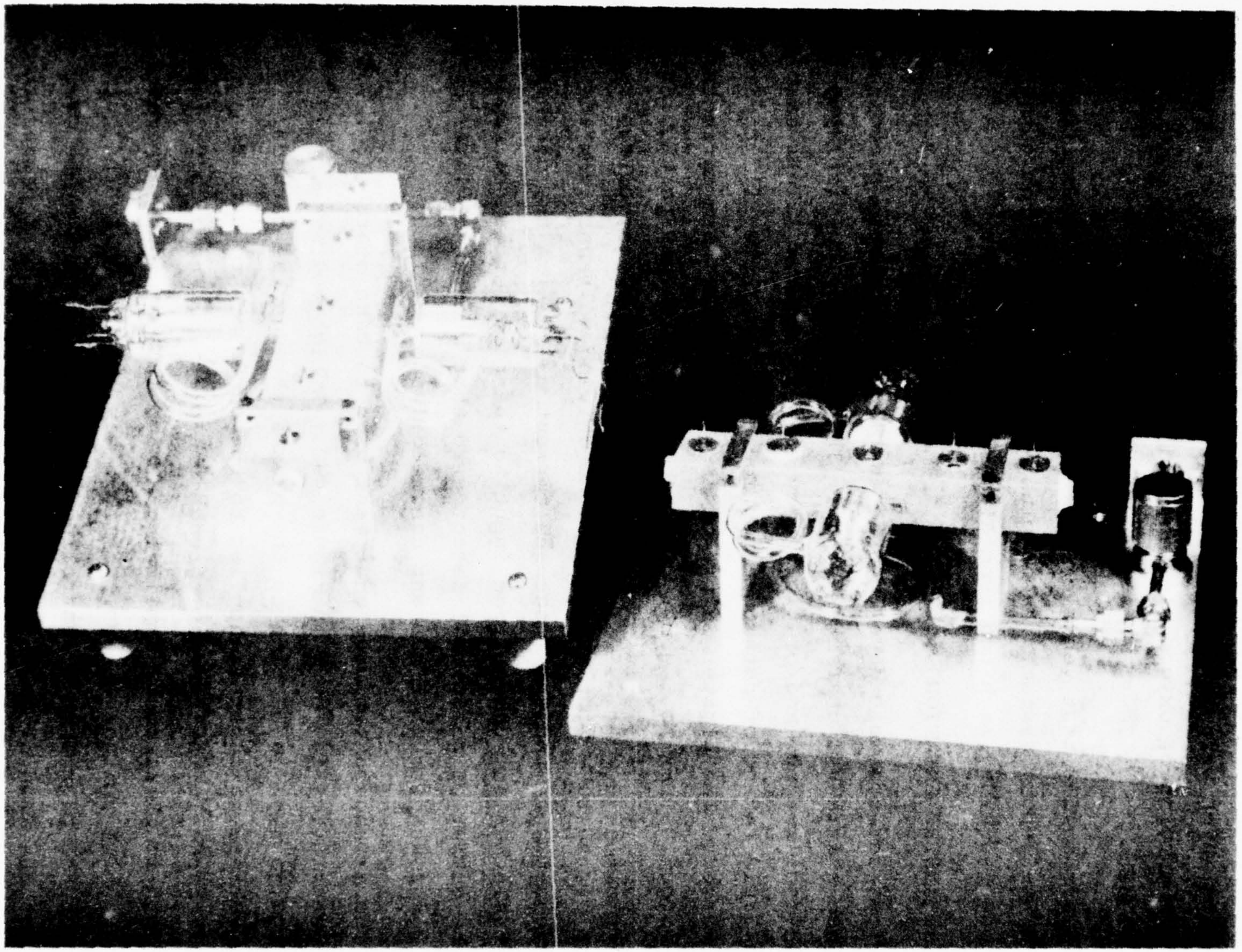

Figure 4-1 Laser Tube Test Vehicles

solution which were later pinched off. These units were processed up to the point of oxygen cleaning and could be used at some future date.

Seals on the test vehicles were made with Bacon Industries' LCA-9/BA-5 epoxy system. Anode pins were fabricated from tungsten. Cathodes were dry-machined from Alcoa 2024 raw stock.

4.2.3 INSTRUMENTATION

Test set-ups were developed to enable the automatic plotting of tube static V-I characteristics. The curve can be displayed on an oscilloscope and/or plotted by an X-Y recorder. This enables more rapid taking of data on a particular tube as the fill parameters are varied. The plotter is useful in the range of tube currents from about 0.5 mA to 5.0 mA. The range for which any particular geometry-fill combination can be run depends upon the voltage requirements of the tube with respect to the driving voltages from the test equipment, and the range and current over which the discharge is stable. Also, the voltage input to the recorder can be replaced by the output of an optical detector so that a curve of laser optical power versus discharge current can readily be obtained.

The arrangement of the equipment used to take static (DC) V-I characteristics is shown in Figure 4-2. A high voltage supply is used to apply a DC bias to the plasma through the cathode. A high voltage sawtooth is applied to the anode pin to provide a small change in the current through the plasma. The high voltage sawtooth is obtained by amplifying a ramp from a signal generator using a high voltage op-amp. In this way, one can vary the current through the plasma in a controlled manner. A current probe over the cathode lead is used to determine the current that passes through the plasma. Coil L_1 provides a current gain of 200. Capacitor C_1

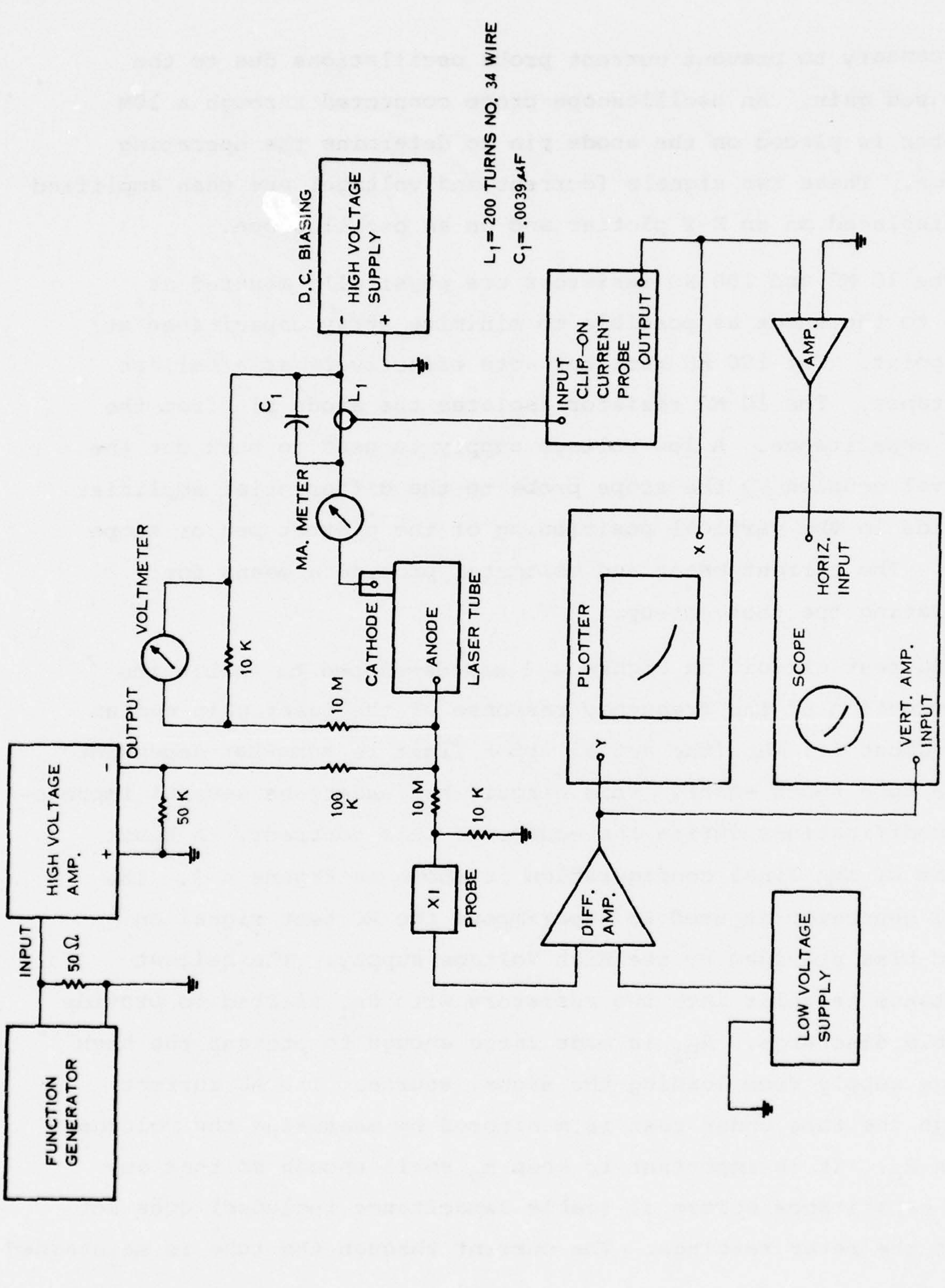

Figure 4-2 Test Set-Up for Measurement of Discharge V-I Characteristics

is necessary to prevent current probe oscillations due to the increased gain. An oscilloscope probe connected through a 10M resistor is placed on the anode pin to determine the operating voltage. These two signals (current and voltage) are then amplified and displaced on an X-Y plotter and on an oscilloscope.

The 10 MΩ and 100 KΩ resistors are physically mounted as close to the anode as possible to minimize stray capacitance at this point. The 100 KΩ resistor acts effectively as a ballast resistance. The 10 MΩ resistor isolates the anode pin from the probe capacitance. A low voltage supply is used to buck out the DC level coupled by the scope probe to the differential amplifier and aids in the vertical positioning of the plotter pen or scope trace. The current meter and voltmeter provide a means for calibrating the test set-up.

The test circuit in Figure 4-3 was developed to enable the determination of the frequency response of the laser gain medium up to about 1.5 MHz (the actual upper limit is somewhat dependent on the tube under test). This circuit has undergone several improvement modifications during the course of this contract. A block diagram of the final configuration is shown in Figure 4-3. The signal generator is used to superimpose the AC test signal on the DC bias provided by the High Voltage supply. The ballast resistance is split into two resistors with R_{B_1} slected to provide a stable discharge. R_{B_2} is made large enough to prevent the high voltage supply from loading the signal source. The AC current through the tube under test is monitored by measuring the voltage across R_S. It is important to keep R_S small enough so that any stray capacitance across it (cable capacitance included) does not affect the meter readings. The current through the tube is maintained

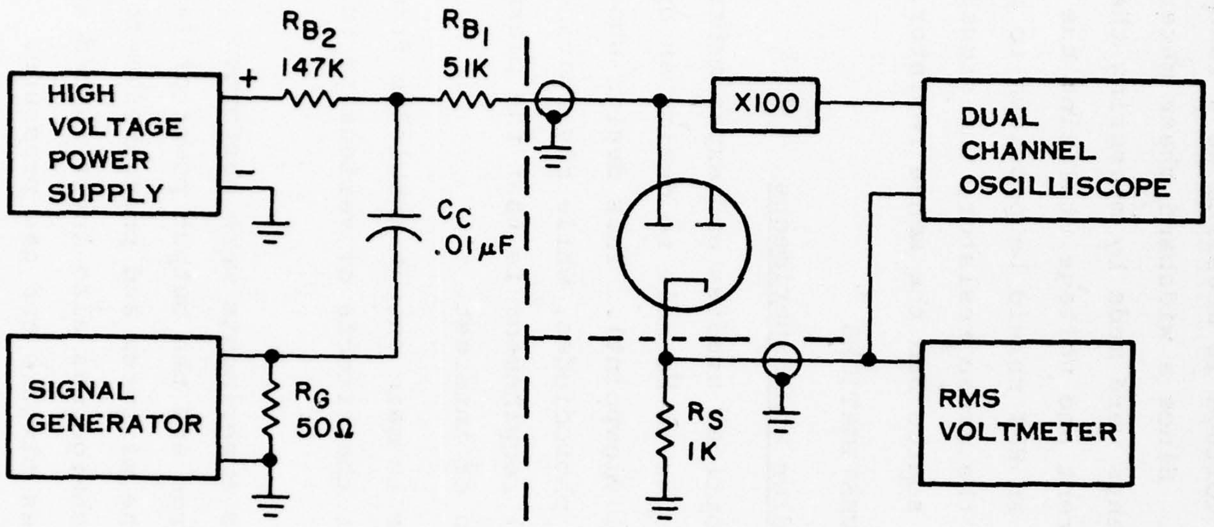

Figure 4-3 AC Test Circuit

constant by adjusting the output of the signal generator at each frequency. The tube voltage is measured as a function of frequency with an oscilloscope. Since a wideband phase meter was not available, phase measurements were made by measuring the time difference between the tube current and voltage utilizing the oscilloscope. It is important that an RFI shield be provided to prevent coupling between the tube and the sense resistor, the signal source and the tube, and the signal source and the sense resistor.

4.2.4 LABORATORY INVESTIGATIONS

4.2.4.1 Optical Studies and Experiments

The goal of our optical studies and experiments was to gain enough information so as to be able to design an optimum laser gyro (from an optical viewpoint). This design should have enough output power for the photodiodes, while dissipating a minimum of power. An additional requirement is that the plasma should be stable for the region of interest.

A second goal was to gain enough knowledge from the data so as to be able to predict the effects of various perturbances on the system.

For these reasons experiments were performed that investigated the gain of a discharge and the output power of laser gyros and linear tubes where the mixtures and pressures were varied. The stability of the discharge was also investigated as a function of ballast resistors, gas mixture and gas pressure.

A very important parameter for laser gyro performance is the amount of output power available from the gyro. This output power is a function of the gain available from the discharge. The amount of gain is determined by the size of the bore (diameter and length), by the mixture and pressure of the gasses present, and by the current exciting the discharge. To optimize the gain medium for laser gyro performance it is important to know how the available gain varies as a function of the various parameters. One way of determining the gain is to measure the threshold of lasing action. Unfortunately, in many cases that were tried, the laser tubes lased at the lowest currents at which a stable discharge could be maintained.

An experiment was set up to measure the actual gain of a laser tube. Using our reflectometer we measured the gain of a tube at one frequency to an accuracy of ±0.01%. Since it is desirable to measure the gain at various points under the gain curve we are considering building a new "probe laser". This laser will have one of its mirrors attached to a piezoelectric material. The laser will be filled with the same gas as the tube under test. Thus, one will be able to measure the actual gain at every point on the gain curve.

We have done several experiments that measured power output, from a laser gyro, as a function of Ne^{20} vs. Ne^{22} ratio, as a function of He^{3} or He^{4} gas, and as a function of total gas pressure.

To measure power output as a function of gas pressure, an RB-55 laser gyro bore diameter 0.075" was filled with a 10:0.5:0.5 ratio of He^{3} to Ne^{20} to Ne^{22}. Power output was measured in each case at a total discharge current of 2.5 ma, 3.5 ma, and 4.5 ma.* A graph of this can be seen in Figure 4-4. This indicates that the optimum pressure for this bore diameter and gas ratio is between 3.5 and

---

*The pathlength of the gyro was monitored and kept constant throughout the experiments.

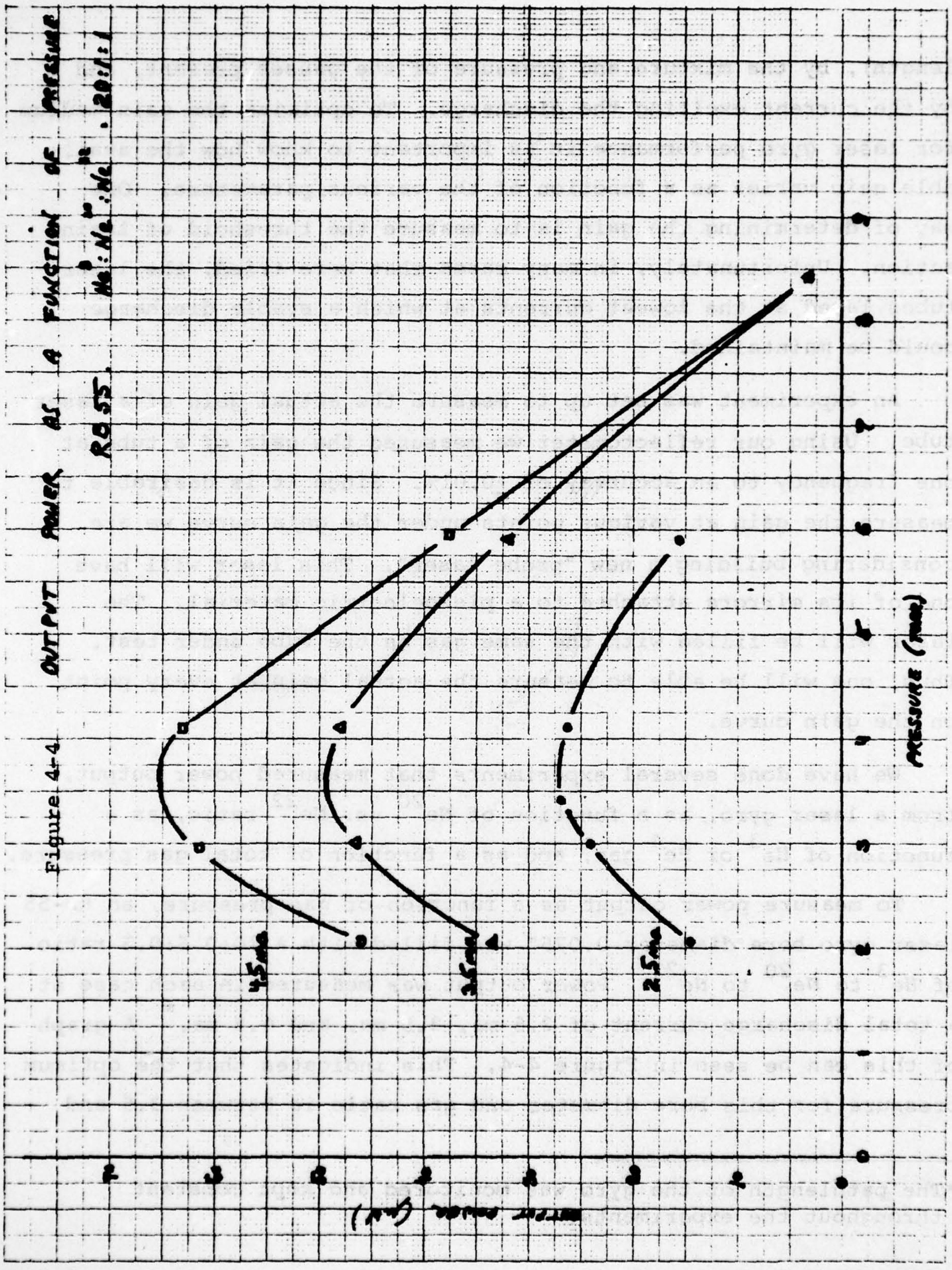

Figure 4-4 OUTPUT POWER AS A FUNCTION OF PRESSURE

4 Torr. To determine the effect of Ne^{20} to Ne^{22} ratio on power output experiments were performed on a RB-25 laser gyro where the Ne^{20} to Ne^{22} ratio was varied between 0.45 to 0.55 and 0.55 to 0.45. The gyro was filled with an 8 to 1 ratio of He^{4} to Ne^{20} and Ne^{22}. The total pressure of the gas mixture was kept at 3.1 Torr. The optical output in one direction was monitored to keep the optical pathlength constant while the output in the other direction was monitored to measure the optical power output. The mirror used for the output signals was a maximum reflecting mirror since no attempt was made to maximize the power output of the gyro. Thus the measurements are meaningful only in a relative way as the optical output power is proportional to the transmission of the output mirror. The output power of these mixes as a function of cathode current is plotted in Figure 4-5. Part A contains a plot of the output power with the discharge in one leg of the gyro. Part B is a plot of the power output for both legs of the discharge operating. As can be seen from these plots the power output is essentially the same for Ne^{20} to Ne^{22} ratios between 0.45 to 0.55 and 0.55 to 0.45. (These are the ratios of interest for laser gyro operation.) We can also see that the maximum output can be obtained with a current of about 4.5 ma through a 1.25 ma bore.

To determine the effect of He^{3} vs. He^{4} on the output power of the gyro, we filled an RB-25 gyro with an 8 to 1 ratio of He^{4} or He^{3} to 0.5 Ne^{20} and 0.5 Ne^{22}. The total pressure of the gas mixture was kept as before, at 3.1 Torr. Figure 4-6 shows the power output as a function of current for a He^{3} and He^{4} gas mix. The data indicates that when operating the gyro (both legs of the discharge on) between 3 ma and 6 ma there is a 10% to 15% gain in power output if one uses the He^{3} instead of the more common He^{4}. With only one

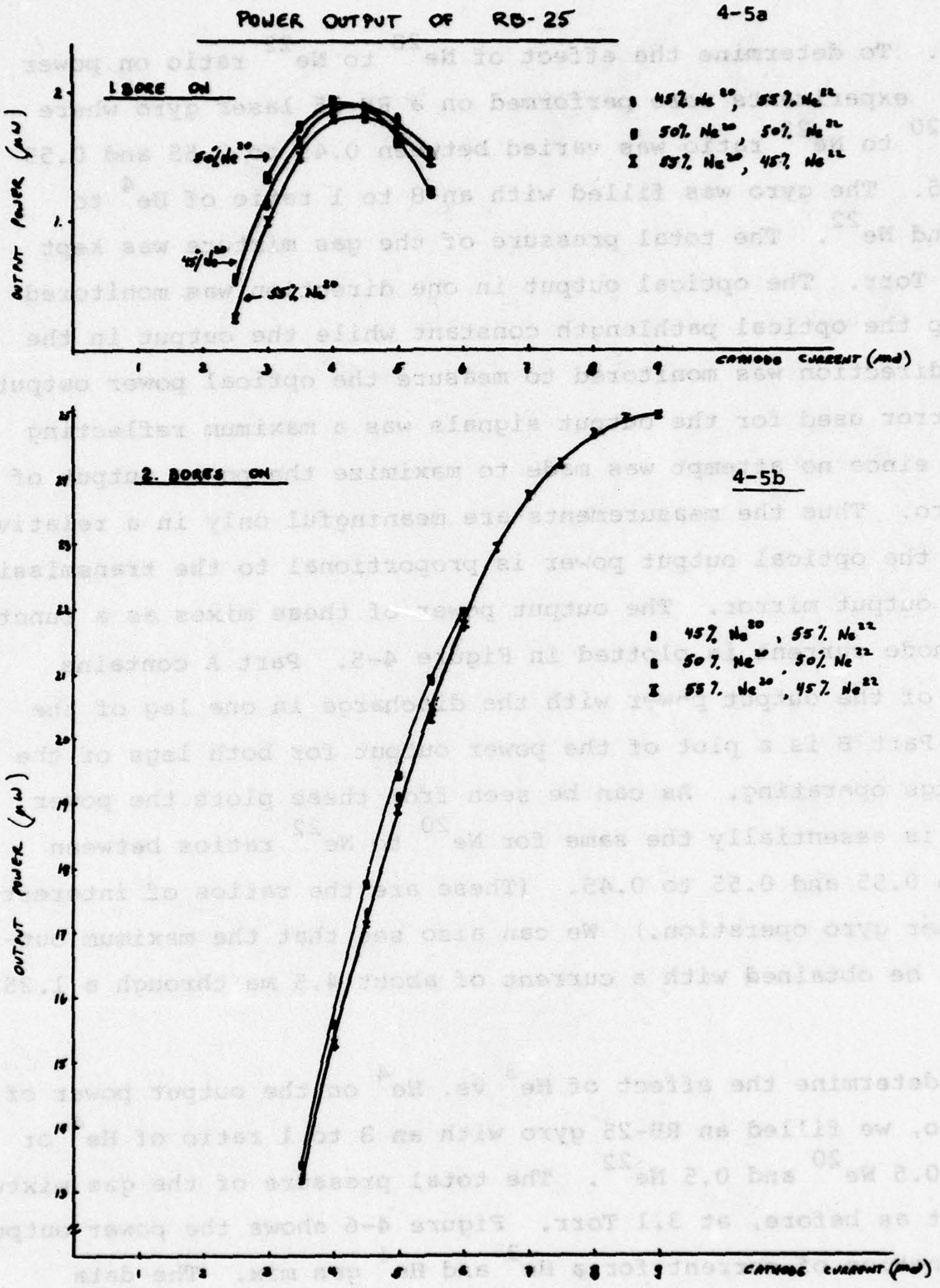

Figure 4-5 Power Output vs. Cathode Current for Several Neon Isotope Ratios

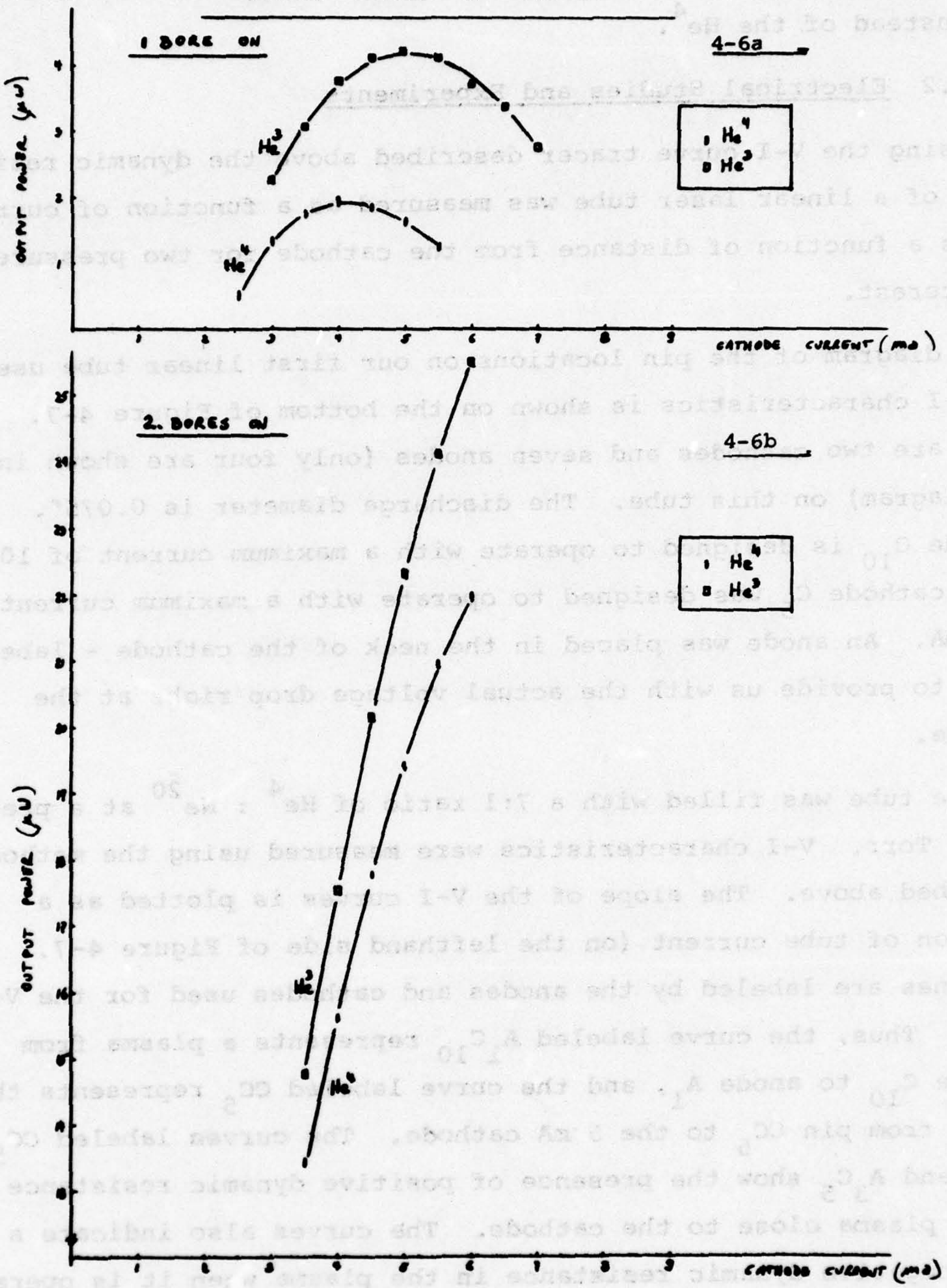

Figure 4-6 Power Output vs. Cathode Current and Helium Isotope

operating the power output is a factor of two greater using the He^3 instead of the He^4.

4.2.4.2 Electrical Studies and Experiments

Using the V-I curve tracer described above the dynamic resistance of a linear laser tube was measured as a function of current and as a function of distance from the cathode for two pressures of interest.

A diagram of the pin locations on our first linear tube used for V-I characteristics is shown on the bottom of Figure 4-7. There are two cathodes and seven anodes (only four are shown in the diagram) on this tube. The discharge diameter is 0.075". Cathode C_{10} is designed to operate with a maximum current of 10 mA while cathode C_5 was designed to operate with a maximum current of 5 mA. An anode was placed in the neck of the cathode - labeled CC_5 - to provide us with the actual voltage drop right at the cathode.

The tube was filled with a 7:1 ratio of $He^4 : Ne^{20}$ at a pressure of 2.0 Torr. V-I characteristics were measured using the method described above. The slope of the V-I curves is plotted as a function of tube current (on the lefthand side of Figure 4-7. The lines are labeled by the anodes and cathodes used for the V-I curve. Thus, the curve labeled A_1C_{10} represents a plasma from cathode C_{10} to anode A_1, and the curve labeled CC_5 represents the plasma from pin CC_5 to the 5 mA cathode. The curves labeled CC_5, A_3C_{10} and A_3C_5 show the presence of positive dynamic resistance in the plasma close to the cathode. The curves also indicate a large negative dynamic resistance in the plasma when it is operated from anodes A_1 and A_2. Thus the negative resistance observed in our plasmas until now is actually composed of a small positive

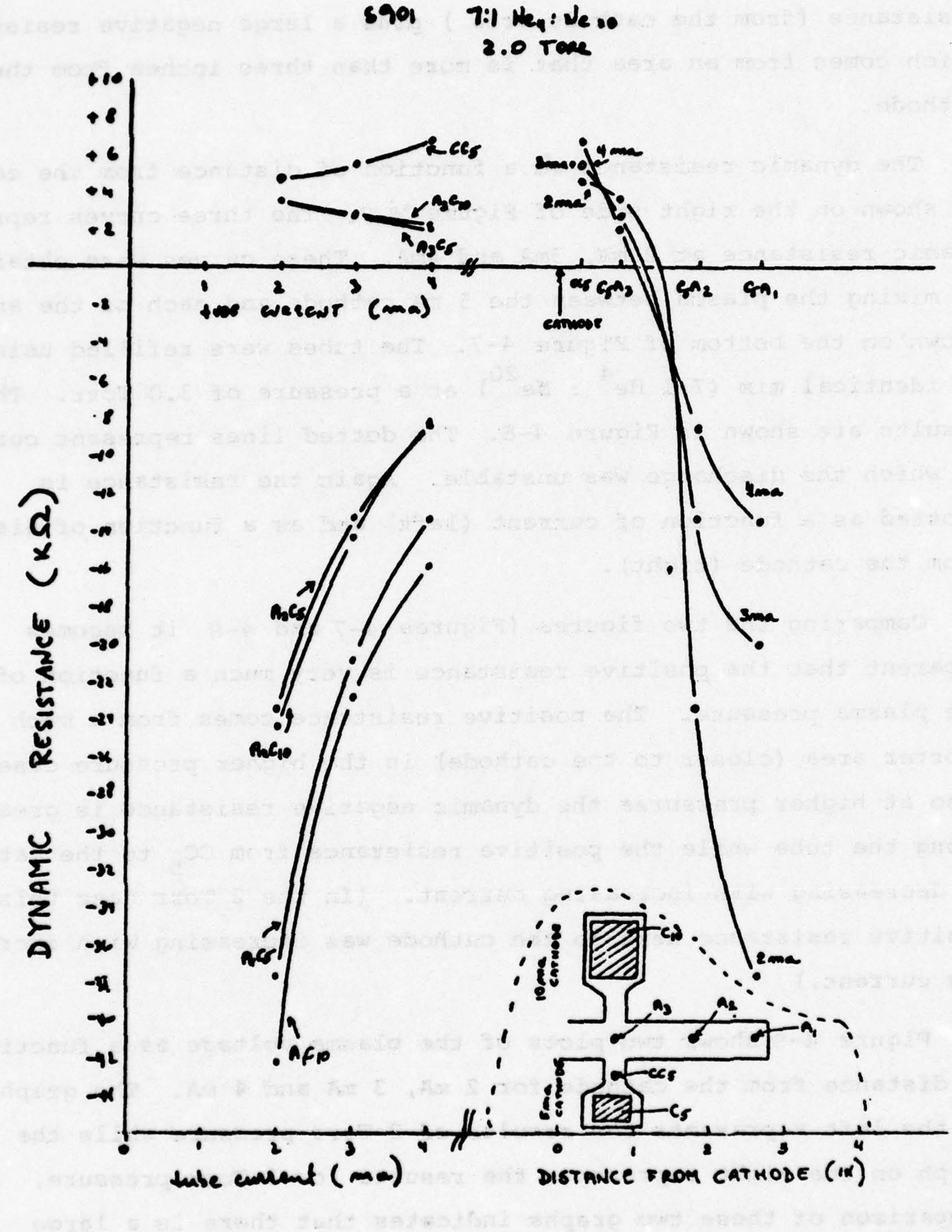

Figure 4-7 Tube V-I Characteristics at P=2.0 Torr; 7:1, He^4:Ne^{20}

resistance (from the cathode area) plus a large negative resistance which comes from an area that is more than three inches from the cathode.

The dynamic resistance as a function of distance from the cathode is shown on the right side of Figure 4-7. The three curves represent dyanic resistance at 2 mA, 3mA and 4mA. These curves were obtained by mixing the plasma between the 5 mA cathode and each of the anodes shown on the bottom of Figure 4-7. The tubes were refilled using an identical mix (7:1 $He^4 : Ne^{20}$) at a pressure of 3.0 Torr. These results are shown in Figure 4-8. The dotted lines represent currents at which the discharge was unstable. Again the resistance is plotted as a function of current (left) and as a function of distance from the cathode (right).

Comparing the two figures (Figures 4-7 and 4-8 it becomes apparent that the positive resistance is very much a function of the plasma pressure. The positive resistance comes from a much shorter area (closer to the cathode) in the higher pressure case. Also at higher pressures the dynamic negative resistance is greater along the tube while the positive resistance from CC_5 to the cathode is decreasing with increasing current. (In the 2 Torr case this positive resistance next to the cathode was increasing with increasing current.)

Figure 4-9 shows two plots of the plasma voltage as a function of distance from the cathode for 2 mA, 3 mA and 4 mA. The graph on the left represents the results of 2 Torr pressure while the graph on the right represents the results for 3 Torr pressure. A comparison of these two graphs indicates that there is a large discrepancy between the two cases (for all three currents) at a distance of half an inch to one inch from the cathode. It seems

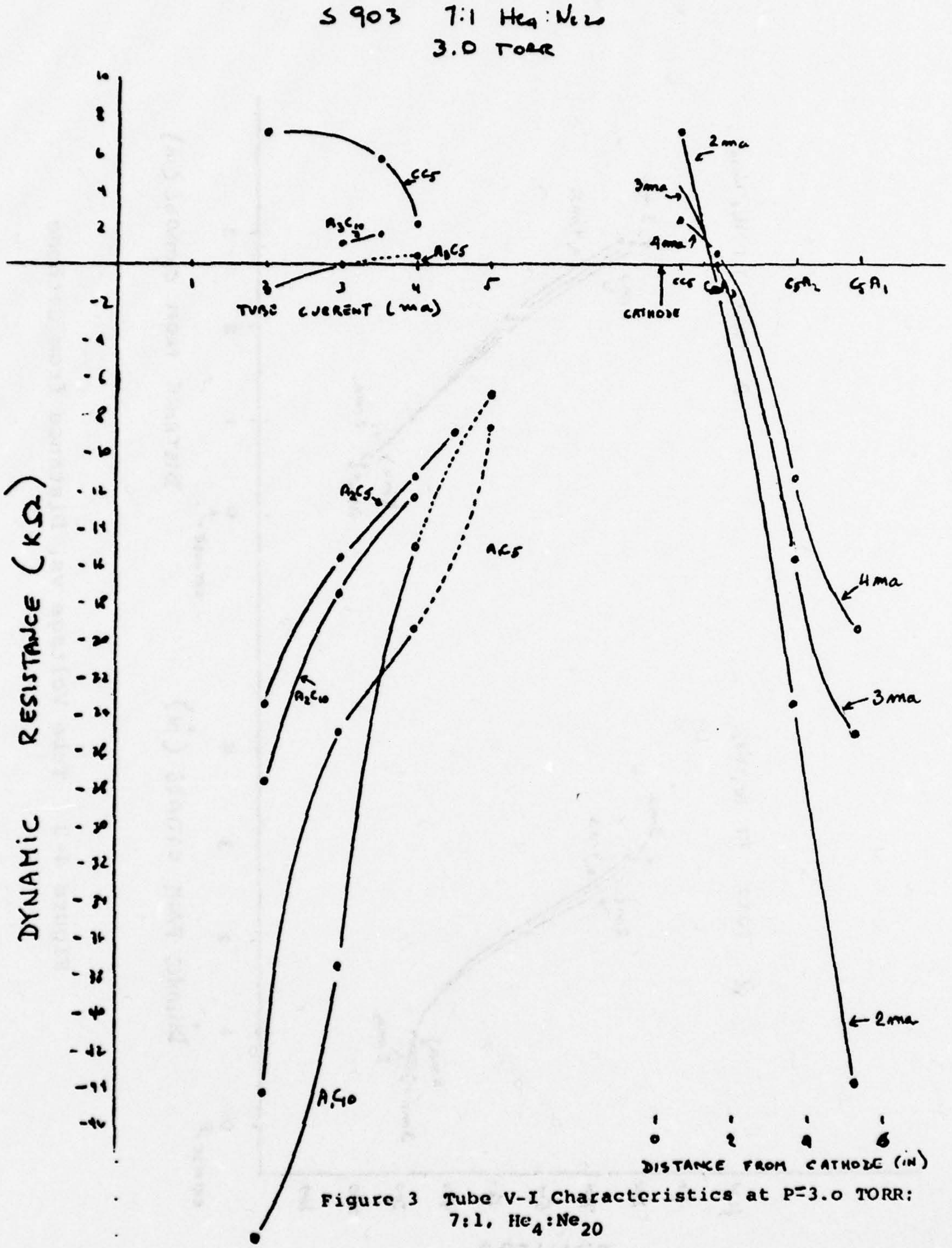

Figure 3 Tube V-I Characteristics at P=3.o TORR: 7:1, He_4:Ne_{20}

Figure 4-8 Tube V-I Characteristics at P=3.0 Torr; 7:1, He^4:Ne^{20}

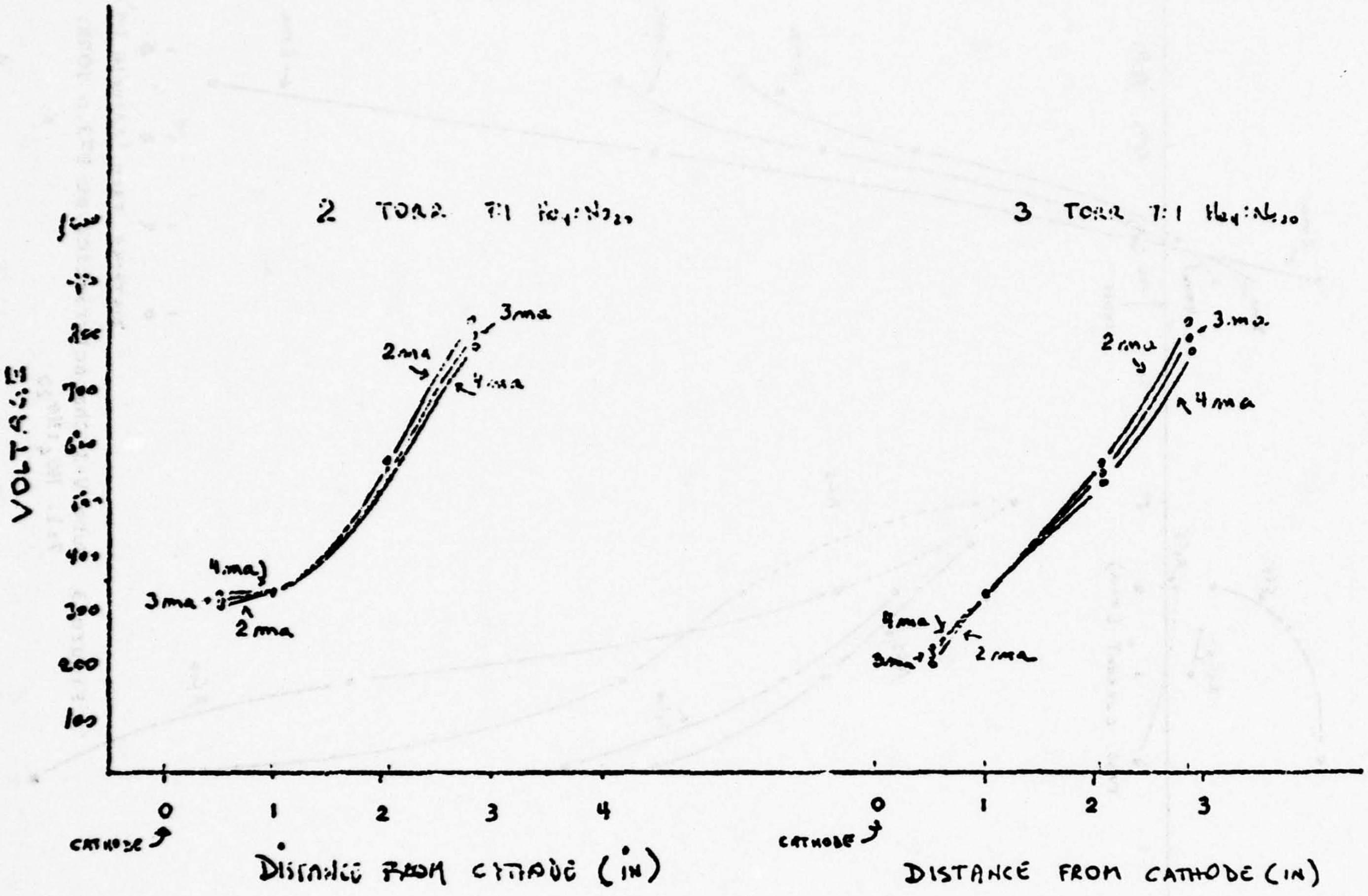

Figure 4-9 Tube Voltage vs. Distance from Cathode

that for the 3 Torr case there is a voltage drop between the test point (anode A_3) one inch from the cathode and the test point (anode CC_5) half an inch from the block. This voltage drop is not present for the lower pressure of 2 Torr. The conclusion that one can draw from this is that the 1/8" diameter tube connecting the cathode envelope to the anode A_3 is of significant resistance at 3 Torr while almost insignificant at the lower pressure of 2 Torr.

The power dissipated by the laser gyro is proportional to the cathode current. To minimize the power dissipated one has to minimize the cathode current. The minimum current that will support a plasma is a function of cathode and anode geometry, cathode and anode capacitance, bore size, gas mixture, gas pressure and gas temperature. Thus one has to look at each of these factors and determine its effect on minimum cathode current.

To determine the effect of ballast resistance on minimum discharge current we ran a HeNe discharge in a laser tube using five sets of ballast resistors. The minimum current required to maintain a plasma in one leg of the discharge was recorded. Ballast resistors chosen for this experiment were 22 KΩ, 51KΩ, 139 KΩ, 156 KΩ and 182 KΩ. The laser tube was operated with the cathode grounded. The bore diameter was 9.5 cm. A plot of the minimum current through one leg (as measured through one anode) for each of the ballast resistances can be seen in Figure 4-10.

It is clear from this graph that one can not keep reducing the current through a discharge by increasing the ballast resistance. It seems that for this tube geometry, gas mix and gas pressure, the minimum current required to sustain a plasma can not be reduced to less than 1.2 mA by increasing the ballast resistors.

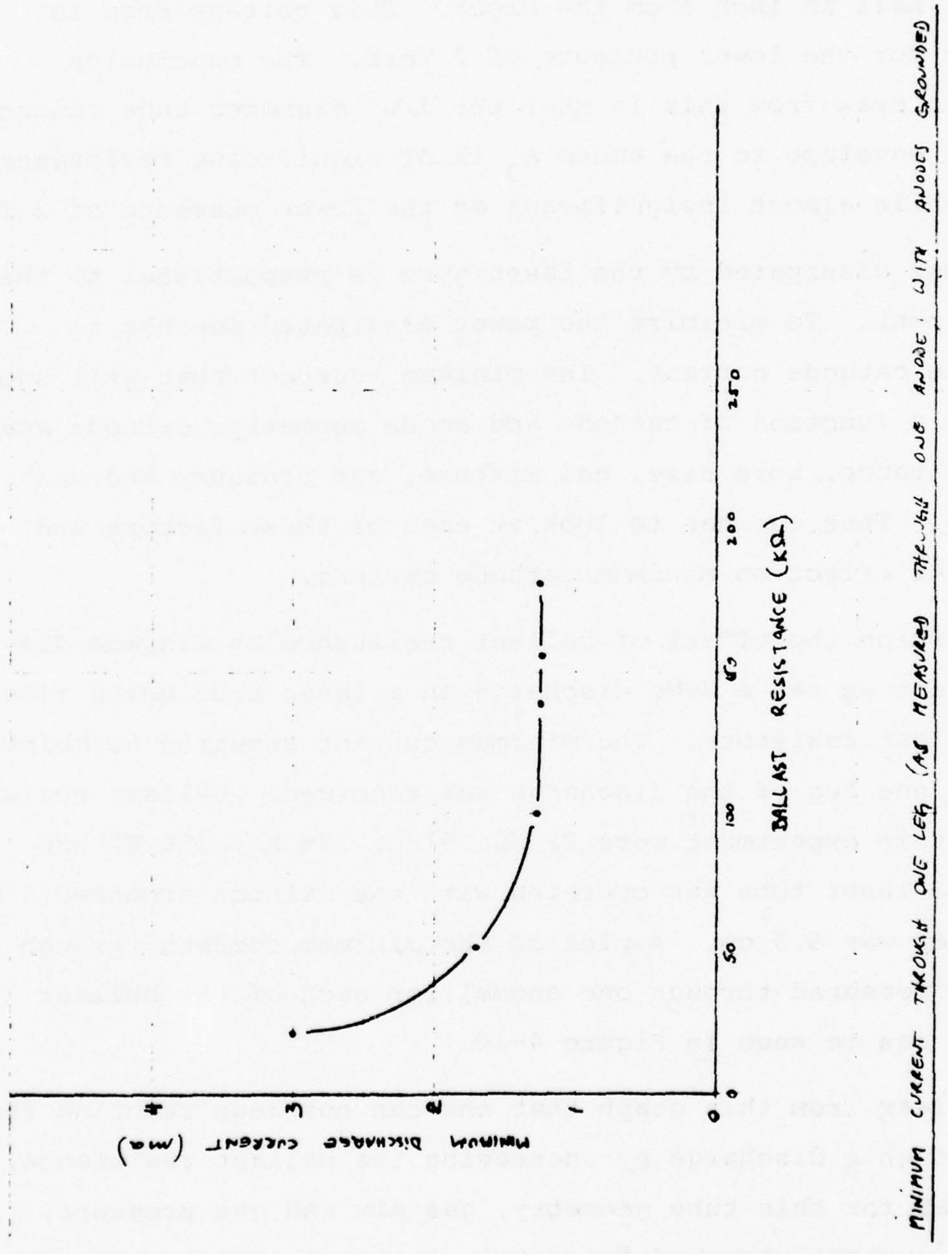

Figure 4-10 Minimum Discharge Current vs. Ballast Resistance

To investigate the effects of tube pressure on minimum discharge current, experiments were performed on a solid block laser gyro. The minimum discharge current for one leg of the plasma was measured as a function of tube pressure. The laser tube was filled with a 10:1 ratio of He^3:(50% Ne^{22} and 50% Ne^{20}) at 2.4 Torr, 3.5 Torr and 4.1 Torr. In addition to measuring the minimum discharge current, the current at which the discharge starts oscillating was also measured. The gyro was operated with 100 KΩ ballast resistors. A graph of minimum and maximum discharge current as a function of tube pressure is shown in Figure 4-11. From these results it seems that for our case (10:1 ratio of He:Ne) the effective operating current window is a function of the tube pressure. The operating window becomes smaller with increasing pressure. However, the minimum current required also drops with increasing pressure.

From an electrical-systems point of view it is important to know the electrical operating parameters of a laser gyro. Experiments were performed to determine the V-I characteristics of an RB-25 laser gyro having a cathode attached by means of glass tubulation. The gyro was filled with an *:0.5:0.5 ratio of He^3 to Ne^{20} to Ne^{22} at a pressure of 3.2 Torr. A plot of the V-I characteristics was obtained. In addition the minimum and maximum (stable) discharge current was investigated as a function of ballast resistance. The output power (through a max. reflecting mirror) was also recorded for the currents of interest. Four different ballast resistors (39 KΩ, 100 KΩ, 139 KΩ and 156 KΩ) were used in the experiment to determine the stable discharge region of the plasma. A plot of the minimum and maximum stable current as a function of ballast resistance can be seen in Figure 4-12. One can see that this gyro behaves similarly to the linear tube tested earlier. In both cases the minimum current decreased with increasing ballast resistance for

Figure 4-11

MINIMUM AND MAXIMUM TUBE CURRENTS VS TUBE PRESSURE

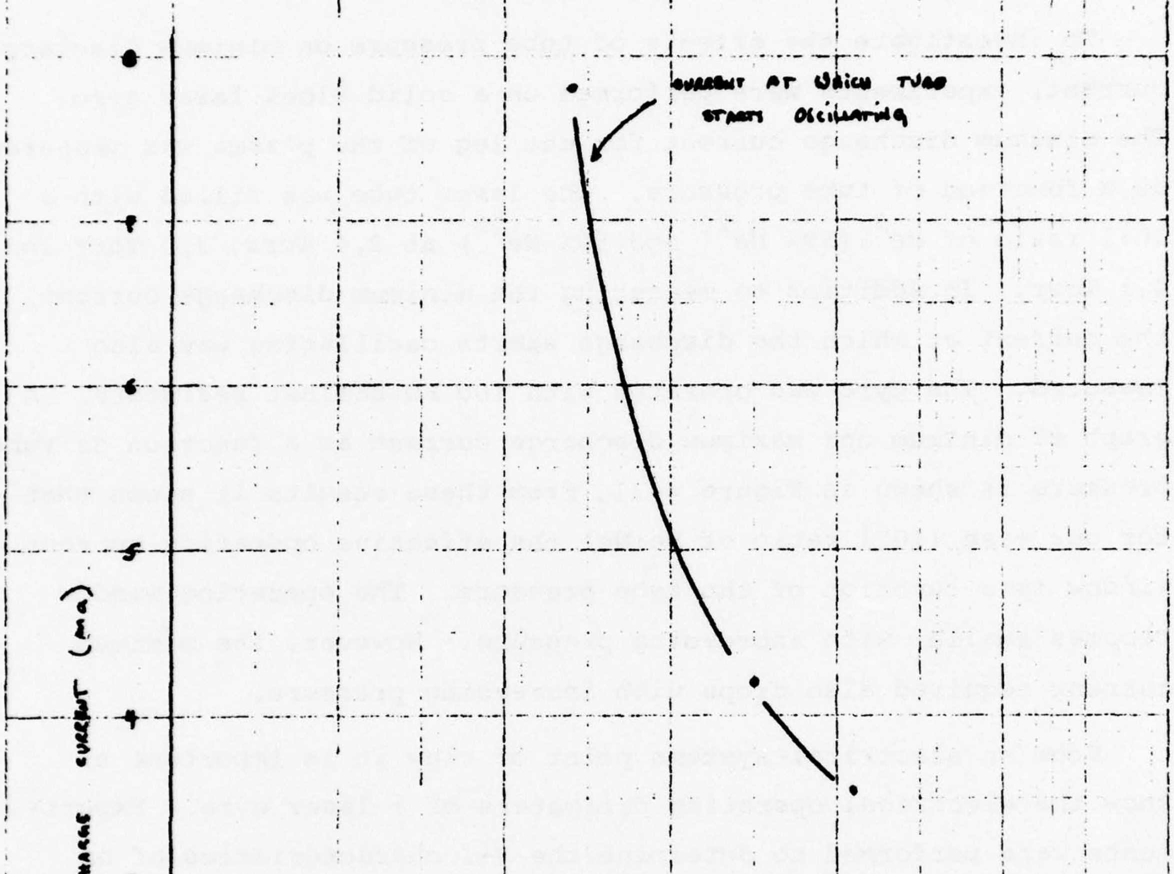

Figure 4-12

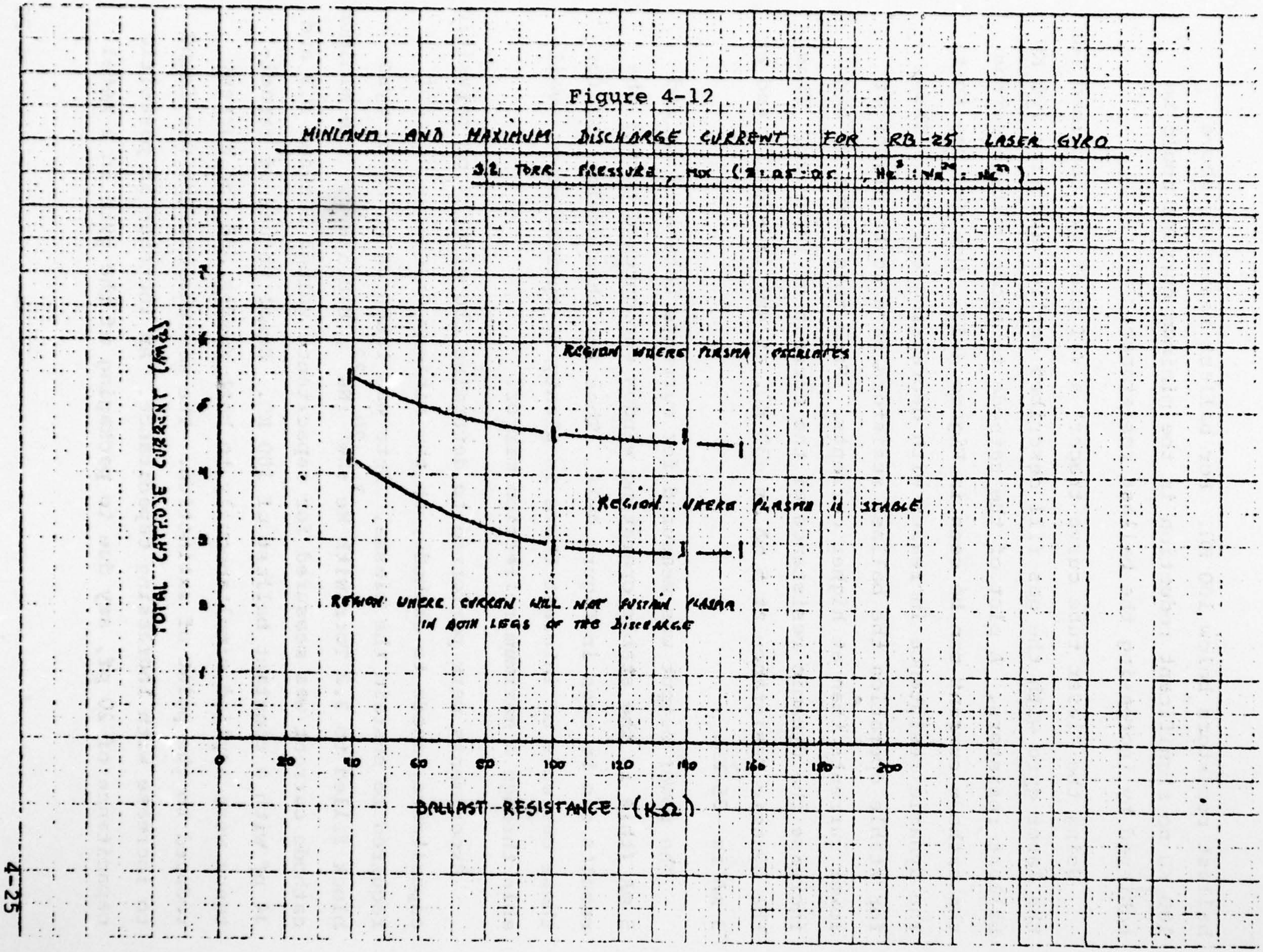

MINIMUM AND MAXIMUM DISCHARGE CURRENT FOR RB-25 LASER GYRO

3.2 TORR PRESSURE, MIX (2:.05:0.5 , $He^3 : Ne^{20} : Ne^{22}$)

ballast resistors below 100 KΩ. For ballast resistors above 100 KΩ no significant reduction in the minimum current could be achieved by increasing the ballast resistance.

Using the "laser tube curve tracer" a V-I plot was obtained for the laser gyro with the gas fill described earlier and with 100 KΩ ballast resistors. A plot of the cathode to anode voltage versus the cathode current can be seen in Figure 4-13. One can see that the dynamic resistance increases with decreasing current. Thus, for stable operation the ballast resistors have to be higher at lower currents than at higher currents. From this curve we can increase the dynamic resistance at the current of interest. Thus the dynamic resistance at 5 mA is -30 KΩ, at 4mA is -32 KΩ, and at 3 mA is -35 KΩ.

The power output was measured for currents between 3 mA and 5 mA (this is the stable operating window encountered above) the results can be seen in Figure 4-14. Thus for this design and for these currents of interest there is plenty of optical power available through a maximum reflection mirror.

Experiments were performed to determine the effects of parasitic capacitance, anode to cathode, on the minimum discharge current required to sustain the plasma. Data was taken on an RB-25 gyro block filled to 3.2 Torr with He^3:Ne^{20}:Ne^{22}, 8:0.5:0.5. The minimum cathode current was measured for capacitance values between 1.3 and 34 pf with a constant ballast of 100 KΩ. Equal values of capacitance were applied simultaneously to both anodes and the current reduced to the point of extinction. The minimum current was found to increase with increasing capacitance. An increase in parasitic capacitance of 20 pf, say due to packaging of the gyro in a metal

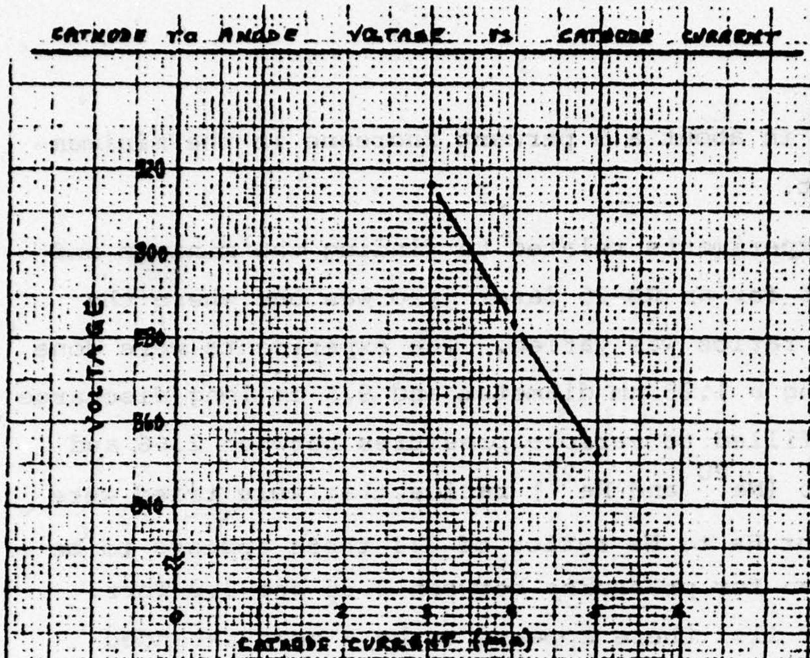

Figure 4-13

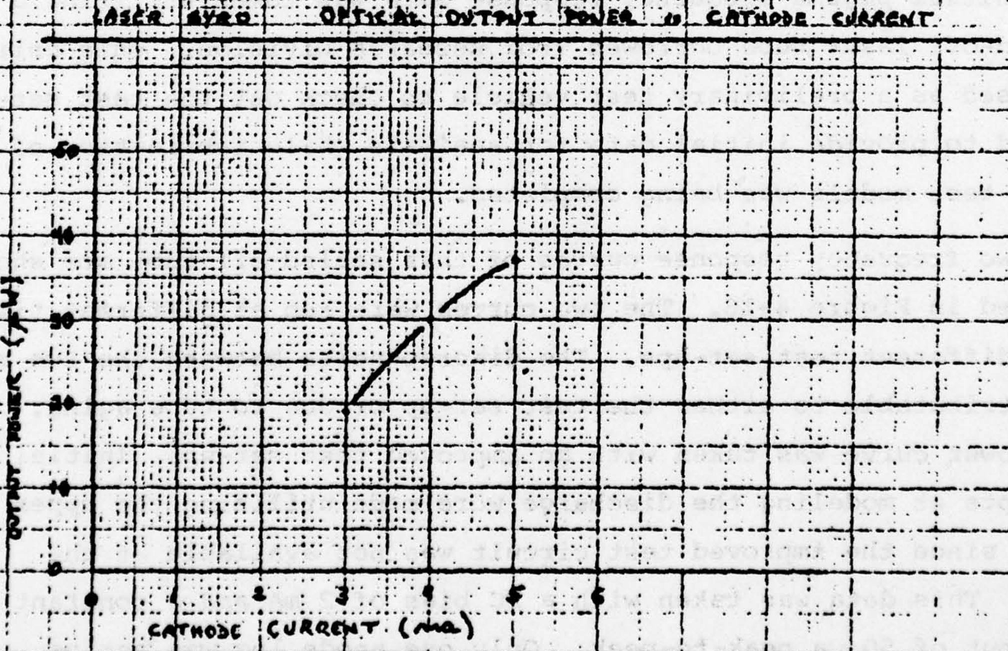

Figure 4-14

housing, would result in about a 5 percent increase in the minimum stable cathode current.

The last set of experiments related to finding the minimum and stable maximum current for an RB-25 laser gyro was one where the pressure and He to Ne ratios was varied. The experiments were done on a linear tube having a 1.25 nm diameter and 9.5 cm long discharge bore. This tube was filled to various pressures between 2.66 and 3.58 Torr. The He^3 to (Ne^{20} and Ne^{22}) ratios that were tried were 11:1, 8:1 and 5:1. For He to Ne ratios of 8:1 there appears to be stable operating region for pressures between 2.66 and 3.2 Torr. For He to Ne ratios of 11:1 there appears to be a more extended region of stable operation extending from 2.66 Torr to about 3.7 Torr. These relationships can be seen in Figure 4-15.

4.2.4.3 Discharge Modeling

Initial plasma frequency response data was taken utilizing a sealed-off laser tube borrowed from Research Division. This unit was used as a preliminary test vehicle to check out the test set-up and to provide initial data for analysis while fabrication of other test models was being completed.

Two frequency response curves of this sealed-off tube are shown plotted in Figure 4-16. The two curves were run at different times with different test set-ups. The discrepancies between the two may be attributable to either the test set-up or due to tube aging. The lower curve was taken with an improved test set-up. Initial attempts at modeling the discharge were made utilizing the upper curve since the improved test circuit was not available at the time. This data was taken with a DC bias of 2 mA and a constant AC input of 50 μa peak-to-peak. Only one anode leg was active.

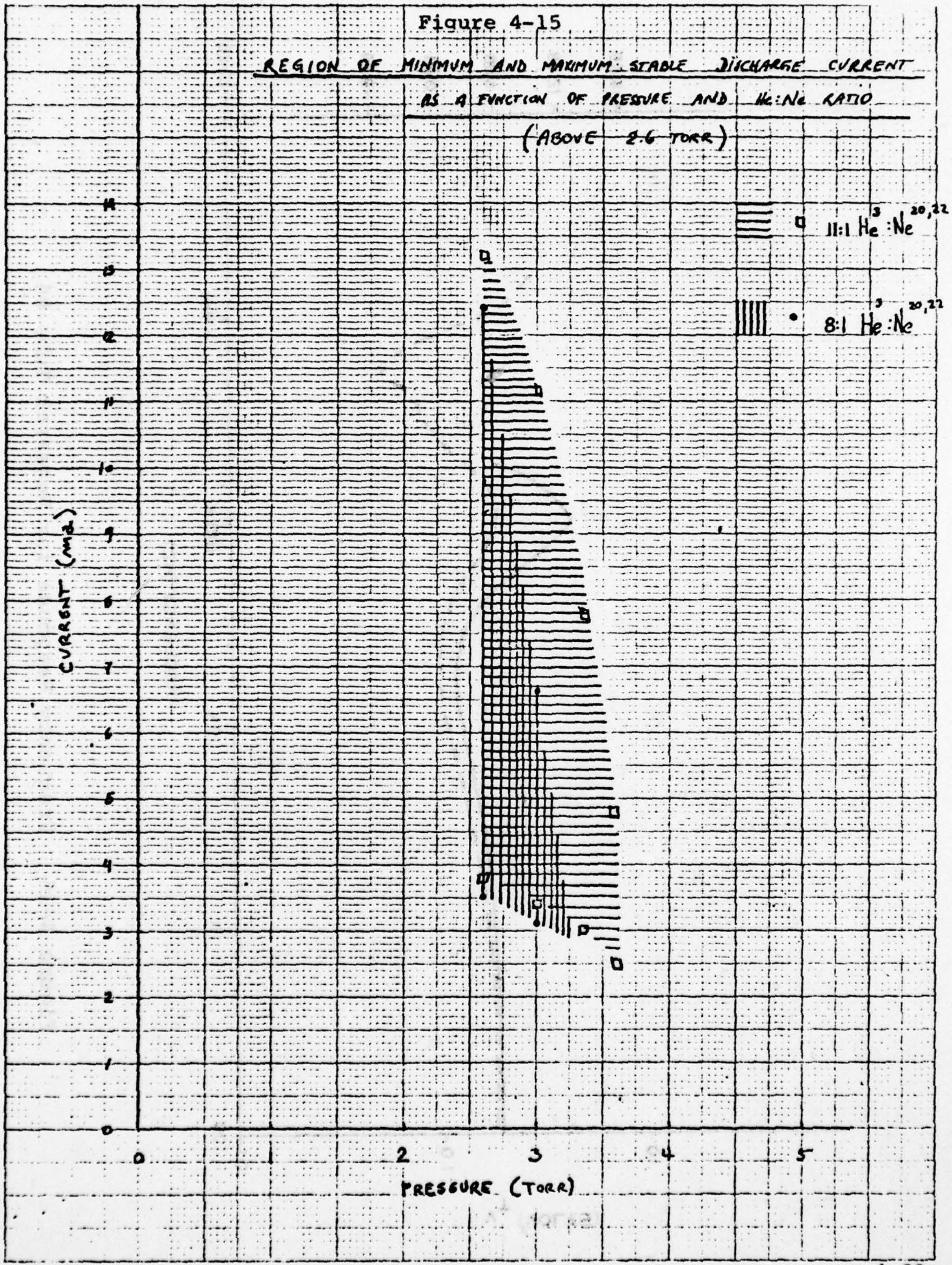

Figure 4-15

REGION OF MINIMUM AND MAXIMUM STABLE DISCHARGE CURRENT AS A FUNCTION OF PRESSURE AND He:Ne RATIO

(ABOVE 2.6 TORR)

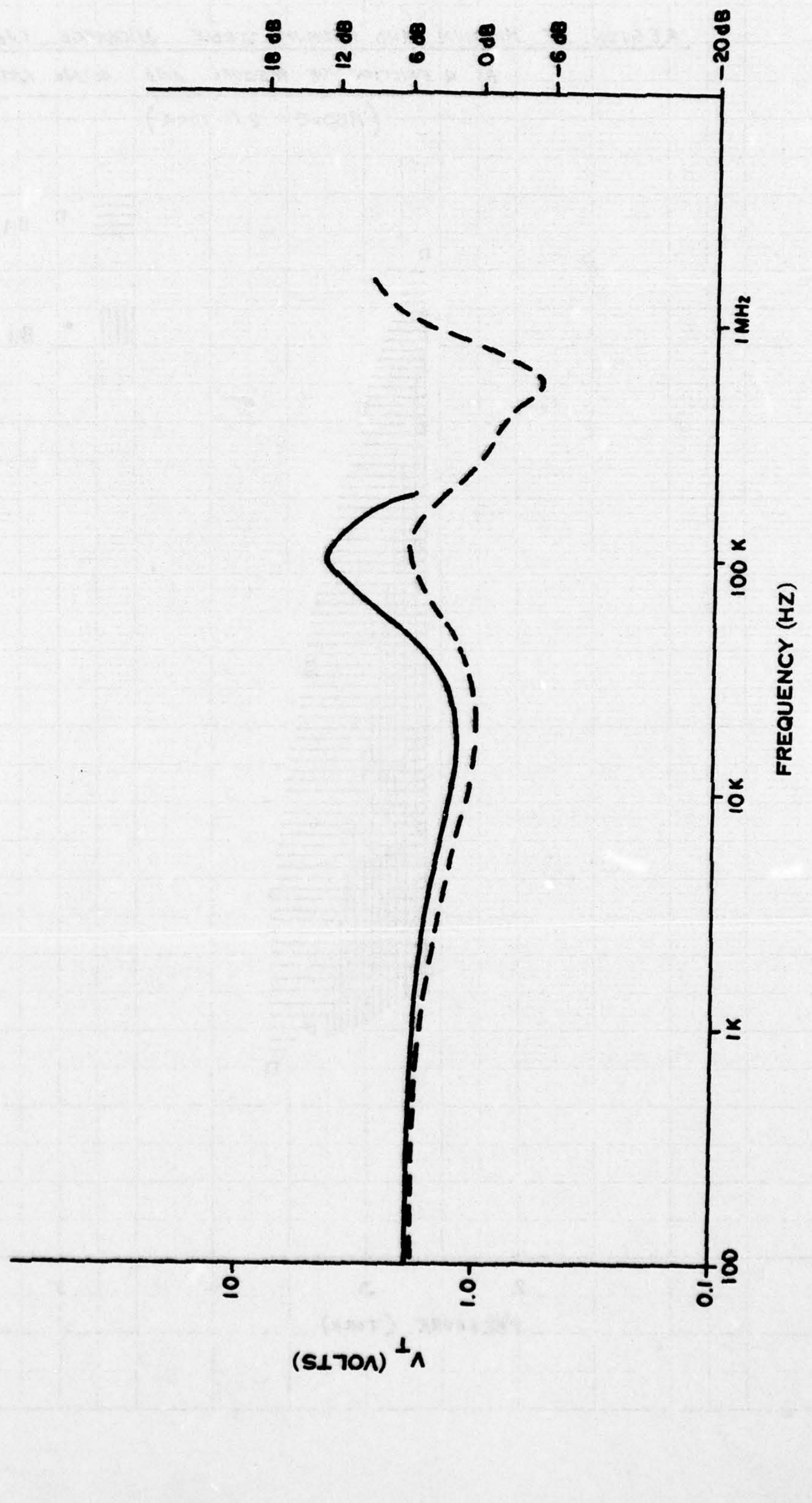

Figure 4-16 Frequency Response for Research Tube #4

The topology shown in Figure 4-17 was selected based upon the general magnitude characteristics of the data. A resonant RCL network providing a high frequency peak at $1/2\pi\sqrt{L_pC_p}$ = 100 KHz. The lower frequency dip is controlled by the parallel R_cL_c network adding an additional pole-zero pair to the circuit response. The DC resistance (R_p) is negative and equal to -44 KΩ. The remaining component values were selected based upon an intial hand analysis and then modified to improve the fit of the resulting circuit response. A TRAC program was used to obtain the circuit response for each iteration. The magnitude response for this topology with the indicated component values is also included in Figure 4-17. Attempts to improve the fit further were not attempted since the new data (lower curve, Figure 4-16) indicated a more complex topology. Figure 4-18 includes C_C and L_{CS} to provide the additional peak at 1.5 MHz. Availability of the multi-anode test models enabled the different regions of the tube to be investigated. A Bode plot of the cathode region and one of the overall tube response using ZAP1 and the anode place at L/2 resulted in the curves shown in Figure 4-19. The broken line is the cathode region, the solid line being the overall tube response. The resistance of the cathode region is positive and its impedance increases with frequency. The overall resistance of the tube is negative indicating that the DC negative resistance of the discharge occurs in the positive column.

Comparison of the phase response of the above topology to that of the tube itself showed significant discrepancies. This result along with the increasing complexity of these topologies provided the incentive to investigate computer-aided curve fitting routines.

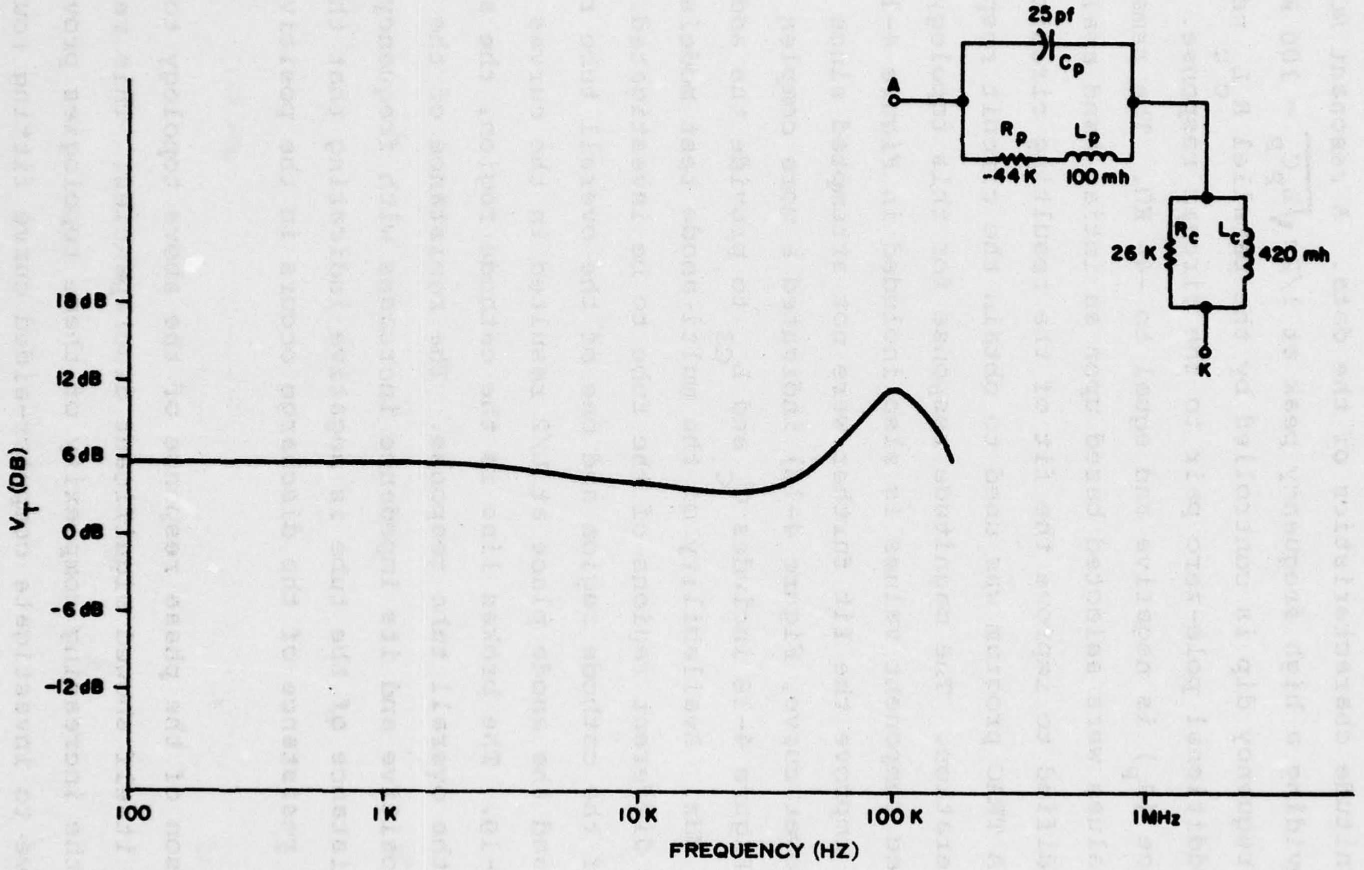

Figure 4-17 Topology to Fit Magnitude Characteristics of Impedance

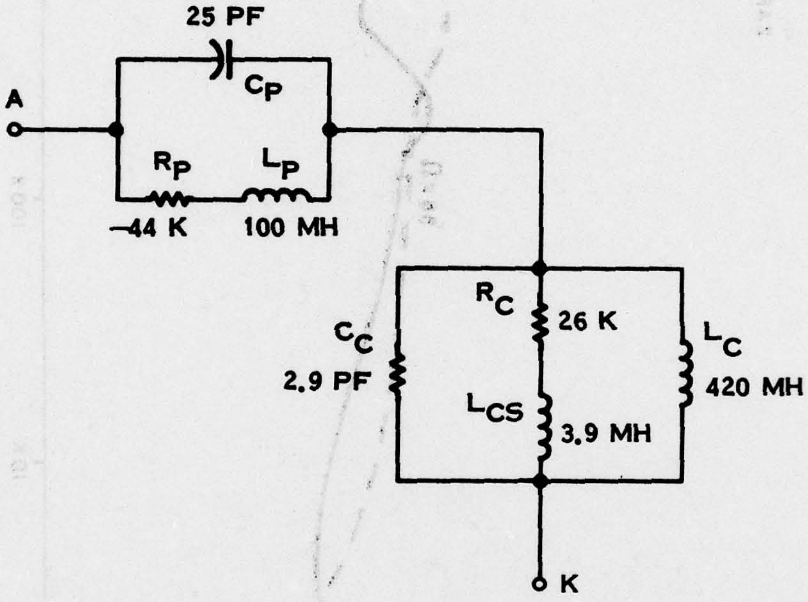

Figure 4-18 Topology Required to Include Additional Peak at 1.5 MHz

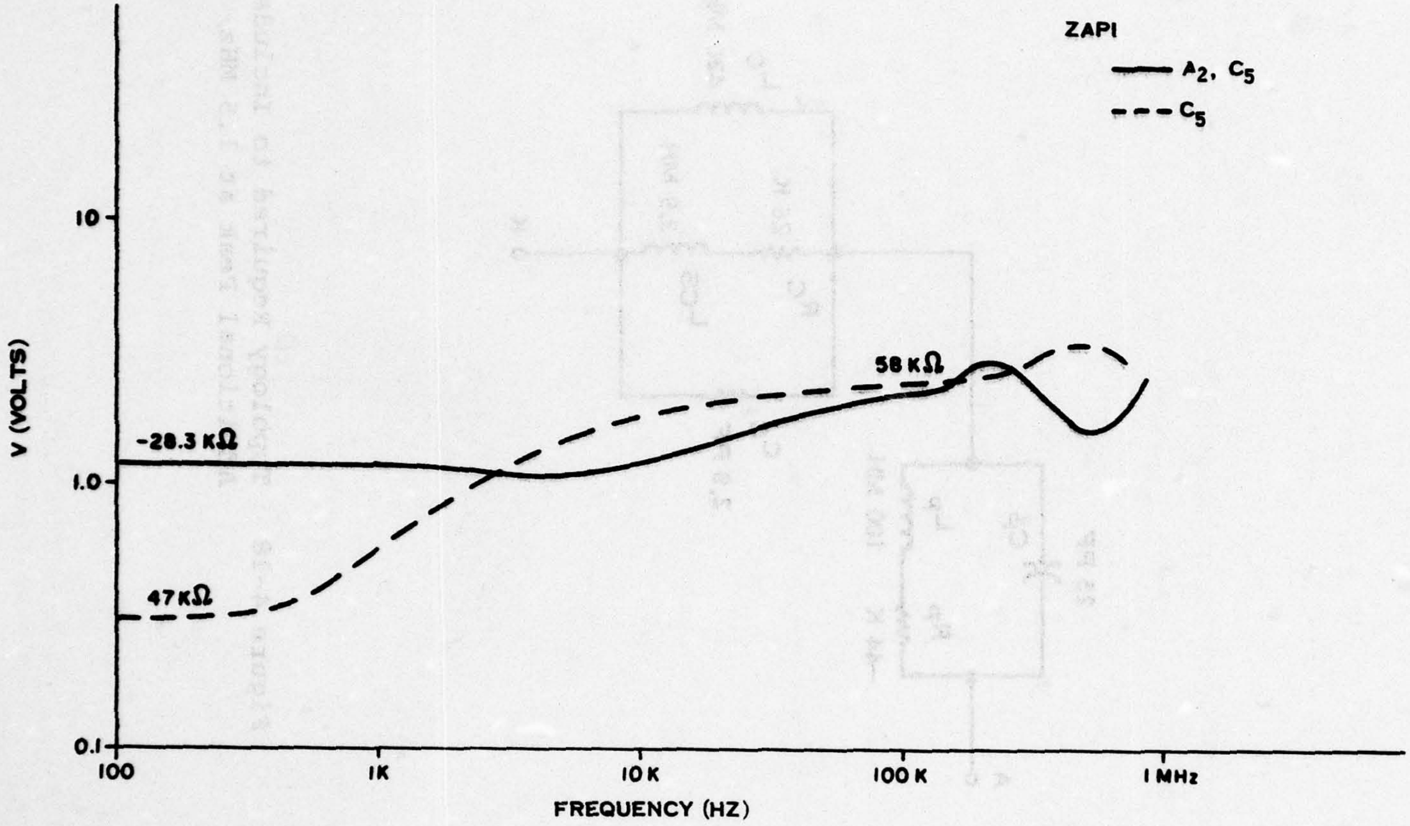

Figure 4-19 Frequency Response of ZAP1

A search of general purpose in-house computer programs was initiated to identify those applicable to this task. Two such programs were selected for evaluation. One of these, XSPA, intended as an optimization routine for filter networks, was purported to, given a circuit topology and starting values for the circuit components, provide those component values that yield the best fit of a given response curve. The second program, RATFIT, using frequency response data as the input, solves for the equation that best fits the data expressed as the quotient of two polynomials (the highest order polynomial that can be handled is five). Determination of the component values from the coefficients of the polynomials would be done by hand.

Test cases having known solutions were run on both programs. XSPA would not converge to a solution for any of the cases tried and was therefore discarded. RATFIT would converge for cases having known solutions, but had difficulty handling the laboratory data. Rather than try to troubleshoot and/or modify these existing programs, it was decided to develop new software directly applicable to the problem at hand. Initial work concentrated on developing a program to determine the equation that best fits the data, expressed as the quotient of two polynomials (similar in intent to RATFIT). The algorithm used was based on a method proposed by Levy in 1959*. The data points are converted to complex numbers $D_i(S)$, and the object is to find polynomials P(S) and Q(S) such that

$$D_i \cong \frac{P(S_i)}{Q(S_i)}$$

Levi's method linearizes the problem by defining the errors as

---

*Levy, E. C., Complex Curve Fitting. IRE Transactions on Automatic Control, May, 1959.

$$e_i = D_i\,Q(S_i) - P(S_i)$$

With this form, the weighted sum of squares of the errors is seen to be a biquadratic function of the P,Q coefficients, hence the partial derivatives with respect to the coefficients leads to a solvable set of linear equations. This linearization is achieved, unfortunately, at the expense of inadvertently weighting the errors by the (complex) magnitude of the denominator Q, which of course is not known beforehand. Since we are trying to fit data which have interesting behavior over four decades of range in S, the Q polynomial will in general also vary by many orders of magnitude. Thus, the unmodified algorithm tends to over-fit the high frequency data and to nearly ignore the low frequency data.

The modification which overcomes this problem is to counter-weight the errors by feeding back estimates of the Q magnitude. Thus, the k^{th} solution yields a denominator $Q_K(S)$, the inverse magnitude of which becomes the weight for the $(K+1)^{st}$ solution. Preliminary tests with both simulated and real data showed that this method converges quickly, although some trickery (e.g., temporarily ignoring the high frequency data) was needed to get a good initial solution.

This curve-fitting technique, while successful, had two undesirable characteristics. The first is that it did not sharply distinguish the minimal degrees of the transfer function numerator and denominator needed to adequately fit the data. For example, if 6^{th} degree over 6^{th} degree polynomials fit the data fairly well, then 7^{th} over 7^{th} could be counted on to fit the data at least slightly better. Thus, it was impossible in a practical way to distinguish fit improvements corresponding to real equivalent components, from fit improvements due solely to accommodation to data noise. The second problem was that, for a given polynomial fit, the translation of fit coefficients into circuit topology is not unique.

Thus, while the generalized method was kept in reserve for verification, the curve-fitting methods were revised to a synthetic format, with components and topologies selected to fit recognizable features of the complex frequency response data. The transfer functions for given trial circuits were programmed specifically rather than generally, and weighted least-squares curve fitting was used to optimize the coefficients within selected frequency bands. Although this method involved as much art as science, it became fairly easy to "build" the data-matching circuit by fitting simple circuits to the low-frequency data, observing the residuals between data and fit at all frequencies, adding circuit components and re-fitting the low- to middle-frequency data, and so on until a satisfactory fit over the entire frequency range was realized. The validity of this method was reinforced by the fact that topologies developed to fit data for a given laser configuration could later be used to fit other data taken for the same configuration with differing parameters. In other words, the equivalent circuit topology, once found, appeared to be an invariant for a given test set-up.

Figure 4-20 shows a complex plane plot of the frequency response of the cathode region of the RB-25-0002 gyro block. This data was generated utilizing an anode pin in the neck of the cathode bulb assembly. An input signal of 50 μa p-p was used with a DC bias of 2 mA. The block was filled to 3.2 Torr with $He^3:Ne^{20}:Ne^{22}$ in a ratio of 8:0.5:0.5. Utilizing the computer techniques described

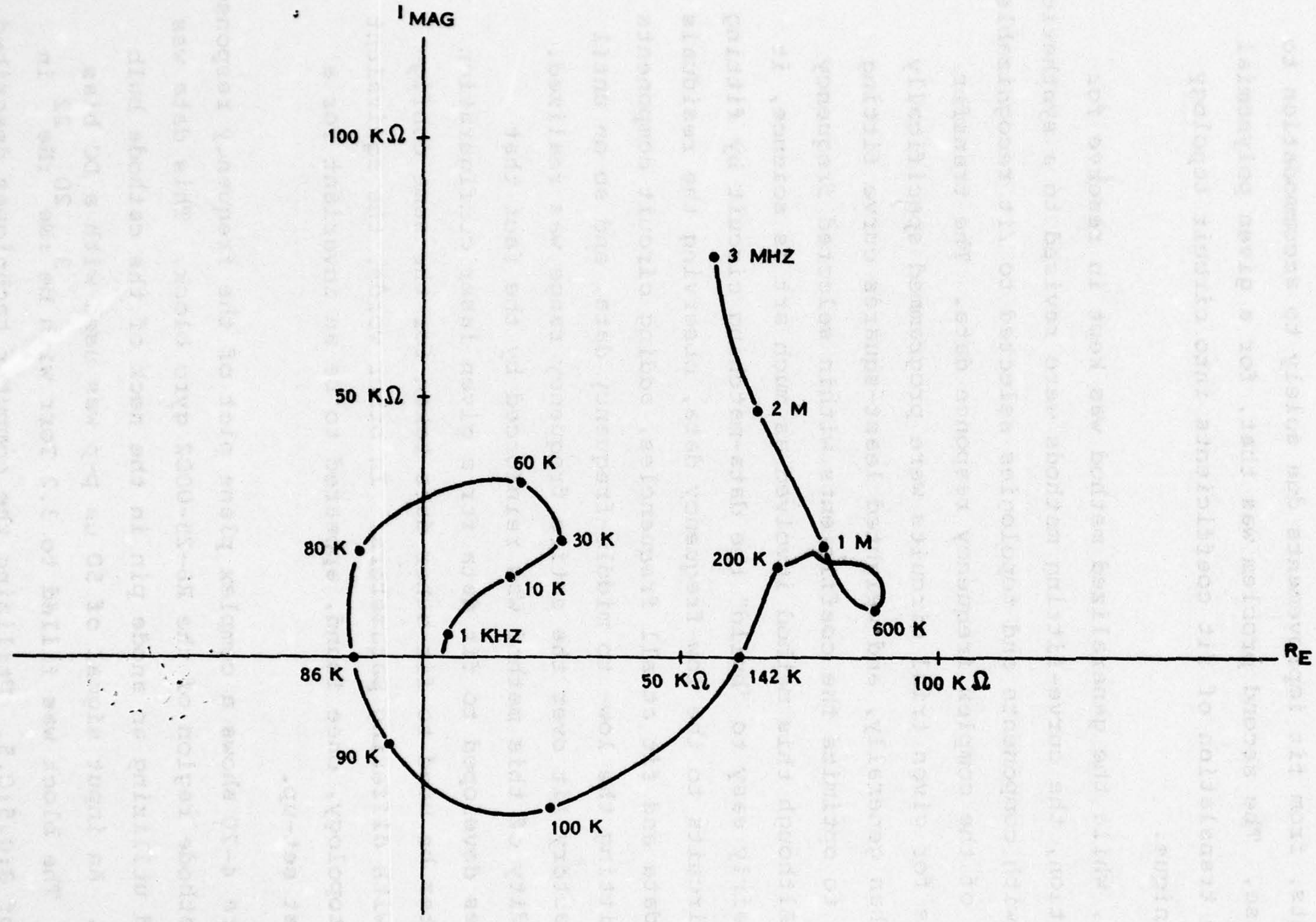

Figure 4-20 Frequency Response of RB-25-0002 Cathode Region

in this section, the topology shown in Figure 4-21 was generated. The two parallel LR networks dominate the response in the 1 KHz range. The counterclockwise spiral is controlled by the resonant RLC network with the high frequency characteristics being dominated by the series L (3.8 mh). The response of this topology is also plotted in Figure 4-21. Figure 4-22 shows a frequency response of the same tube but including the positive column. The characteristic cathode spiral can be seen to dominate up to about 150 KHz. The positive column shifts the entire plot to the left resulting in a negative resistance at DC. It also modifies the response significantly above 150 KHz. The topology and component values of Figure 4-23 provide the fit to this data as indicated in Figure 4-22. The net modifications to the topology necessary to include the positive column, then, are a series negative resistance and an additional four-element RLC resonant circuit containing an additional negative resistance. The component values describing the cathode region are somewhat different from those given in Figure 4-21. This is due to the fact that the latter frequency response was run at a somewhat higher DC current (3.0 mA) and also with another fill the parameters of which were the same except that the cleanliness or quality of the second fill is not necessarily identical to that of the first. As a matter of fact there appears to be a strong correlation between the AC characteristics of the plasma and the age or color of the fill.

Figures 4-24 and 4-25 are frequency responses of the RB-25 block at 1.8 mA DC bias and all filled to 3.0 Torr 8:0.5:0.5 $He^3:Ne^{20}:Ne^{22}$. The color of the first fill was intense orange. The block was pumped on overnight prior to filling. The color of the second fill was a less intense orange tending toward pink. This fill did not have the benefit of an overnight pump. It should

AD-A062 257 RAYTHEON CO SUDBURY MASS EQUIPMENT DIV F/G 17/7
MULTIOSCILLATOR RING LASER GYRO.(U)
SEP 78 A ZAMPIELLO, D PASIK F33615-76-C-1218
UNCLASSIFIED AFAL-TR-78-133 NL

2 OF 2
AD
A062257

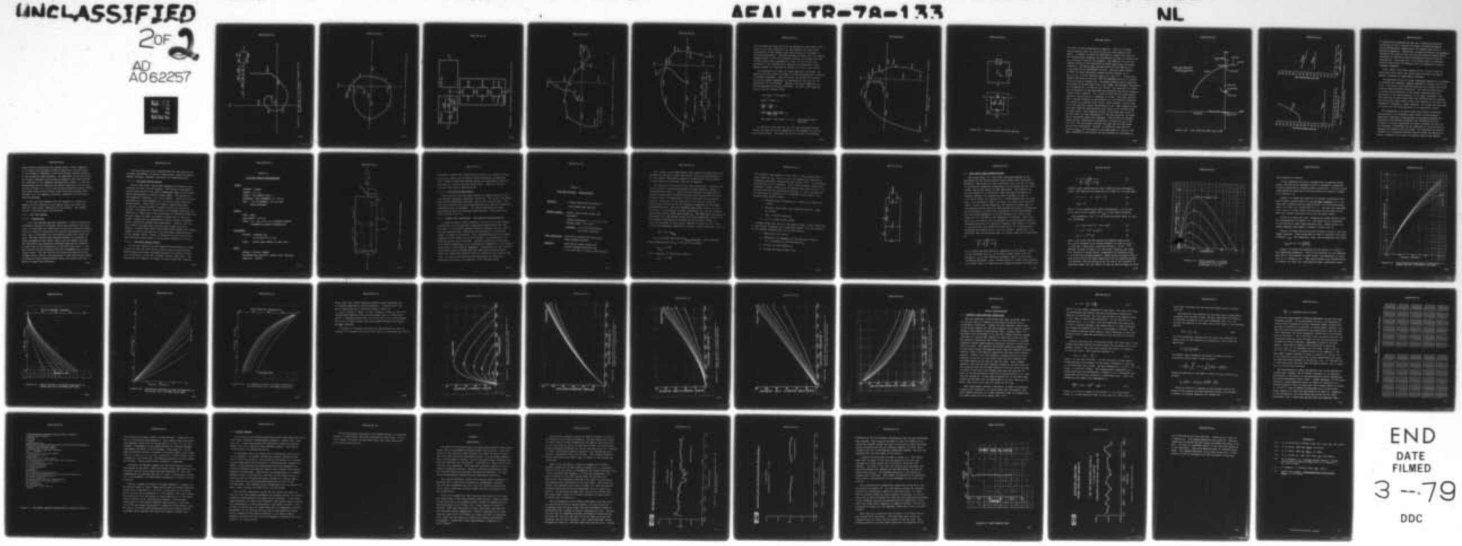

END
DATE
FILMED
3 -- 79
DDC

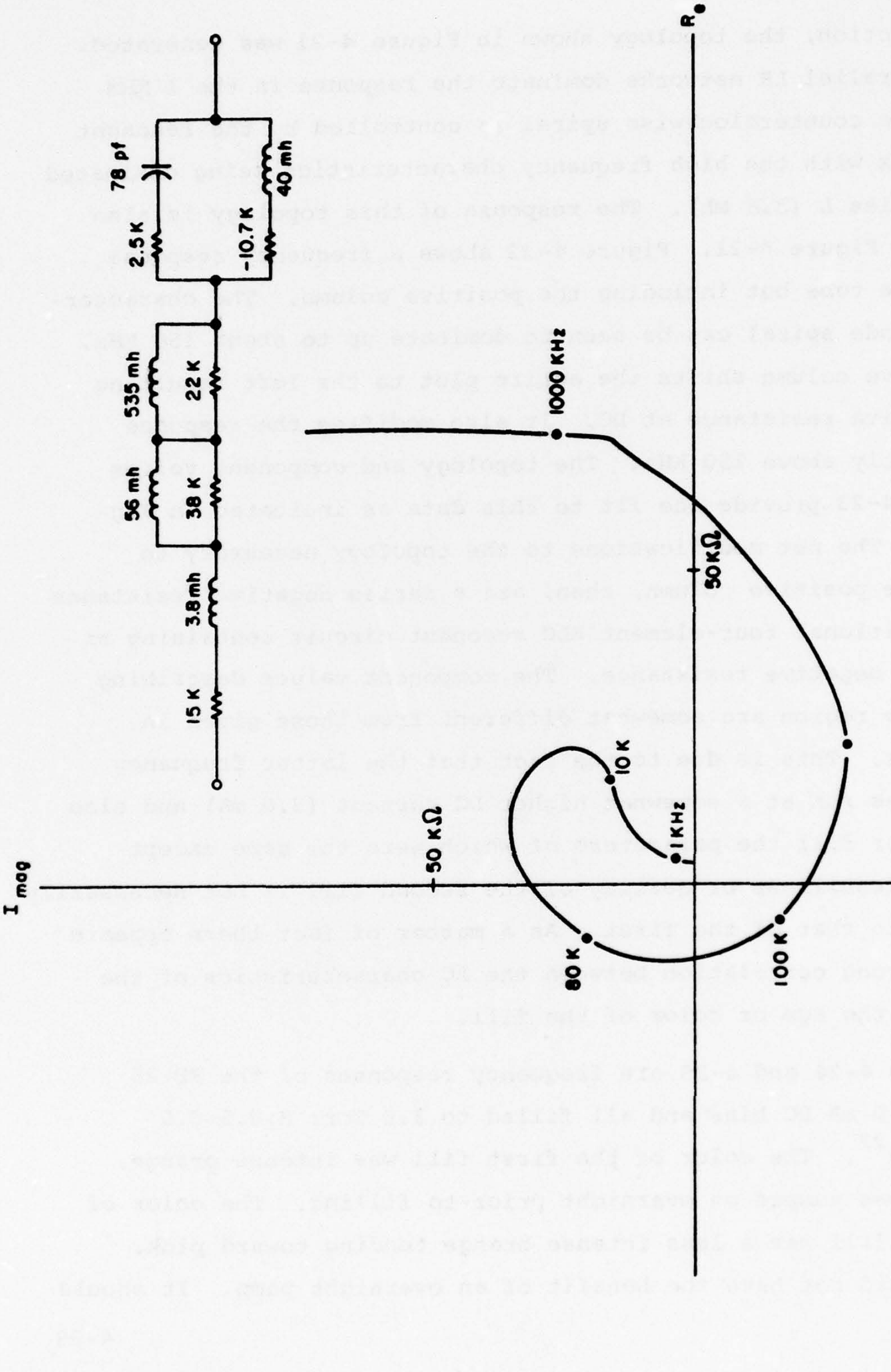

Figure 4-21 The Topology and Its Frequency Response for the Cathode Region of RB-25-0002

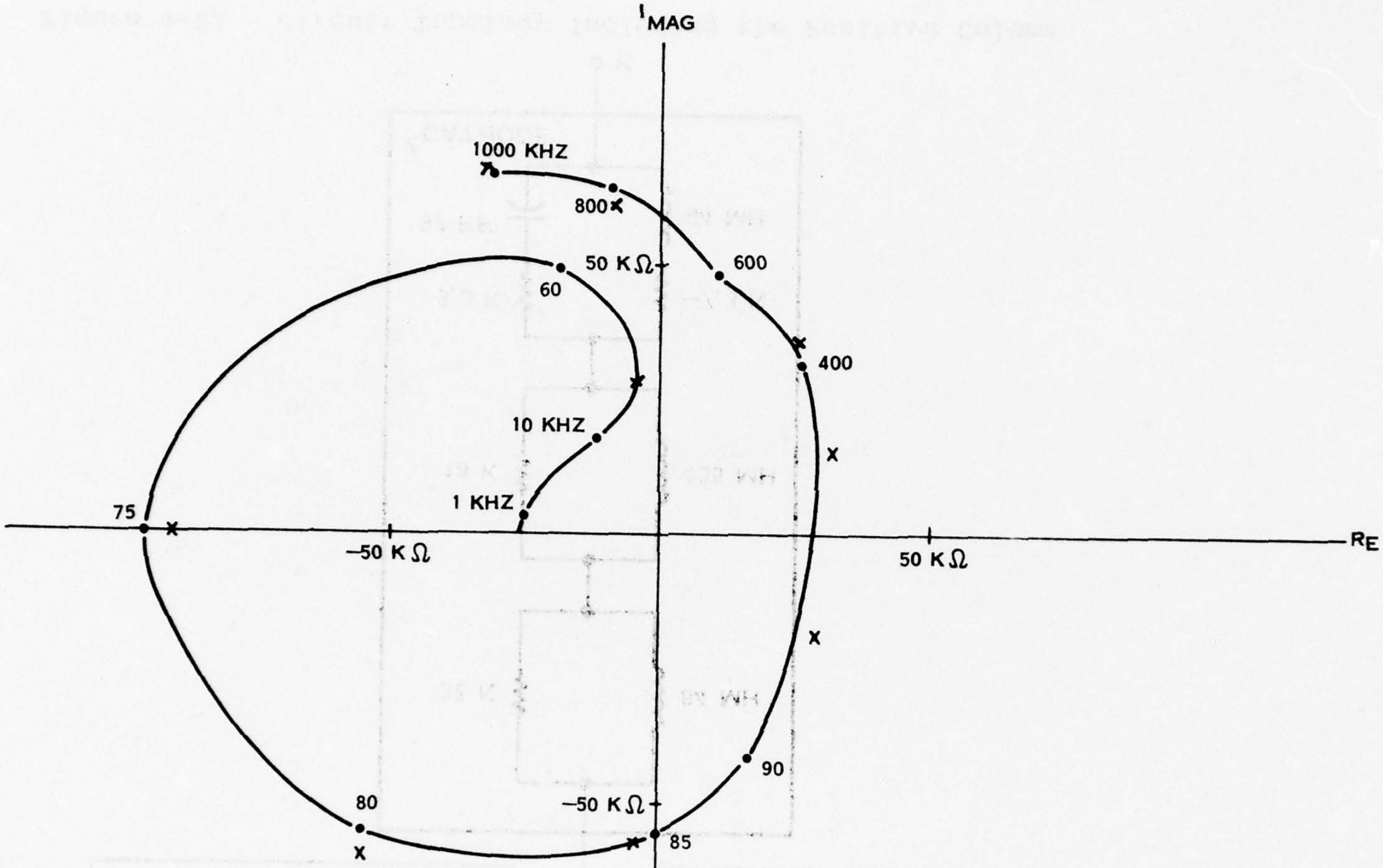

Figure 4-22 Overall Response of the RB-25-0002 with Resulting Fit

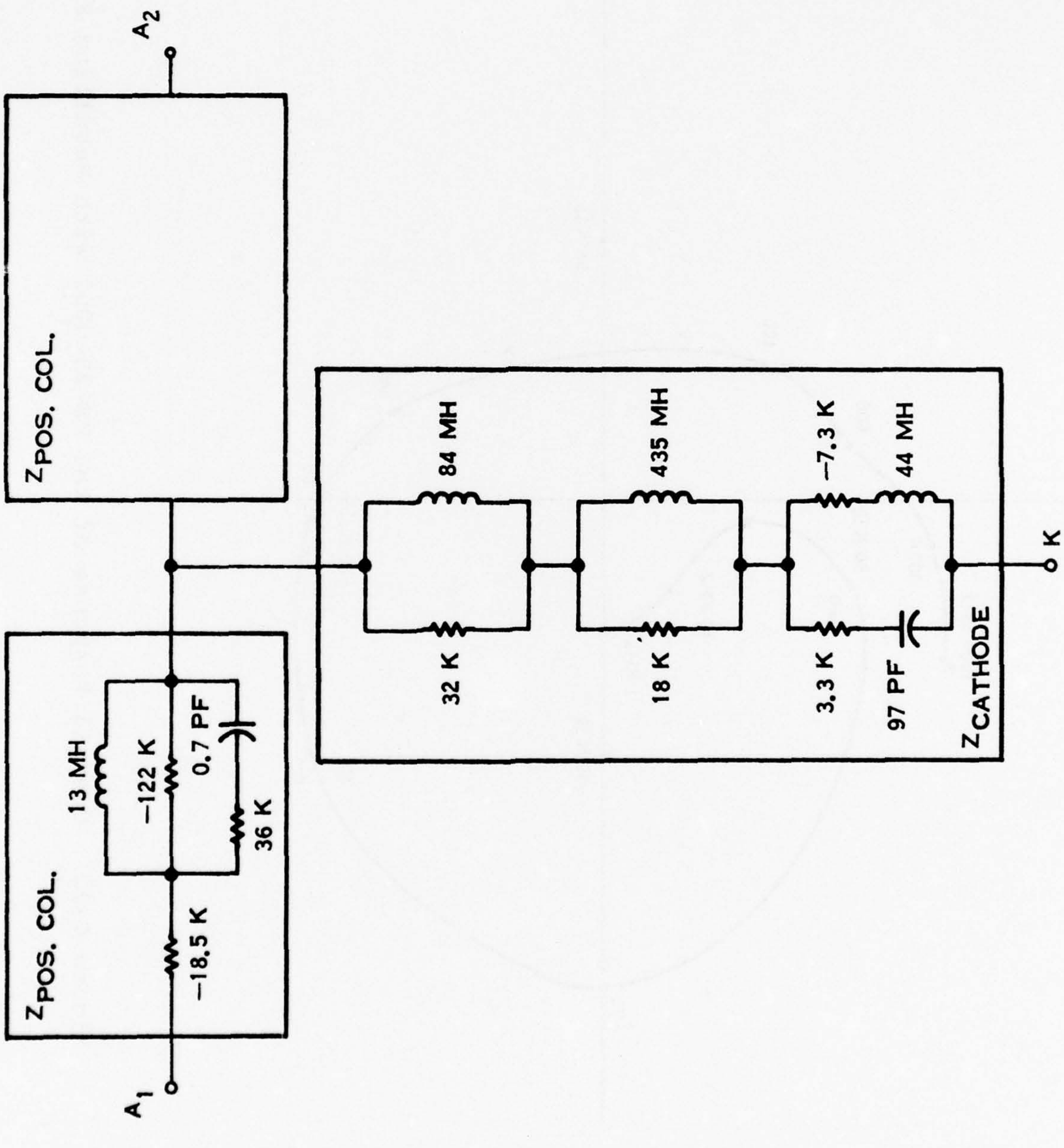

Figure 4-23 Circuit Topology Including the Positive Column

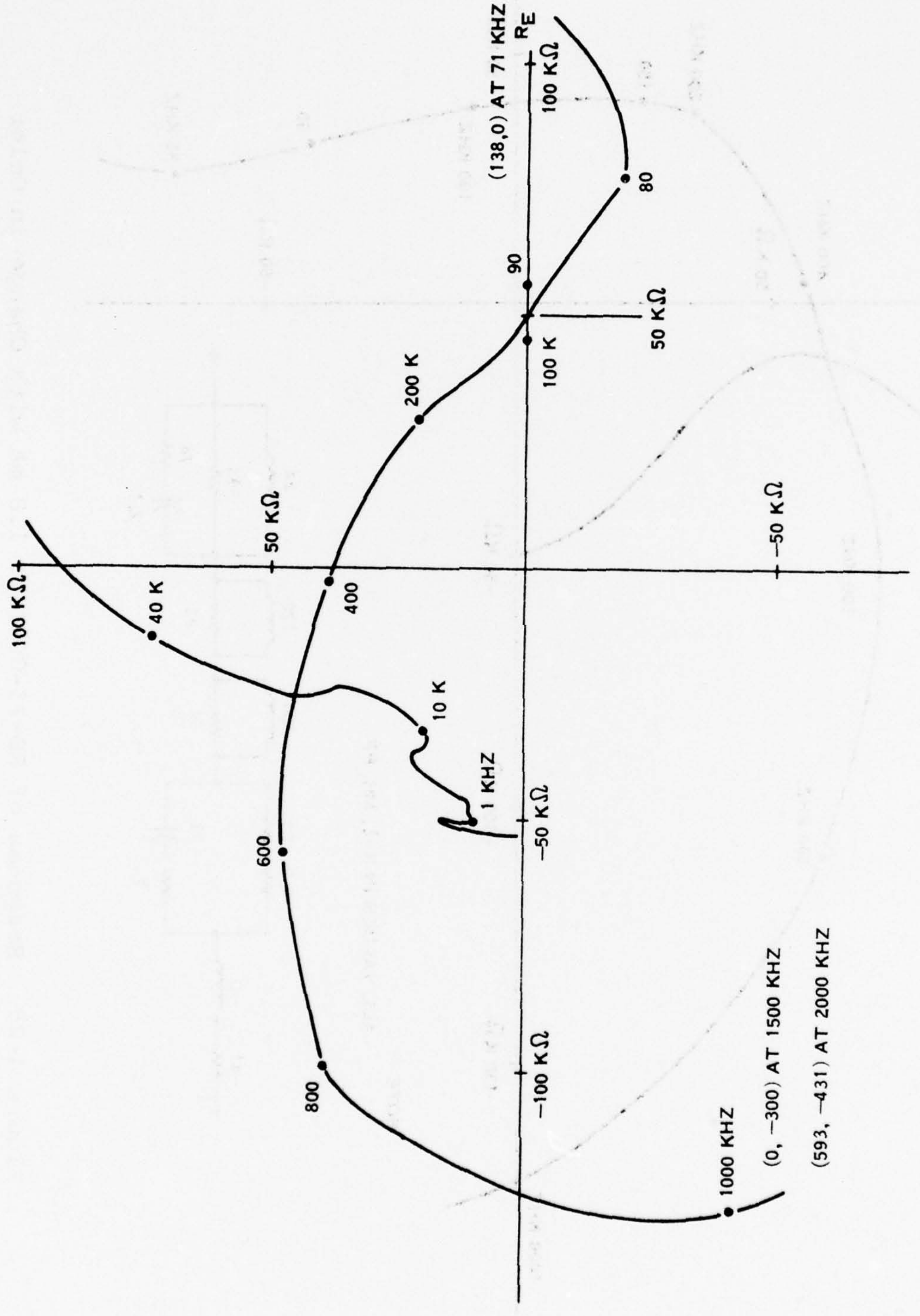

Figure 4-24 Response of RB-25-0002 at 1.8 mA DC with Fresh Fill

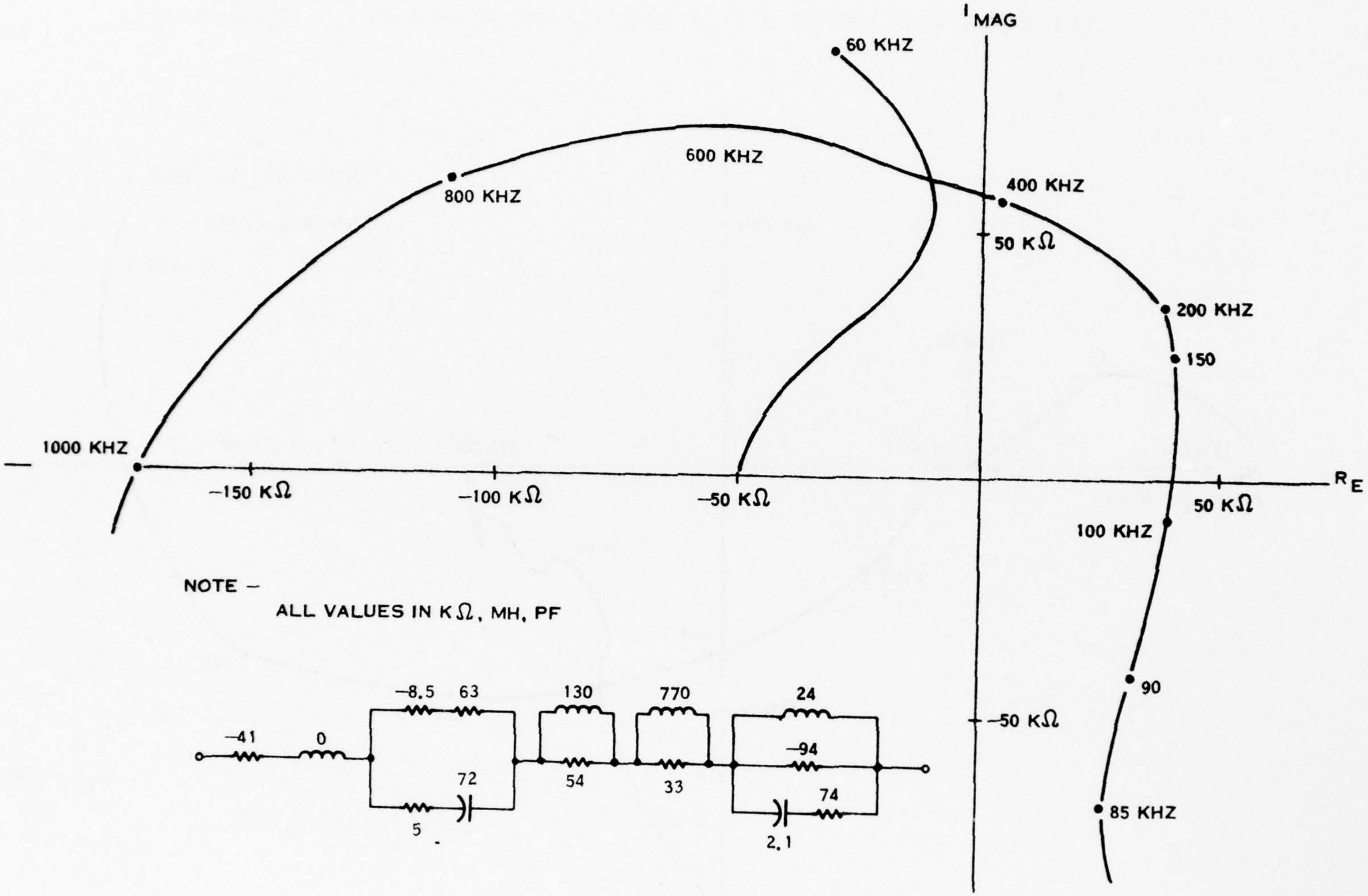

Figure 4-25 Response of RB-25-0002 at 1.8 mA with Change in Color

also be noted that the first fill is potentially more stable since there is one less intersection of the negative real axis (the significance of the negative real axis crossing is discussed in following paragraphs). The data plotted in Figure 4-26 is a second response curve of the fill plotted in Figure 4-23 except that the DC bias current was increased to 3.0 mA. As can be seen the direction of the cathode spiral and hence the stability of the plasma changes as a function of either fill color or DC current.

To investigate the stability requirements of the plasma, the stability of the circuit of Figure 4-23 was determined as a function of ballast resistance. More generally, the stabilizing network can be any complex impedance, Z_B, expressed as the ratio of two polynomials in S, A(S)/B(S). Likewise the plasma impedance, Z_P, can be expressed in the form C(S)/D(S). Writing a mesh equation for the circuit (Figure 4-27a).

$$I(S)\ Z_B(S) + I(S)\ Z_P(S) = 0$$

$$Z_B(S) + Z_P(S) = 0$$

$$\frac{A(S)}{B(S)} + \frac{C(S)}{D(S)} = 0$$

$$\frac{A(S)\ D(S) + C(S)\ B(S)}{B(S)\ D(S)} = 0$$

$$A(S)\ D(S) + C(S)\ B(S) = 0 \text{ - C.E. - The Characteristic Equation.}$$

It should be noted that the C.E. for the generalized series network is identical to the numerator of the impedance as seen by the biasing source. The stability of the network is defined by

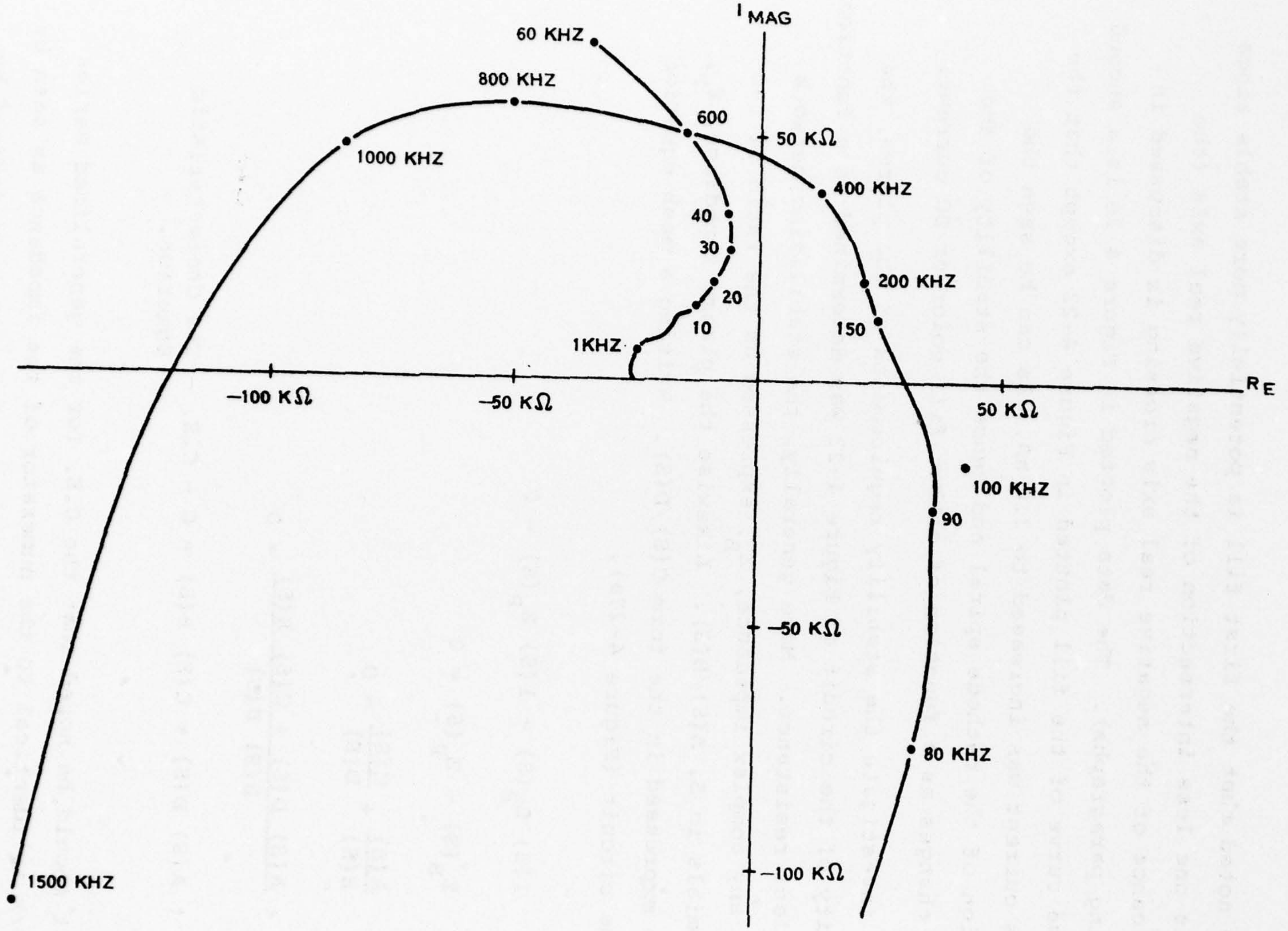

Figure 4-26 Response of RB-25-0002 at 3.0 mA DC - No Change in Fill Color

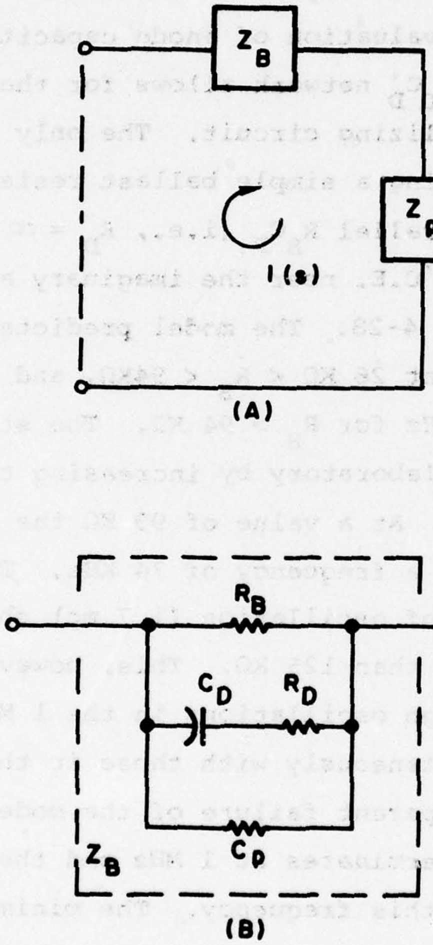

(A)

(B)

Figure 4-27 General Discharge Biasing Network the roots of this characteristic equation. That is, a stable system requires that all roots of the C.E. have negative real parts. A computer program was developed to compute the roots of the characteristic equation for the general Z_B shown in Figure 4-27b as a function of one of its elements. The addition of C_P to the network allows for the evaluation of anode capacitance on network stability. The series $R_D C_D$ network allows for the addition of a pole-zero to the stabilizing circuit. The only cases studied to date are those involving a simple ballast resistor (i.e., $R_D = \infty$, $C_P = 0$) and a parallel $R_B C_P$ (i.e., $R_D = \infty$). A root locus showing the roots of the C.E. near the imaginary axis as a function of R_B is given in Figure 4-28. The model predicts stable operation for values of R_B such that $26\ K\Omega < R_B < 94 K\Omega$, and periodic instability at a frequency of $\approx$ 74 KHz for $R_B > 94\ K\Omega$. The stability at 74 KHz was investigated in the laboratory by increasing the ballast keeping the DC current constant. At a value of 99 KΩ the discharge became unstable, oscillating at a frequency of 74 KHz. The model predicts that a second frequency of oscillation (1.7 mc) should be observed for values of R_B greater than 125 KΩ. This, however, did not seem to be the case even though oscillations in the 1 MHz frequency range have been observed simultaneously with those in the 100 KHz range in other tubes. This apparent failure of the model may be due to the fact that the data terminates at 1 MHz and therefore the model may be inaccurate above this frequency. The minimum and maximum stable ballast resistance is plotted as a function of C_P in Figure 4-29. The correlation between this plot and the real world has not been determined. However, it should be noted that the trend in $R_{B_{max}}$ with increasing C_P has been observed, that is, the upper threshold of oscillation can be increased by increasing C_P.

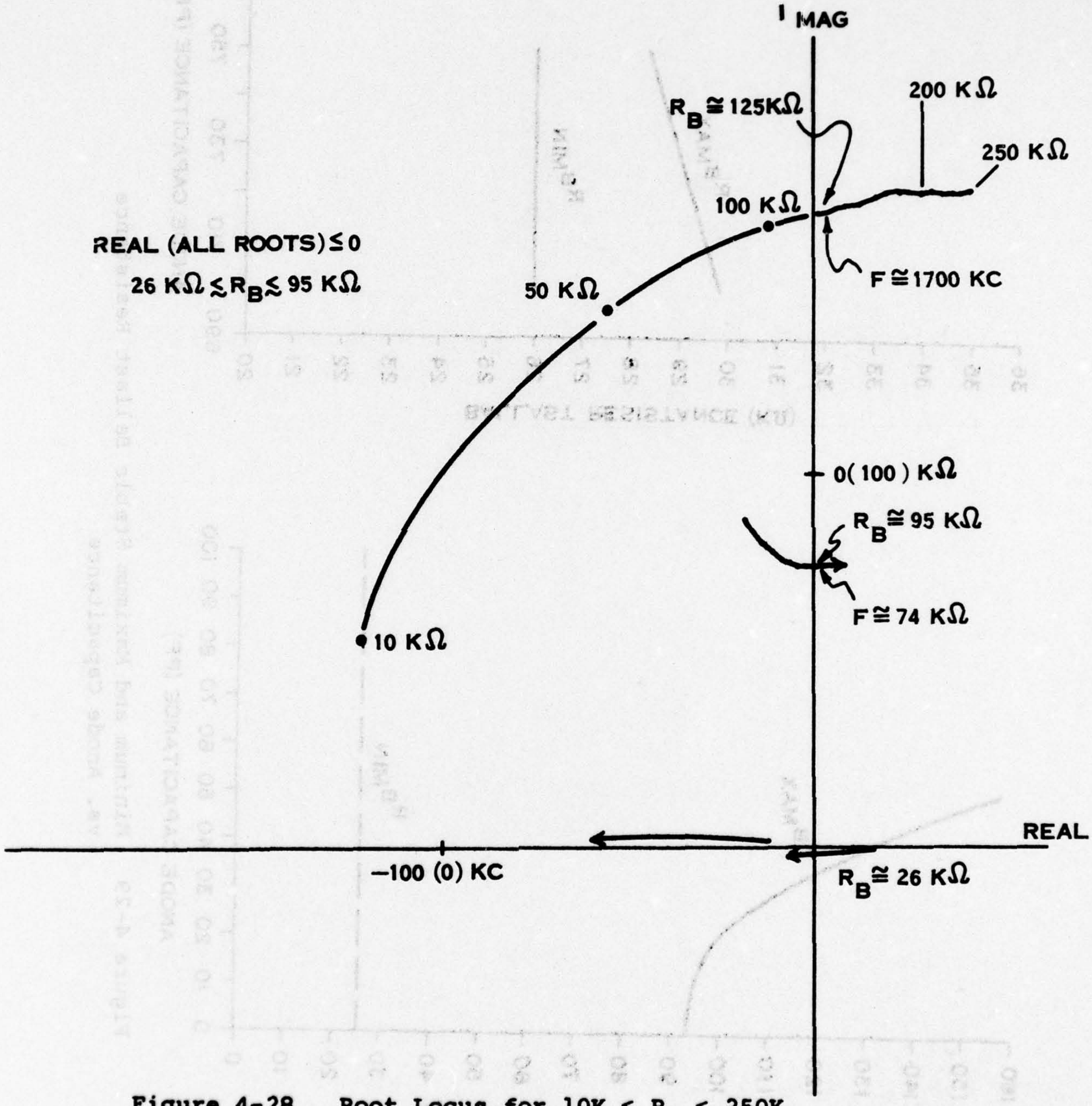

Figure 4-28 Root Locus for $10K \leq R_B \leq 250K$

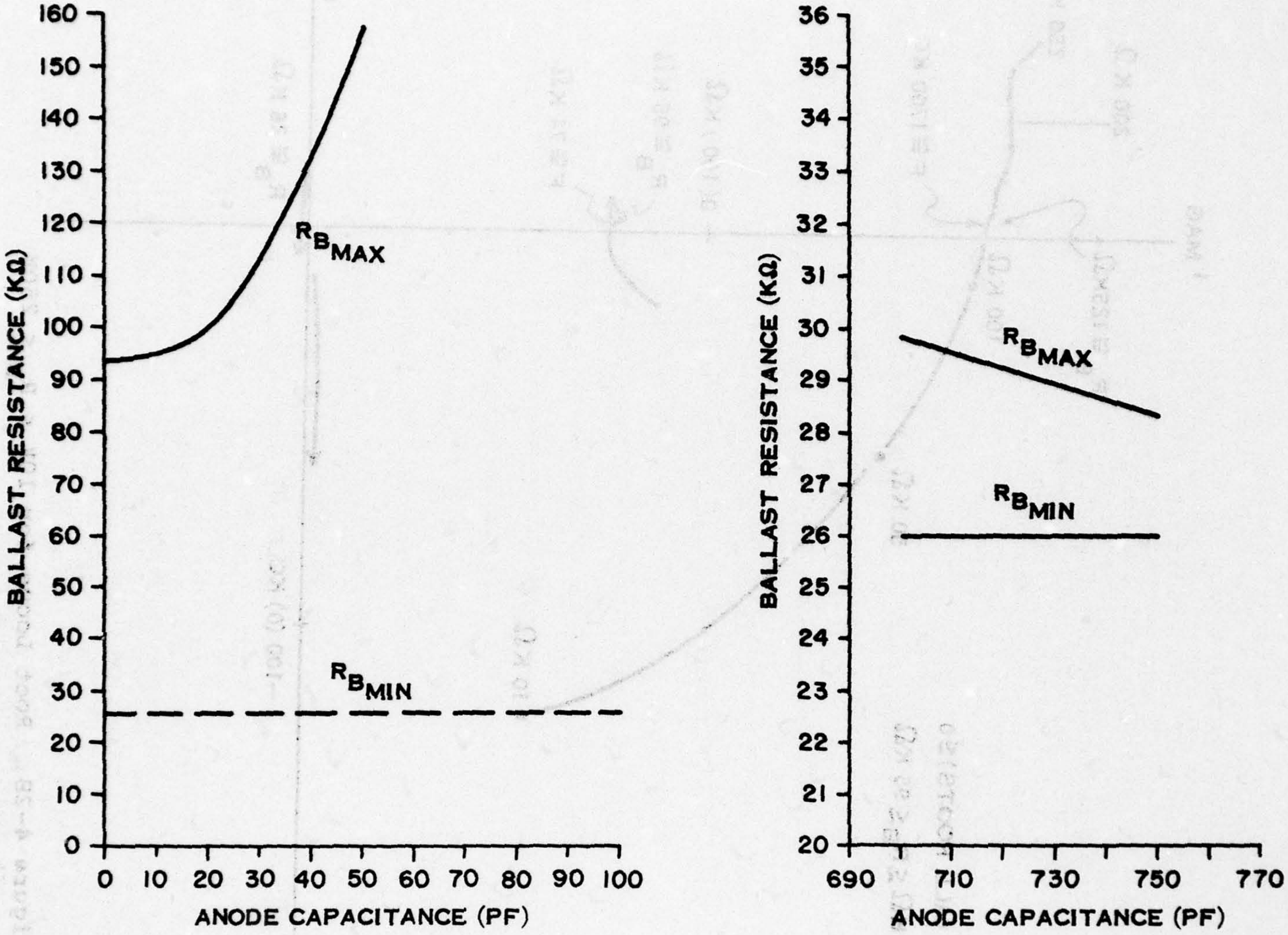

Figure 4-29 Minimum and Maximum Stable Ballast Resistance vs. Anode Capacitance

It should also be pointed out that for a stabilizing network consisting of only a resistor the range of stable resistance can be determined by inspection of the complex plane plot of discharge impedance. Instability is possible wherever the impedance intersects the negative real axis and the range of stable ballast resistance is defined by the DC intersection and the first AC intersection. Realizing this, it is fairly simple to determine relative stabilities of different fills by inspection of their frequency responses.

Also, observe that there appears to be a critical value of capacitance above which the stable range of ballast resistance begins to decrease as capacitance increases.

The amplitude of the AC current modulation applied to the plasma to generate the frequency response information varied from 5 μa to 50 μa. The actual level used was typically the largest level that could be applied without distortion. Over driving would result in obvious non-linearities in the plasma response along with generation of the second harmonic of the input frequency. The non-linearity was most severe near the 180° phase shift frequency and quite small input signal levels were required at and near this frequency to maintain a linear response. No attempt has been made to account for this non-linearity in the equivalent circuit.

The propensity of the RB-25 laser gyro block for discharge oscillations in the frequency range around 100 KHz prompted additional laboratory investigations into possible methods for eliminating the problem concurrent with the modeling effort. Initially, a silicon photodiode was used to examine the glow of the discharge to determine how the amplitude of the oscillations changed with distance from the anode. The amplitude was found to increase with increasing distance from the anode and appeared to reach a maximum at the region of negative glow in the cathode.

While optically monitoring the cathode region, the AC impedance at the anode was decreased by adding capacitance from this point to the cathode to determine if the oscillations could be affected at the accessible tube terminals. The amplitude of the oscillation was found to decrease with decreasing impedance and could actually be eliminated if the impedance was made small enough. It was also demonstrated that by replacing the signal generator in the AC test circuit of Figure 4-3 with a non-inverting amplifier having suitable gain whose input is the voltage across the series cathode sense resistor (i.e., by applying electrical feedback) the oscillation could be quenched.

It has also been observed that the tendency to instability appears to be a function of fill quality where fill color was used as a qualitative indication of fill quality. The cleaner the fill, the more stable the discharge.

4.2.5 LIFE TEST PROGRAM

4.2.5.1 Introduction

A life test program has been undertaken in order to define the correlation between the discharge electrical parameters and laser life, to investigate the feasibility of using the electrical parameters as a means of evaluating fill quality and predicting service life, and to investigate the relationship between gas volume and life. New test vehicles were designed capabile of operating as single fundamental mode linear lasers with PZT tuhable cavities. The fabrication and processing techniques employed are identical to those used in the fabrication of the RB-25 laser gyro. A life test station has been designed which can accommodate six of these linear lasers. The test station electronics provides for active cathode current control, and monitoring of tube current and voltage by means of a panel mounted digital meter and running time with digital elapsed time indicators.

The test vehicles can be removed from the test station for periodic measurement of optical output power, lasing threshold, plasma frequency response, and static V-I characteristics.

4.2.5.2 Life Test Vehicle Design

Single mode linear lasers were designed to be used as test vehicles for the life test program. PZT tuning is provided to enable positioning of the single fundamental mode at line center during measurements of optical output power. The cavity is a half-symmetric resonator, 12.1 cm in length. A gain of 8.6 cm is provided with a bore diameter of 1.25 nm in a split discharge configuration. Solder seals are used to fasten electrodes to the unit, whereas optical contacts provide the seals for mirrors. The materials, fabrication, and assembly processes are identical to those used in the manufacture of the RB-25 Laser Gyro. The gas volume has been calculated to match that of the gyro. Larger volumes can be accommodated by simply changing the depth of one counterbore during block fabrication. Removal from the fill stand is accomplished utilizing the current pinch-off design. An additional anode is provided midway between the running anodes to allow investigation of the electrical characteristics of the cathode region. Table 4-1 details the life test vehicle specifications while Figure 4-30 provides a sketch of the unit.

4.2.5.3 Life Test Station Design

A life test station has been designed and fabricated to allow burn-in of the life test vehicles under active current control. Solid state series pass regulators provide this current control to an accuracy of ±1.5% with a dynamic range of 280 volts. The station has the capacity to handle six dual anode test vehicles.

TABLE 4-1
LIFE TEST VEHICLE SPECIFICATION

CAVITY:

GEOMETRY - LINEAR
LENGTH - 12.1 cm
TUNING - PZT TUNABLE OVER 1 λ
RESONATOR - HALF SYMMETRIC, R = 100 cm
BORE - 1.25 mm DIAMETER x 8.6 cm LONG,
SPLIT DISCHARGE

OUTPUT:

MODE - TEM_{oo}
BEAM RADIUS - 0.25 mm
POWER - 10 - 100 μw AT 3.0 ma CATHODE CURRENT
DEPENDENT ON MIRROR TRANSMISSION

ELECTRODES:

CATHODE - ALUMINUM 2024
(0.15 ma/cm^2 @ 3.0 ma)
ANODE - NICKEL WIRE BRAZED TO INVAR BASE

SEALS:

MIRRORS - OPTICAL CONTACT
ELECTRODES AND PUMP-OUT - SOLDER (TIN, TIN-LEAD)
PINCH-OFF - COPPER

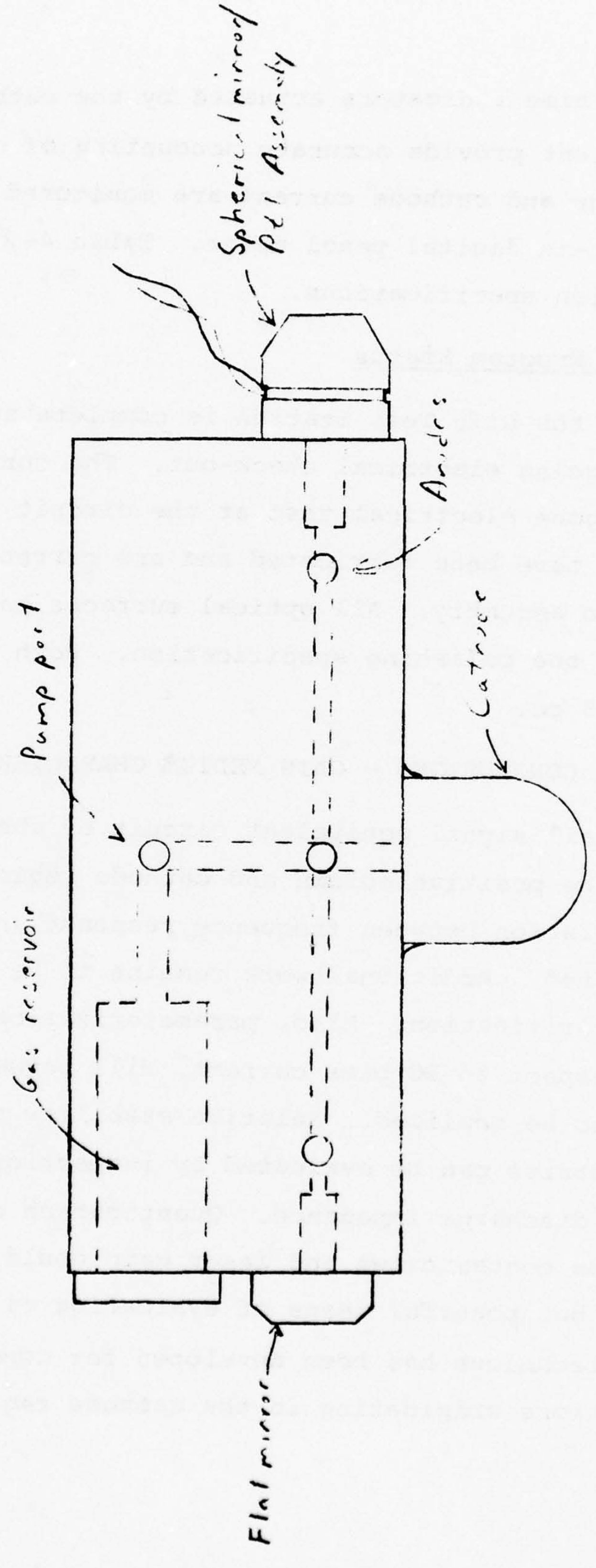

Figure 4-30 Linear Laser Life Test Vehicle

Individual elapsed time indicators actuated by the cathode current of the unit under test provide accurate accounting of operating life. Anode voltage and cathode current are monitored on station by means of a built-in digital panel meter. Table 4-2 details the life test station specifications.

4.2.5.4 Life Test Program Status

Fabrication of the Life Test Station is complete and this unit is currently undergoing electrical check-out. The current regulators have already undergone electrical test at the circuit level. The life test vehicles have been fabricated and are currently undergoing processing prior to assembly. All optical surfaces have been inspected and meet the polishing specification. Both these units have a volume of 15 cc.

4.2.6 SUMMARY AND CONCLUSIONS - GAIN MEDIUM CHARACTERIZATION

A tentative small signal equivalent circuit of the gain medium partitioned into the positive column and cathode region has been realized. A correlation between frequency response and fill quality has been demonstrated. Additional work remains to be done with respect to model verification. Also, parameterization of the model components with respect to DC bias current, fill parameters, and geometry has yet to be realized. Relative stability of different fills and/or geometries can be evaluated by inspection of the complex plane plot of the discharge impedance. Quantization of the relationship between plasma contaminates and laser gain could provide a relatively simple but powerful means of evaluating fill quality and life. An active technique has been developed for controlling discharge oscillations originating in the cathode region.

TABLE 4-2

LIFE TEST STATION - SPECIFICATION

CAPACITY:	6 SINGLE ANODE TEST VEHICLES OR 3 DUAL ANODE TEST VEHICLES
CURRENT CONTROL:	ACTIVE, SOLID STATE SERIES PASS REGULATOR CURRENT ADJUSTABLE - 1.5 ma TO 10.0 ma DYNAMIC RANGE - 280 VOLTS ACCURACY: ±1.5% WITH TEMPERATURE AND LOAD VARIATIONS
TIME INDICATION:	INDIVIDUAL ELAPSED TIME INDICATORS; ANODE CURRENT ACTUATED
METERING:	TEST VEHICLE ANODE VOLTAGE AND CATHODE CURRENT MONITORED WITH 3-1/2 DIGIT DPM; ±0.05% ±1 COUNT ACCURACY

As a result of the experimental data acquired to date along with analysis of the small signal equivalent circuit presented earlier in this report some general stability guidelines to be considered in the design of a discharge tube can be defined.

Two regions of instability have been encountered: Instabilities at low current levels characterized by either aperiodic behavior (discharge extinction) or periodic oscillations, the amplitude of which decreases with increasing current; and oscillations at higher current levels, the amplitude of which increases with increasing current. Stability of the discharge at low current levels is controlled primarily by the low frequency components of the model, presented earlier. This low frequency equivalent circuit is given in Figure 4-31 including a ballast resistance, R_B, and the parasitic capacitance between anode and cathode C_S. The inductance is primarily associated with the cathode region while the significant portion of the negative resistance is provided by the positive column. A stability analysis of this circuit results in limits on the value of ballast resistance required to provide a stable discharge, that is:

$$|R_N| < R_B < R_{B_{max}}$$

As C_S increases the value of $R_{B_{max}}$ decreases. This truncated model predicts that for $C_S = 700$ pf, for instance,

$$R_{B_{max}} = 30.4K$$

with a frequency of oscillation equal to

$$f_{osc} = 6.9 \text{ KHz}$$

(The complete model predicts 29.8 K and 7.2 KHz respectively.) In other words for $R_B < 25.8$ K it will be impossible to maintain a discharge (aperiodic instability) and for $R_B \geq 30.4$ K low frequency oscillations will be observed. For a fixed cathode geometry and therefore a nearly fixed L one can maximize the stability of a low current discharge by minimizing C_S and R_N. A list of guidelines for improving the stability of a discharge to be biased at low current levels would include:

1. Minimize R_N by minimizing the length of the positive column.
2. Minimize capacitance from anode and positive column to cathode
3. Fill to higher pressures
4. Fill to lower ratios, He:Ne

Instabilities that occur at the higher current levels (amplitude of oscillation increases with increasing current) are due primarily to the cathode impedance and can be controlled by:

1. Maximizing fill purity
2. Minimizing the impedance of the stability network, i.e., increasing C_S and decreasing R_B
3. Filling to lower pressures
4. Filling to higher He:Ne ratios

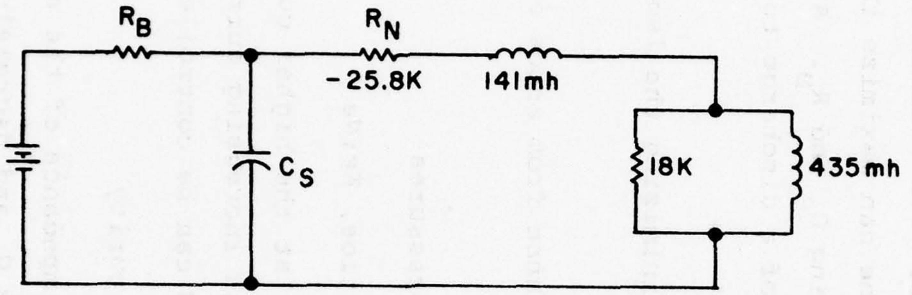

Figure 4-31 Low Frequency Equivalent Circuit

4.3 RING LASER POWER PARAMETRIZATION

The output power of a ring laser gyroscope depends on the parameters of the excited medium (small-signal gain, saturation parameter, importance of cross-relaxation, etc.) as well as those of the optical resonator (transmission of the output mirror, other losses, and cavity length or mode splitting). The behavior of the gain medium in a helium-neon laser has been the subject of numerous studies, but perhaps the best treatment is that of P. W. Smith (Refs. 4-1 through 4-3). Other workers such as Field (Ref. 4-4) and Bennett (Ref. 4-5) have, of course, made contributions. Briefly one may summarize the results by saying that in the operating He-Ne laser the small-signal gain curve is distorted by the burning of holes at the frequencies of the lasing modes, the hole-width depending on the gas pressure but lying in the range of 50 to 200 MHz at the pressures of interest. Also, the gain over the entire curve is reduced by cross-relaxation effects, mediated principally by radiation trapping; this effect is similar to the universal gain reduction which occurs in a homogeneously broadened gain medium (e.g., most CO_2 lasers). Smith (Ref. 4-2) has shown that the saturated gain of a He-Ne laser may be described by

$$g = \frac{g_o}{\left(1 + \frac{I}{w_o}\right)^{\frac{1}{2}} + C\frac{I}{w_o}}$$

for a travelling-wave amplifier operating at line center. Here g is the saturated gain, g_o is the small-signal gain, I is the intensity, w_o is the saturation parameter, and C is the cross-relaxation parameter. For a travelling-wave (ring) laser running on n modes (total of clockwise and counterclockwise), we would have

$$g = \frac{g_o}{\left(1 + \frac{I}{w_o}\right)^{\frac{1}{2}} + nC\frac{I}{w_o}} \qquad (1)$$

assuming equal intensities for the n modes and non-overlapping holes. The condition for operation of a laser is, for each mode,

$$g = \ell + t \quad \text{or} \quad \frac{g}{\ell} = 1 + \frac{t}{\ell} \qquad (2)$$

$$I_{out} = tI \qquad (3)$$

where t is the output mirror power transmission, ℓ is the sum of all other cavity losses, and I_{out} is the output intensity.

The parameters in Eq. (1) are taken from Smith (Refs. 4-2 and 4-3) as follows:

$$w_o = (12.9\ \text{Torr}^{-1}\ P - 6.5)\ \text{w/cm}^2 \qquad (4)$$

$$C = 6.5 \times 10^{-3}\ w_o\ \text{cm}^2/\text{w} \qquad (5)$$

$$g_o = 3 \times 10^{-4}\ L/D \qquad (6)$$

where L and D are the tube length and diameter respectively. For a given pressure P the optimum diameter is given by $D_{opt}P$ = 3.6 Torr-mm. Using these values and taking L - 15 cm, ℓ = 1 percent, we show in Figure 4-32 the output intensity (per mode) as a function of output mirror transmission for pressures from 1 to 4 Torr and optimum diameter. These curves are purely indicative since in fact the small-signal gain will be reduced somewhat (~30 percent) from the values in Eq. (6) due to the necessity of operation either off line center or with two neon isotopes to avoid

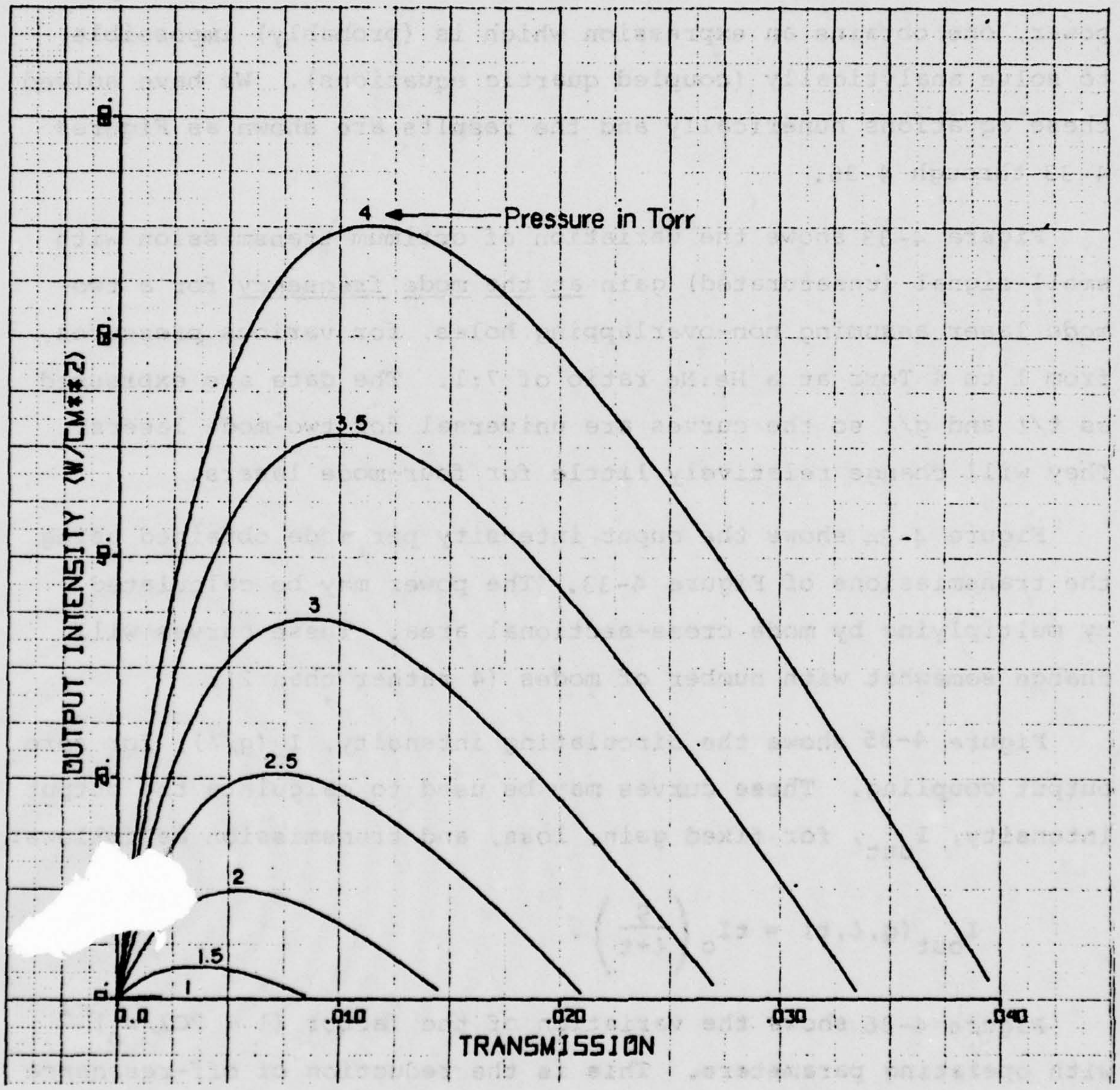

Figure 4-32 Output Intensity vs. Mirror Transmission for a Two-Mode He-Ne Laser 15 cm Long

mode competition effects.

If one optimizes the mirror transmission for maximum output power, one obtains an expression which is (probably) impossible to solve analytically (coupled quartic equations). We have solved these equations nunerically and the results are shown as Figures 4-33 through 4-36.

Figure 4-33 shows the variation of optimum transmission with small-signal (unsaturated) gain <u>at the mode frequency</u> for a two-mode laser assuming non-overlapping holes, for various pressures from 1 to 4 Torr at a He:Ne ratio of 7:1. The data are expressed as t/ℓ and g/ℓ so the curves are universal for two-mode lasers. They will change relatively little for four-mode lasers.

Figure 4-34 shows the ouput intensity per mode obtained using the transmissions of Figure 4-33. The power may be calculated by multiplying by mode cross-sectional area. These curves will change somewhat with number of modes (4 rather than 2).

Figure 4-35 shows the circulating intensity, $I_c(g/\ell)$, for zero output coupling. These curves may be used to calculate the output intensity, I_{out}, for fixed gain, loss, and transmission as follows:

$$I_{out}(g,\ell,t) = tI_c\left(\frac{g}{\ell+t}\right).$$

Figure 4-36 shows the variation of the factor $(1 + 2CI/w_o)^{-1}$ with operating parameters. This is the reduction of off-resonance gain due to the presence of laser action, corresponding to Figure 4-35 (i.e., assuming t=0). This factor enters into considerations of whether the laser will oscillate in other, undesirable modes

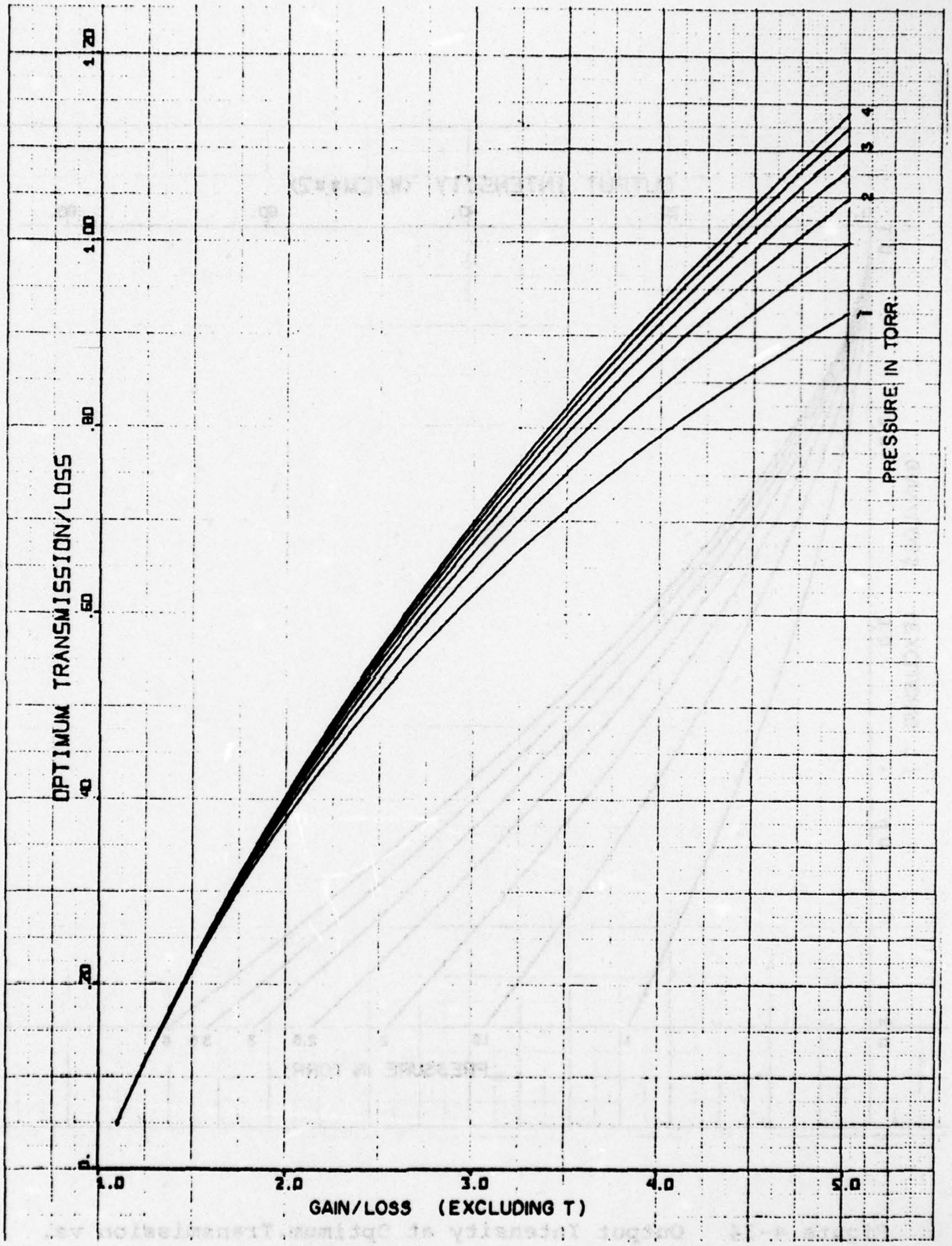

Figure 4-33 Scaled Optimum Output-Mirror Transmission vs. Scaled Gain for a Two-Mode He-Ne Laser

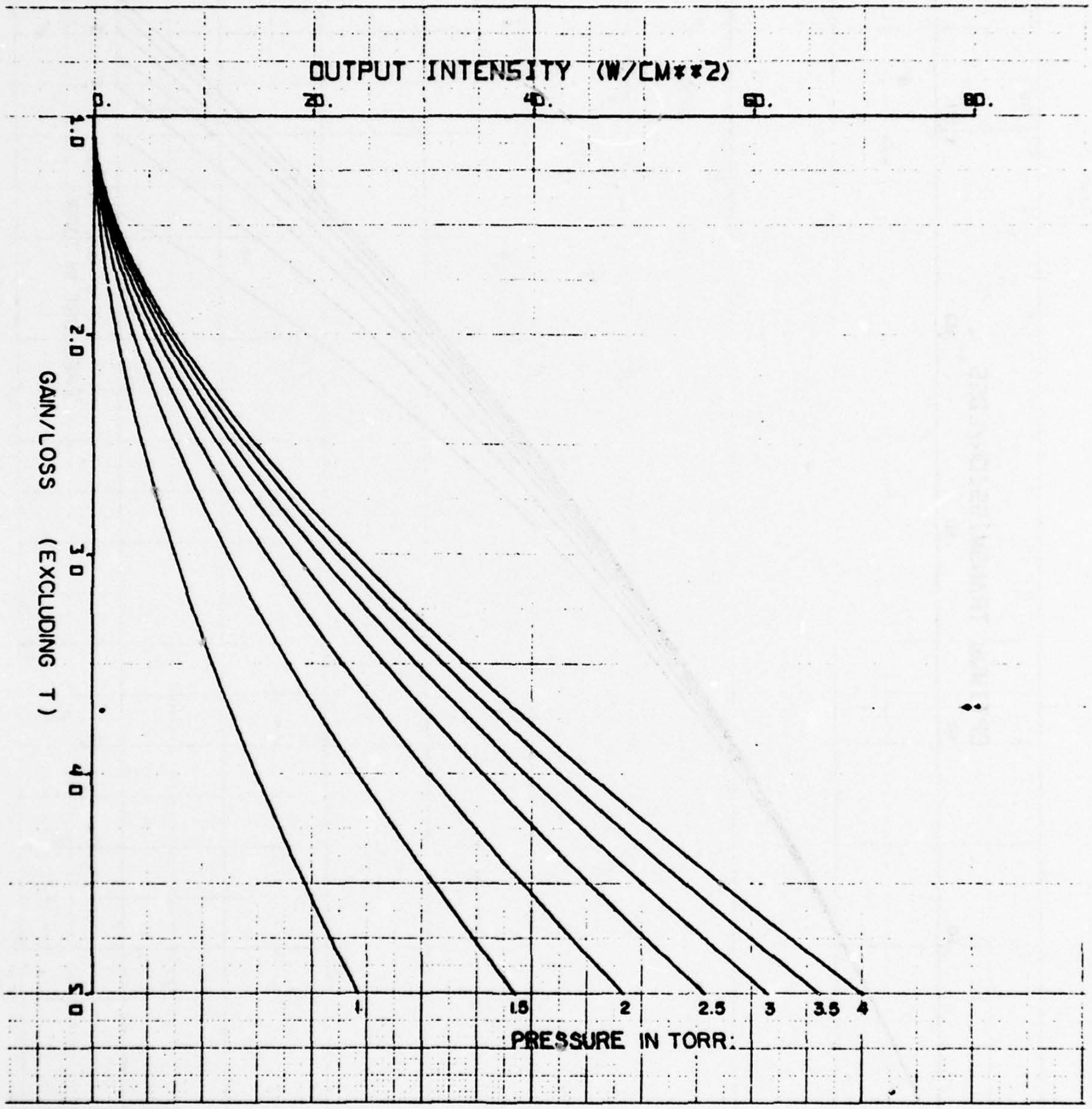

Figure 4-34 Output Intensity at Optimum Transmission vs. Scaled Gain for a Two-Mode He-Ne Laser

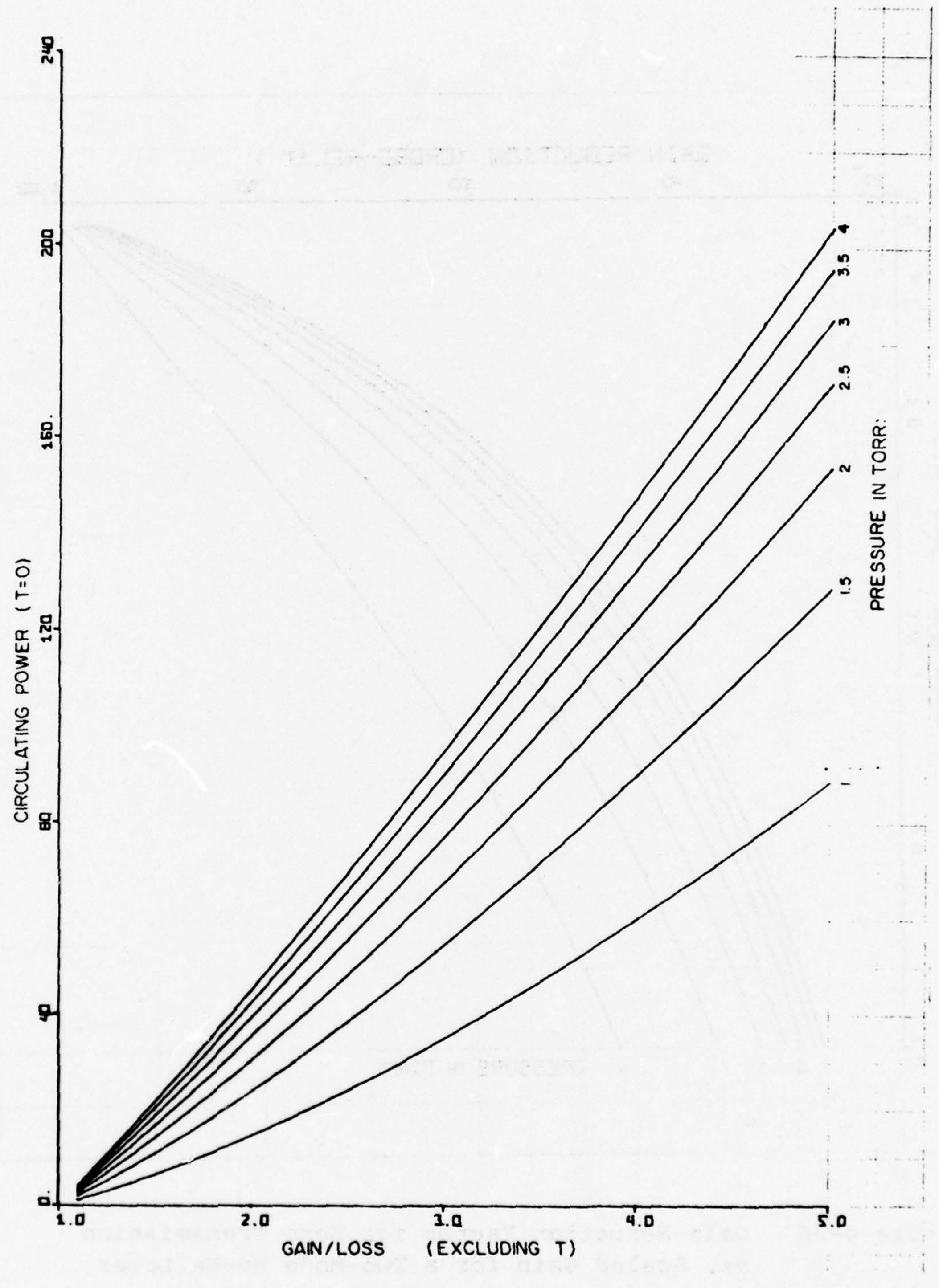

Figure 4-35 Circulating Intensity for Zero Transmission vs. Scaled Gain for a Two-Mode He-Ne Laser

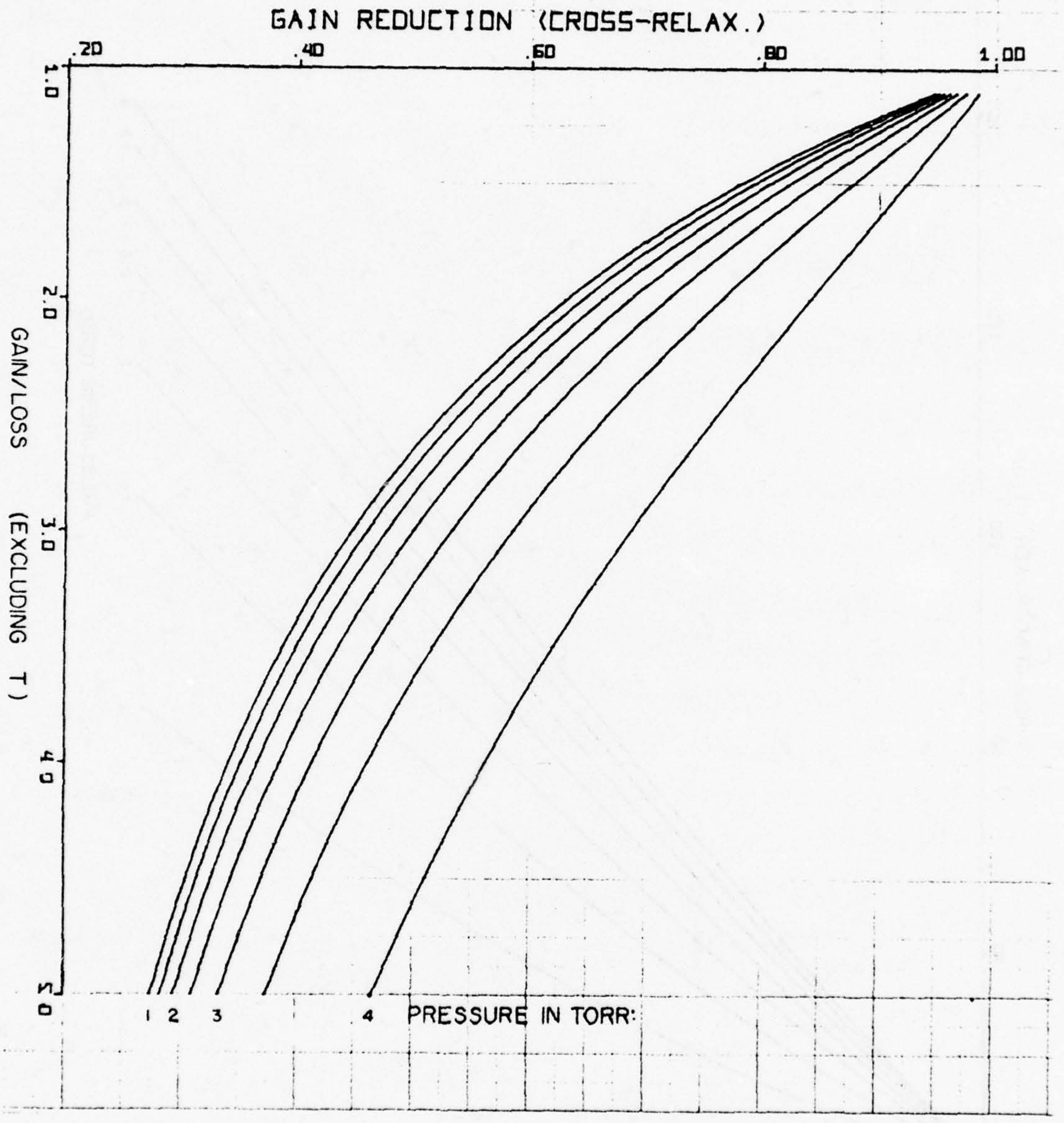

Figure 4-36 Gain-Reduction Factor for Zero Transmission vs. Scaled Gain for a Two-Mode He-Ne Laser

since their gain, while possible nominally above threshold will be somewhat quenched by cross-relaxation. In other words, the small-signal gain for a non-lasing mode is given by $g = g_o(1 + nCI/w_o)^{-1}$ where I is the intensity in each of the n(=2) lasing modes (assuming the non-lasing mode runs in a direction and at a frequency where there is no hole due to the lasing modes), and g_o is the small-signal gain which would otherwise be present at that frequency.

Figures 4-37 through 4-41 show the same quantities given in Figures 4-32 through 4-36 but for the case of a four-mode ring laser.

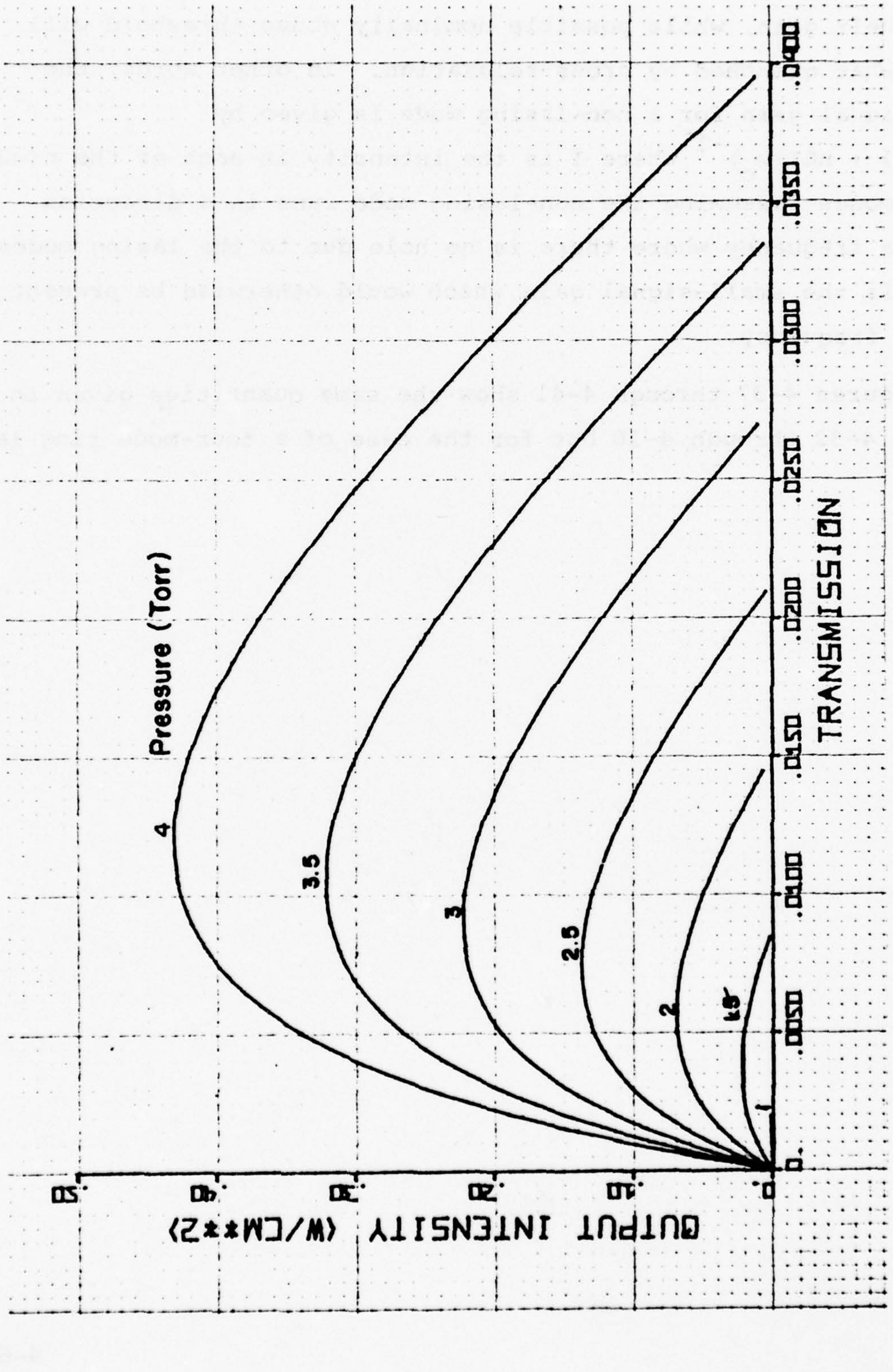

Figure 4-37 Output Intensity vs. Mirror Transmission for a Four-Mode He-Ne Laser 15 cm Long

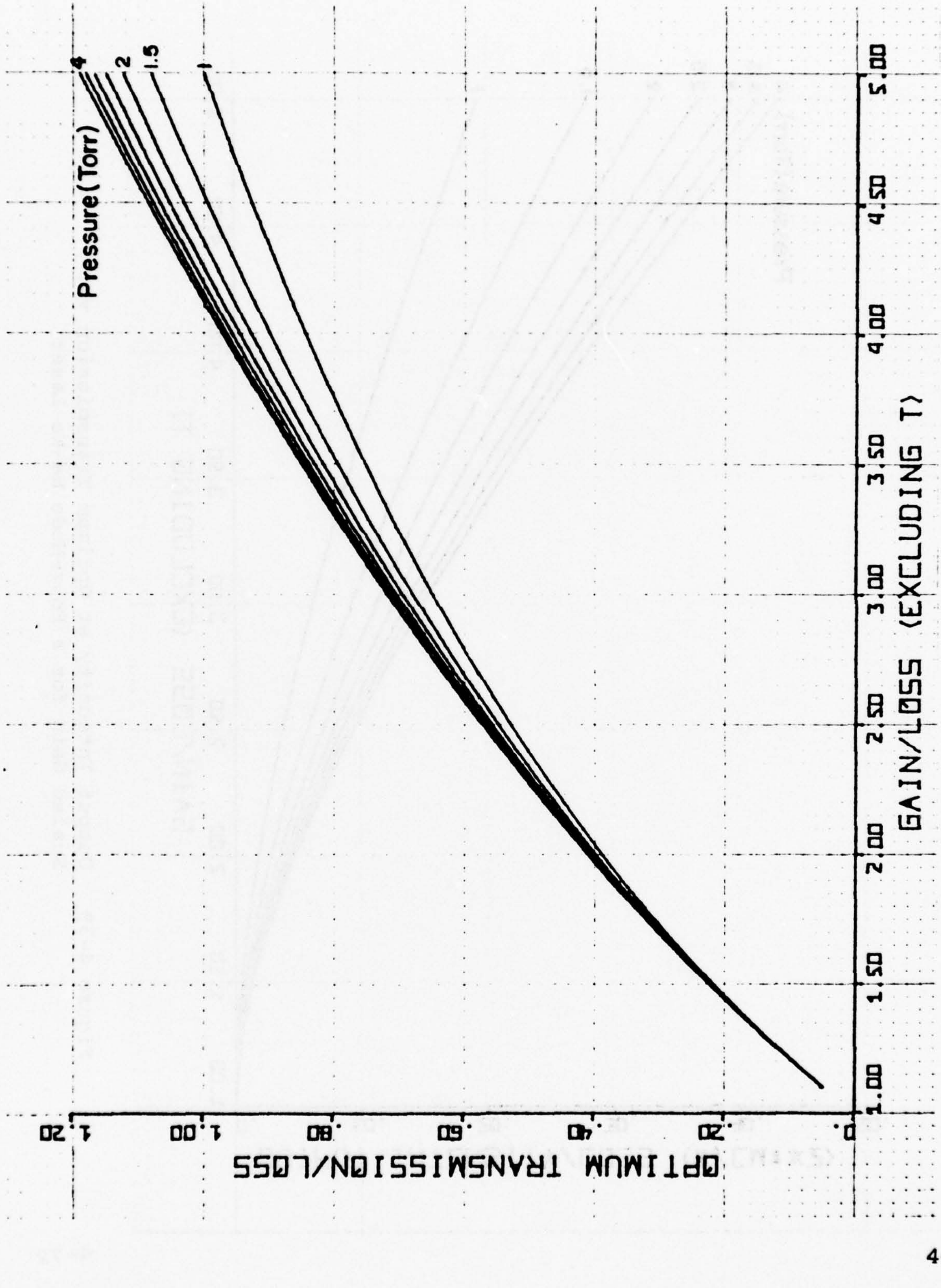

Figure 4-38 Scaled Optimum Output-Mirror Transmission vs. Scaled Gain for a Four-Mode He-Ne Laser

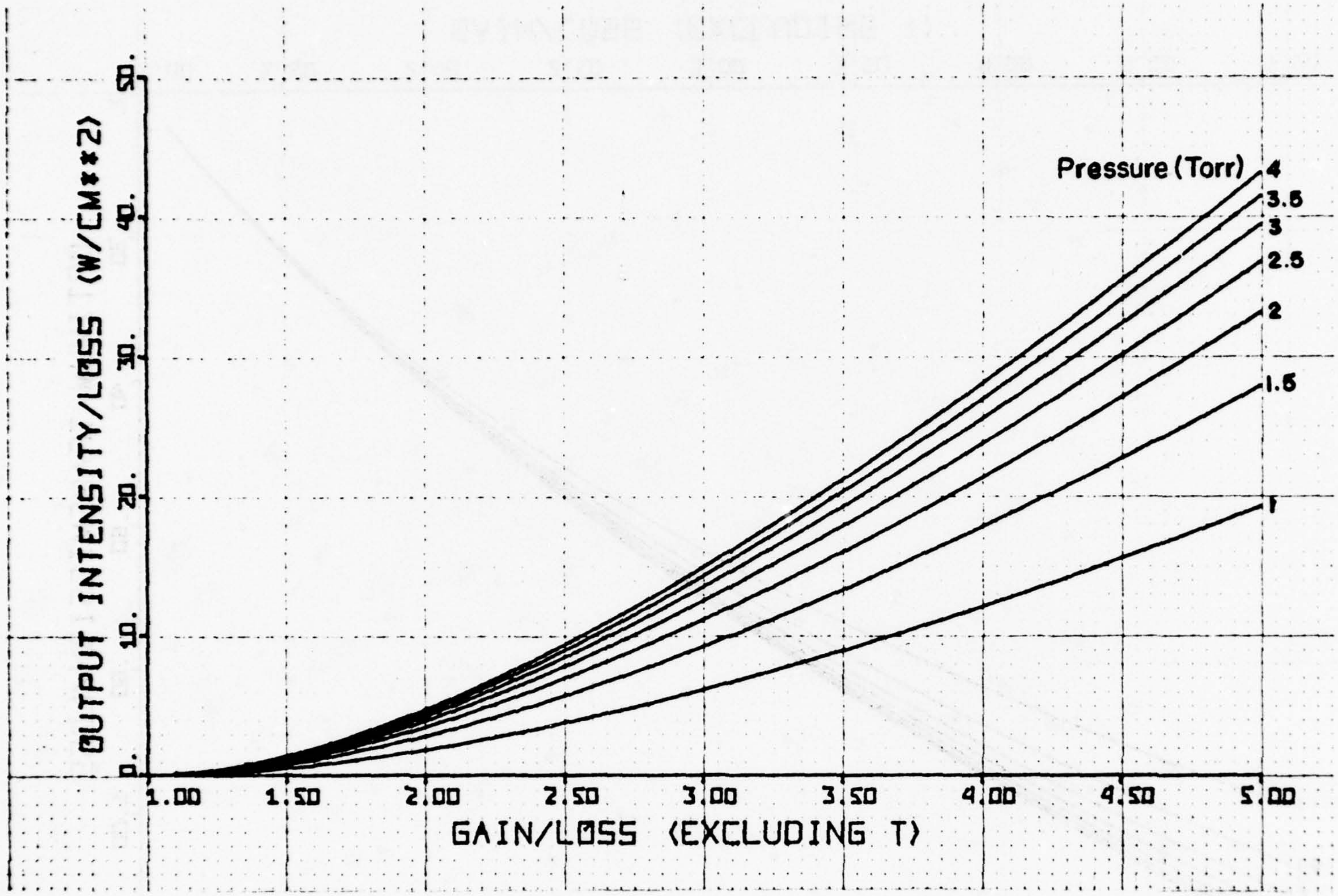

Figure 4-39 Output Intensity at Optimum Transmission vs. Scaled Gain for a Four-Mode He-Ne Laser

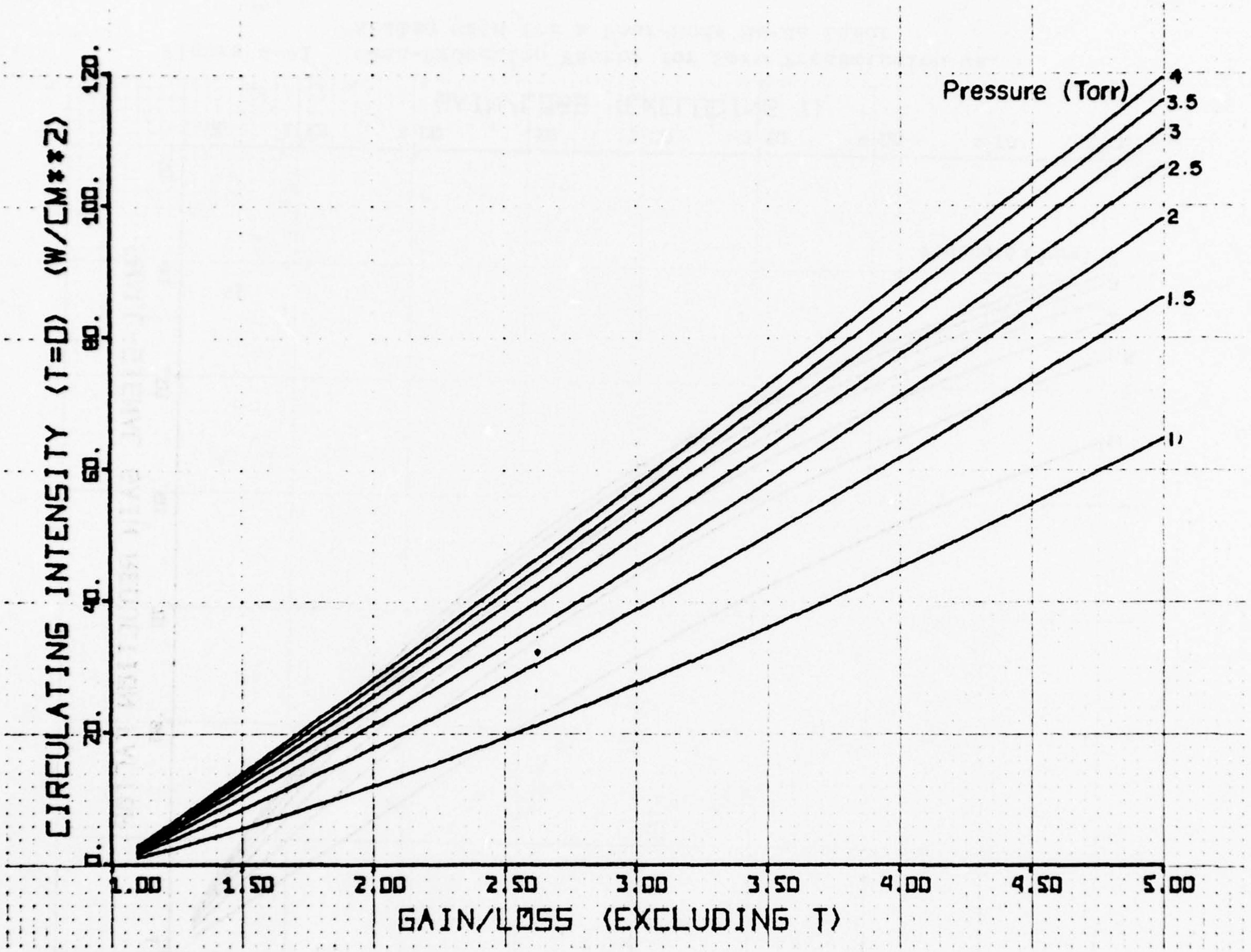

Figure 4-40 Circulating Intensity for Zero Transmission vs. Scaled Gain for a Four-Mode He-Ne Laser

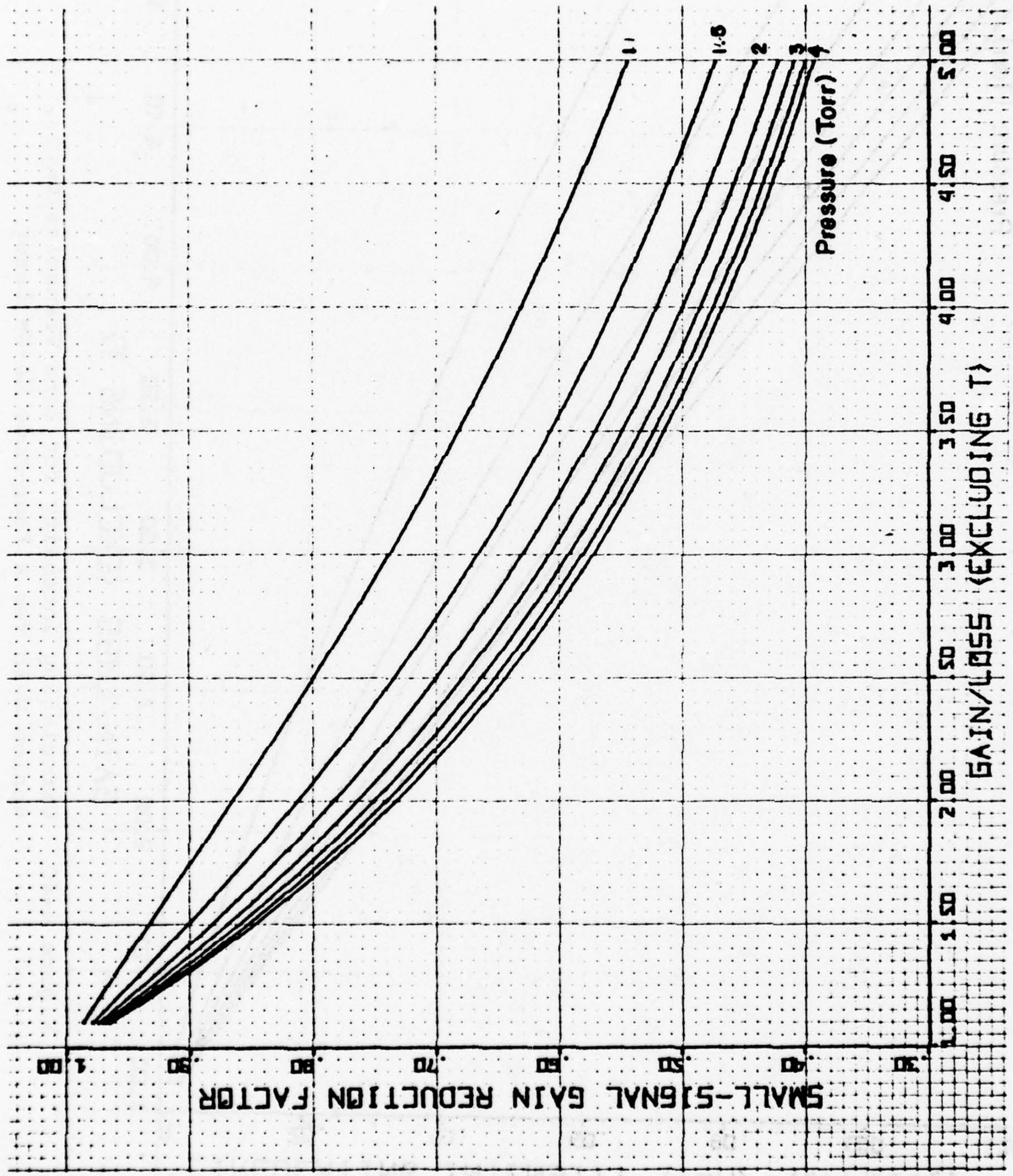

Figure 4-41 Gain-Reduction Factor for Zero Transmission vs. Scaled Gain for a Four-Mode He-Ne Laser

SECTION 5

DESIGN CONSIDERATIONS

5.1 GEOMETRIC STABILITY/DRAG INTERACTION

The full potential of the He-Ne ring laser gyroscope (RLG) can be realized only if a number of perturbing influences can be minimized or eliminated. Perhaps the most important among these is one which affects two- and four-frequency gyros equally, namely, Langmuir flow-induced Fizeau-Fresnel drag. Langmuir (Ref. 5-1) has shown that the passage of an electric current through a plasma confined to a narrow tube results in a mass flow within the tube. The mechanism underlying this effect is the difference in average momentum transfer experienced by electrons and ions in collisions with the walls. The electric field which causes the passage of current exerts equal and opposite forces upon the (equally abundant) positive (ionic) and negative (electronic and some ionic) species present. However, the ions transfer a greater fraction of their momentum to the wall in collisions since the mass mismatch with the atoms making up the wall is less for them. Thus, crudely speaking, the ions are more strongly coupled to the wall than are the electrons and thus (in that portion of the gas within one mean free path of the wall) the average force upon the gas near the walls is in the direction of that due to the electrons, i.e., away from the cathode K. If the tube is sealed off, or for some other reason the net mass flow is constrained to be zero, there will be then a flow from A to K near the center of the tube.

When light passes through a dielectric of index of refraction n moving with velocity v, it can be shown that the speed of the light (phase velocity) in a fixed reference frame is changed from its normal value c/n by an amount (Ref. 5-2).

$$\Delta c = v\left(1 - \frac{1}{n^2} + \frac{\omega}{n}\frac{dn}{d\omega}\right) \qquad (5\text{-}1)$$

where ω is the radian frequency of the light. The first two terms in parentheses come simply from the relativistic formulae for addition of velocities; the last term is due to the Doppler shift of the light as seen by the dielectric. In the vicinity of a resonance (e.g., in a laser) this term dominates the others and, to give a concrete example, the output bias of a laser gyroscope can change by hundreds of Hz for a 1 mA change in current. For this reason practical gyros employ a split discharge in which the current flows in opposite directions in the two legs of the discharge.

One can calculate the flow profile within the laser tube if one assumes some distribution of force within the discharge due to the Langmuir effect. One must also include the effect of viscosity at the tube walls. The resulting equation is

$$F(r) = -\eta\left(v'' + \frac{v'}{r}\right) \qquad (5\text{-}2)$$

where v is the flow velocity, η is the viscosity, primes denote differentiation with respect to the radial coordinate r, and F(r) is the force per unit volume. We have assumed $F(r) = F_o(a^2 - r^2) + F_1$ where a is the bore radius. The assumed radial dependence was chosen partially for convenience, although it is a reasonable representation of the real forces in a narrow-bore tube. With this assumption the radial flow dependence is

$$\frac{v(r)}{v_o} = f(r) = 3\left(\frac{r}{a}\right)^4 - 4\left(\frac{r}{a}\right) + 1 \qquad (5\text{-}3)$$

where v_o is the flow speed at the center (r = 0), and we have chosen F_1 (a back-pressure term) to give zero net flow along the bore since presumably the two legs have equal current, pressure and flow.

The effective flow velocity for the laser mode is obtained by averaging over the mode volume. We have simplified this problem by treating the mode as if it were infinitely thin, i.e., by writing the position of the optic axis of the laser in the discharge path as

$$\vec{r}(z) = \vec{r}_o + z\vec{\Delta}_o \; . \tag{5-4}$$

(z is the coordinate running along the bore) and assuming the average flow is that obtained by averaging Eq. (5-3) along the optic axis:

$$\bar{v} = \frac{1}{L}\int v\left(r(z)\right)dz \; .$$

We assume a split discharge with equal currents in the two (collinear) legs so that in fact we write

$$\bar{v} = \frac{2}{L}\left| v_o \int_o^{L/2} + [-v_o] \int_{L/2}^{L} \right| f\left(|\vec{r}_o + z\vec{\Delta}_o|\right)dz \; .$$

Taking the position of the mode at 0 and L as $(x_o, 0)$ and (x_2, y_2) we have

$$\vec{\Delta}_o = \left(\vec{r}(L) - \vec{r}(0)\right)/L = \left(\frac{x_2 - x_1}{L}, \frac{y_2}{L}\right).$$

Since the value of v_o depends on the viscosity and on the Langmuir-flow process for which quantitative data are difficult to obtain, we instead normalize our results for

$$\frac{\vec{v}}{|v_o|} \propto \text{frequency shift of gyro}$$

by using the experimentally observed dependence of gyro bias upon discharge current: If we extinguish one leg of the discharge we obtain several hundred Hz of bias, the exact amount varying from one gyro to another as a function of cavity length, pressure, etc. (One can show both experimentally and theoretically that the flow effect dominates the direct dispersion effects due to the altered gain of the laser.) For a bias due to one leg only of 600 Hz, the calculated shifts are given in Table 5-1 for various positions of the mode on entrance and exit, expressed in units of the bore radius. Note that by symmetry there should be no shift for $x_1^2 + y_1^2 = x_2^2 + y_2^2$, in agreement with the table. (The values of 10^{-15} to 10^{-9} are due to roundoff errors in the computer.) The Wang BASIC computer program is shown in Figure 5-1. We see that in all cases the worst errors for a given maximum deviation occur for mode positions centered at one end ($x_2 = y_2 = 0$), and that for a 1 mm radius bore, one must hold the mode to within 3 μm of center for a ±0.01 Hz error tolerance.

The significance of these calculations lies in the possibility of RLG block "warpage" due to thermal gradients, or of imperfect parallelism in the motion of the piezo-electric mirror responsible for cavity pathlength control (PLC). Crudely speaking, if the cavity contains a single spherical mirror of radius of curvature R, or several mirrors of radii R_i which act like a single mirror of radius $R = (\Sigma R_i^{-1})^{-1}$, then an angular displacement by θ of any cavity mirror results in a shift of mode position by about Rθ. Depending on the direction of tilt this motion may or may not be a pure translation, but a worst-case analysis asks the question, "What

TABLE 5-1

Gyro Bias Shift Induced by Fizeau-Fresnel Drag for Various Mode Positions

```
******************** X1=0.001, Y1=0.000 *************************
 X2 \Y2>    0.00000    0.00025    0.00050    0.00075    0.00100
-0.00100 -1.800E-15  7.499E-05  2.999E-04  6.749E-04  1.199E-03
-0.00075 -5.249E-04 -4.499E-04 -2.249E-04  1.499E-04  6.749E-04
-0.00050 -8.999E-04 -8.249E-04 -5.999E-04 -2.249E-04  2.999E-04
-0.00025 -1.124E-03 -1.049E-03 -8.249E-04 -4.499E-04  7.499E-05
 0.00000 -1.199E-03 -1.124E-03 -8.999E-04 -5.249E-04 -1.200E-15
 0.00025 -1.124E-03 -1.049E-03 -8.249E-04 -4.499E-04  7.499E-05
 0.00050 -8.999E-04 -8.249E-04 -5.999E-04 -2.249E-04  2.999E-04
 0.00075 -5.249E-04 -4.499E-04 -2.249E-04  1.499E-04  6.749E-04
 0.00100  0.000E+00  7.499E-05  2.999E-04  6.749E-04  1.199E-03

******************** X1=0.002, Y1=0.000 *************************
 X2 \Y2>    0.00000    0.00050    0.00100    0.00150    0.00200
-0.00200 -6.000E-15  2.999E-04  1.199E-03  2.699E-03  4.799E-03
-0.00150 -2.099E-03 -1.799E-03 -8.999E-04  5.999E-04  2.699E-03
-0.00100 -3.599E-03 -3.299E-03 -2.399E-03 -8.999E-04  1.199E-03
-0.00050 -4.499E-03 -4.199E-03 -3.299E-03 -1.799E-03  2.999E-04
 0.00000 -4.799E-03 -4.499E-03 -3.599E-03 -2.099E-03 -1.200E-14
 0.00050 -4.499E-03 -4.199E-03 -3.299E-03 -1.799E-03  2.999E-04
 0.00100 -3.599E-03 -3.299E-03 -2.399E-03 -8.999E-04  1.199E-03
 0.00150 -2.099E-03 -1.799E-03 -8.999E-04  5.999E-04  2.699E-03
 0.00200  0.000E+00  2.999E-04  1.149E-03  2.699E-03  4.799E-03

******************** X1=0.004, Y1=0.000 *************************
 X2 \Y2>    0.00000    0.00100    0.00200    0.00300    0.00400
-0.00400  0.000E+00  1.199E-03  4.799E-03  1.079E-02  1.919E-02
-0.00300 -8.399E-03 -7.199E-03 -3.599E-03  2.399E-03  1.079E-02
-0.00200 -1.439E-02 -1.319E-02 -9.599E-03 -3.599E-03  4.799E-03
-0.00100 -1.799E-02 -1.679E-02 -1.319E-02 -7.199E-03  1.199E-03
 0.00000 -1.919E-02 -1.799E-02 -1.439E-02 -8.399E-03 -1.200E-14
 0.00100 -1.799E-02 -1.679E-02 -1.319E-02 -7.199E-03  1.199E-03
 0.00200 -1.439E-02 -1.319E-02 -9.599E-03 -3.599E-03  4.799E-03
 0.00300 -8.399E-03 -7.199E-03 -3.599E-03  2.399E-03  1.079E-02
 0.00400  0.000E+00  1.199E-03  4.799E-03  1.079E-02  1.919E-02

******************** X1=0.008, Y1=0.000 *************************
 X2 \Y2>    0.00000    0.00200    0.00400    0.00600    0.00800
-0.00800 -1.800E-13  4.799E-03  1.919E-02  4.319E-02  7.679E-02
-0.00600 -3.359E-02 -2.879E-02 -1.439E-02  9.599E-03  4.319E-02
-0.00400 -5.759E-02 -5.279E-02 -3.839E-02 -1.439E-02  1.919E-02
-0.00200 -7.199E-02 -6.719E-02 -5.279E-02 -2.879E-02  4.799E-03
 0.00000 -7.679E-02 -7.199E-02 -5.759E-02 -3.359E-02 -1.200E-13
 0.00200 -7.199E-02 -6.719E-02 -5.279E-02 -2.879E-02  4.799E-03
 0.00400 -5.759E-02 -5.279E-02 -3.839E-02 -1.439E-02  1.919E-02
 0.00600 -3.359E-02 -2.879E-02 -1.439E-02  9.599E-03  4.319E-02
 0.00800  0.000E+00  4.799E-03  1.919E-02  4.319E-02  7.678E-02

******************** X1=0.016, Y1=0.000 *************************
 X2 \Y2>    0.00000    0.00400    0.00800    0.01200    0.01600
-0.01600 -6.000E-13  1.919E-02  7.678E-02  1.727E-01  3.070E-01
-0.01200 -1.343E-01 -1.151E-01 -5.758E-02  3.839E-02  1.727E-01
-0.00800 -2.303E-01 -2.111E-01 -1.535E-01 -5.758E-02  7.677E-02
-0.00400 -2.879E-01 -2.687E-01 -2.111E-01 -1.151E-01  1.919E-02
 0.00000 -3.071E-01 -2.879E-01 -2.303E-01 -1.343E-01  0.000E+00
 0.00400 -2.879E-01 -2.687E-01 -2.111E-01 -1.151E-01  1.919E-02
 0.00800 -2.303E-01 -2.111E-01 -1.535E-01 -5.758E-02  7.677E-02
 0.01200 -1.343E-01 -1.151E-01 -5.758E-02  3.838E-02  1.727E-01
 0.01600  0.000E+00  1.919E-02  7.676E-02  1.727E-01  3.070E-01

******************** X1=0.032, Y1=0.000 *************************
 X2 \Y2>    0.00000    0.00800    0.01600    0.02400    0.03200
-0.03200 -1.800E-12  7.673E-02  3.069E-01  6.904E-01  1.227E+00
-0.02400 -5.372E-01 -4.605E-01 -2.302E-01  1.534E-01  6.903E-01
-0.01600 -9.211E-01 -8.443E-01 -6.139E-01 -2.302E-01  3.068E-01
-0.00800 -1.151E+00 -1.074E+00 -8.442E-01 -4.604E-01  7.671E-02
 0.00000 -1.228E+00 -1.151E+00 -9.209E-01 -5.371E-01 -1.200E-12
 0.00800 -1.151E+00 -1.074E+00 -8.440E-01 -4.603E-01  7.670E-02
 0.01600 -9.207E-01 -8.439E-01 -6.137E-01 -2.301E-01  3.067E-01
 0.02400 -5.369E-01 -4.602E-01 -2.300E-01  1.533E-01  6.899E-01
 0.03200  0.000E+00  7.667E-02  3.066E-01  6.899E-01  1.226E+00

******************** X1=0.064, Y1=0.000 *************************
 X2 \Y2>    0.00000    0.01600    0.03200    0.04800    0.06400
-0.06400 -6.000E-12  3.062E-01  1.224E+00  2.752E+00  4.888E+00
-0.04800 -2.145E+00 -1.838E+00 -9.188E-01  6.120E-01  2.751E+00
-0.03200 -3.678E+00 -3.371E+00 -2.450E+00 -9.184E-01  1.223E+00
-0.01600 -4.598E+00 -4.291E+00 -3.370E+00 -1.837E+00  3.058E-01
 0.00000 -4.903E+00 -4.596E+00 -3.675E+00 -2.142E+00 -1.200E-11
 0.01600 -4.594E+00 -4.288E+00 -3.367E+00 -1.835E+00  3.056E-01
 0.03200 -3.672E+00 -3.366E+00 -2.447E+00 -9.170E-01  1.221E+00
 0.04800 -2.140E+00 -1.834E+00 -9.166E-01  6.106E-01  2.745E+00
 0.06400  0.000E+00  3.052E-01  1.220E+00  2.744E+00  4.873E+00

******************** X1=0.128, Y1=0.000 *************************
 X2 \Y2>    0.00000    0.03200    0.06400    0.09600    0.12800
-0.12800  0.000E+00  1.212E+00  4.843E+00  1.086E+01  1.923E+01
-0.09600 -8.517E+00 -7.296E+00 -3.641E+00  2.420E+00  1.084E+01
-0.06400 -1.462E+01 -1.339E+01 -9.724E+00 -3.636E+00  4.828E+00
-0.03200 -1.827E+01 -1.705E+01 -1.337E+01 -7.273E+00  1.207E+00
 0.00000 -1.947E+01 -1.825E+01 -1.457E+01 -8.477E+00 -1.200E-11
 0.03200 -1.822E+01 -1.699E+01 -1.333E+01 -7.251E+00  1.203E+00
 0.06400 -1.453E+01 -1.331E+01 -9.664E+00 -3.613E+00  4.798E+00
 0.09600 -8.438E+00 -7.228E+00 -3.607E+00  2.398E+00  1.074E+01
 0.12800  0.000E+00  1.197E+00  4.783E+00  1.073E+01  1.899E+01

******************** X1=0.256, Y1=0.000 *************************
 X2 \Y2>    0.00000    0.06400    0.12800    0.19200    0.25600
-0.25600 -1.800E-10  4.662E+00  1.851E+01  4.114E+01  7.187E+01
-0.19200 -3.305E+01 -2.826E+01 -1.403E+01  9.241E+00  4.087E+01
-0.12800 -5.698E+01 -5.211E+01 -3.763E+01 -1.394E+01  1.827E+01
-0.06400 -7.129E+01 -6.638E+01 -5.178E+01 -2.790E+01  4.571E+00
 0.00000 -7.574E+01 -7.084E+01 -5.626E+01 -3.242E+01 -1.200E-10
 0.06400 -7.038E+01 -6.553E+01 -5.111E+01 -2.754E+01  4.511E+00
 0.12800 -5.553E+01 -5.078E+01 -3.666E+01 -1.357E+01  1.778E+01
 0.19200 -3.179E+01 -2.718E+01 -1.348E+01  8.879E+00  3.924E+01
 0.25600  0.000E+00  4.420E+00  1.754E+01  3.897E+01  6.801E+01

******************** X1=0.512, Y1=0.000 *************************
 X2 \Y2>    0.00000    0.12800    0.25600    0.38400    0.51200
-0.51200 -2.400E-09  1.561E+01  6.028E+01  1.274E+02  2.063E+02
-0.38400 -1.160E+02 -9.839E+01 -4.756E+01  2.989E+01  1.231E+02
-0.25600 -2.040E+02 -1.850E+02 -1.302E+02 -4.611E+01  5.641E+01
-0.12800 -2.559E+02 -2.363E+02 -1.797E+02 -9.259E+01  1.416E+01
 0.00000 -2.681E+02 -2.487E+02 -1.924E+02 -1.059E+02  2.460E-09
 0.12800 -2.414E+02 -2.228E+02 -1.690E+02 -8.679E+01  1.319E+01
 0.25600 -1.808E+02 -1.637E+02 -1.147E+02 -4.031E+01  4.868E+01
 0.38400 -9.576E+01 -8.100E+01 -3.886E+01  2.410E+01  9.704E+01
 0.51200  0.000E+00  1.174E+01  4.482E+01  9.269E+01  1.444E+02
```

```
1 REM CALCULATES VELOCITY-INDUCED DRIFTS "VDRIFT"
2 SELECT PRINT 01D(72)
3 S1=600
4 R1=.001
5 PRINT
6 PRINTUSING 7,R1
7%******************* X1=#.###, Y1=0.000 ***********************
8 PRINT " X2 ";HEX(5C);"Y2>";
9 FOR Y2=0 TO R1 STEP .25*R1
10 PRINTUSING 11,Y2;:NEXT Y2:PRINT
11%     #.#####
12 FOR X2=-R1 TO R1 STEP .25*R1
13 PRINTUSING 14,X2;
14%-#.#####
15 FOR Y2=0 TO R1 STEP .25*R1
16 IF Y2<>0 THEN 18:IF X2<0 THEN 17:T1=0:GOTO 19
17 T1=#PI:GOTO 19
18 T1=#PI/2+ARCTAN(-X2/Y2)
19 R2=SQR(X2↑2+Y2↑2)
20 M1=R1*R2*COS(T1)
21 N1=R1↑2
22 N2=R2↑2
23 P=-8/3*(M1-N1)+4*N1*(M1-N1)
24 C=-4/3*(N2-2*M1+N1)+4*(M1-N1)↑2+2*N1*(N2-2*M1+N1)
25 D=4*(M1-N1)*(N2-2*M1+N1)
26 E=(N2-2*M1+N1)↑2
27 S=S1*(-3/2*P-3/2*C-21/16*D-18/16*E)
28 PRINTUSING 29,S;:NEXT Y2:PRINT
29% -#.###↑↑↑↑
30 NEXT X2:PRINT
31 R1=2*R1:IF R1<1 THEN 6
32 END
```

Figure 5-1 Wang BASIC Computer Program Used to Generate Table 5-1 tilt results in at most a drift of such-and-such?" Taking the 0.01 Hz or 3 μm criterion and assuming $R = 2m$ (a median figure for RLG's) this implies a total tilt of no more than 1.5 μ rad = 0.3 arc sec seconds! Furthermore, if we assume the mode is initially somewhat misaligned, the effect is ever stronger. From Table 5-1, if the mode is initially off by 3.2 percent of the bore radius, and aligned with $x_1 = 0.032$, $y_1 = 0$, $x_2 = y_w = 0.024$ ($r_2 = 0.034 \approx 0.032$), then a motion of 1 μm in the $-\hat{x}_2 - \hat{y}_2$ direction results in a shift change of 0.067 Hz. Clearly good initial alignment is important.

Continuing the example, suppose the PLC mirror moves $\lambda/2$ from one extreme to the other. While the direct effect upon mode position would be a motion of only about the same magnitude (< 1 μm), any accompanying tilt must be less than 1.5 μrad. If the mirror surface is 1 cm in diameter, its motion must be parallel to itself to within 5 percent.

Finally, consider the effect of thermal gradients. Suppose the RLG block to made of Cervit whose coefficients of thermal expansion we may take as typically $\alpha = 10^{-7}/^{o}C$. If the block is 3 cm thick and 10 cm long and is subjected to a $1^{o}C$ gradient from top to bottom, the mirrors will all tilt about 0.3 μrad resulting in a total mode shift of about 2.4 μm, just barely acceptable. Thus one must expect RLG's to have thermal-gradient sensitivities of the order of 0.01^{o}/hr per degree Centigrade of temperature differential across the block. Of course good engineering practice dictates mounting techniques which isolates the block from external thermal flux.

5.2 OPTICAL READOUT

In accordance with Raytheon publication ER76-4064 (Multioscillator Ring Laser, Technical and Management Proposal, 3 March 1976), Section 2.4, a concurrent design and fabrication effort for optical readout has been conducted under Raytheon funding. The results of this effort are summarized below.

In accordance with the design goal of minimizing solid intracavity elements, the readout design uses signals leaked through one of the cavity mirrors. The action of the readout is to geometrically superimpose the extensions of counterrotating intracavity beams, to discriminate the polarization states by appropriately oriented retarders and polaroid sheets, and to detect the residual signals on photodiodes. This action is accomplished in a compact assembly using a retro-prism on the back of the output mirror, a beam-splitter for dividing the power between two internal paths, and a quarter-wave plate/polaroid/diode chain in each of the divided paths. The assembly which accomplishes this is without air gaps, except between the diode cover and the diodes.

The critical fabrication items are well within the state of the art, with the possible exception of reliable control of relative intensity leaked through the output mirror coatings. It has been found desirable to control parallelism in the output mirror surfaces and orthogonality in the retro-prism to the order of about 10 arc seconds to ensure that the mixed beams will be adequately parallel. Reasonable but not precise control must be exercised over phase shifts induced by the various coatings in the readout optics. Assembly involves only one critical alignment in placing the retro-prism on the output mirror.

Various preliminary versions of the readout optics, in different degrees of compactness, have been successfully fabricated. Several fully compact versions, as described above, have been fabricated and worked satisfactorily.

SECTION 6

VERIFICATION

The RB-25-10 Multioscillator Ring Laser Gyro has been constructed, using some of the methods developed under this contract. Over 1680 hours of test data have been obtained with about 80 hours of cool down time and functional subsystem testing. The principal emphasis was on developmental testing, however some performance repeatability data was obtained over the period. A second unit, RB-25-11 has also been put into operation. This has been used principally for electronic integration testing. However, stationary performance data have been periodically obtained overnight and weekends. It shows the same performance characteristics exhibited by RB-25-10.

This section presents results from certain tests conducted at Raytheon and in some cases witnessed by independent observers. The test data presented here fall into the following categories: Scale factor linearity, warm-up trends and turn-on repeatability, and random drift.

Scale factor departure from linearity was found to be 0.6 ppm for input rates in the range between $\pm 400^\circ$/second. Warm-up trends in gyro bias for a gyro tested without thermal or magnetic protection were found to be 3°/hour with a time constant of about 10 minutes. They were consistent in sign, magnitude, and duration, and therefore easily compensated. Turn-on repeatability of gyro bias was found to be 0.05°/hour (1σ) after one hour of operation; this, again was for cases of uncontrolled thermal and magnetic environment. Random drift data demonstrated a capability of $0.003^\circ/(\text{hour})^{\frac{1}{2}}$.

Scale factor linearity points are shown in Figure 6-1 and 6-2 for different data-taking procedures. The data points for Figure 6-1 were taken by pulse accumulations for exactly one revolution of the rate table on which the gyro was mounted, the pulse counts being compensated digitally for (earth rate plus bias) as a function of time. The points plotted in Figure 6-1 are deviations from average, expressed as parts per million. The standard deviation among these points was about 2 ppm, or about 2.5 arc seconds per revolution.

Much of the variation in Figure 6-1 appears to be noise, possibly induced by the data taking procedure (i.e., non-repeatability of the rate table in reproducing the signal indicating that a full revolution had elapsed). To test this hypothesis, the data of Figure 6-2 are scale factor data for the same gyro (RB-25-10), the difference being that the counts for each point were based on ten revolutions of the rate table. The curves are clearly much smoother than those of Figure 6-1, and the standard deviation among the points was calculated to be 0.6 parts per million. We therefore conclude that, for the rate values where data were taken, Figure 6-2 is more indicative of scale factor linearity than is Figure 6-1.

Turn-on repeatability and warm-up trend data were also taken for gyro RB-25-10 over a ten-day period. The gyro electronic parameters affecting gyro output were left unchanged (except as noted below) for a number of turn-on repeatability runs. The gyro was left open to laboratory thermal and magnetic field ambients. For each run, the gyro was left off for at least one hour, and sometimes was left off overnight. Data taking was begun instantaneously at start-up. The data taken were raw data (i.e., pulses

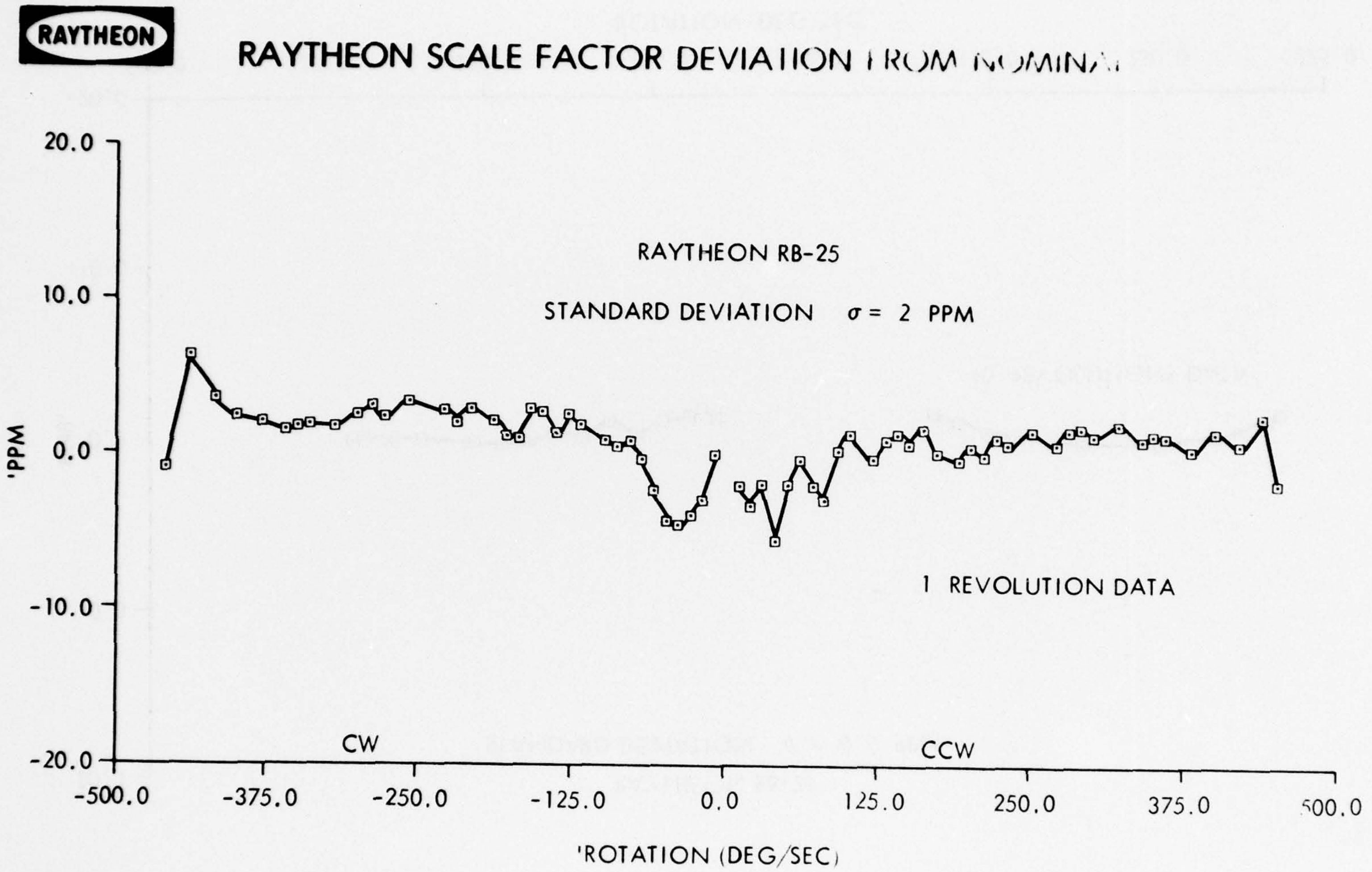

Figure 6-1 RB-25 Scale Factor Response Curve, Data Per Each Revolution

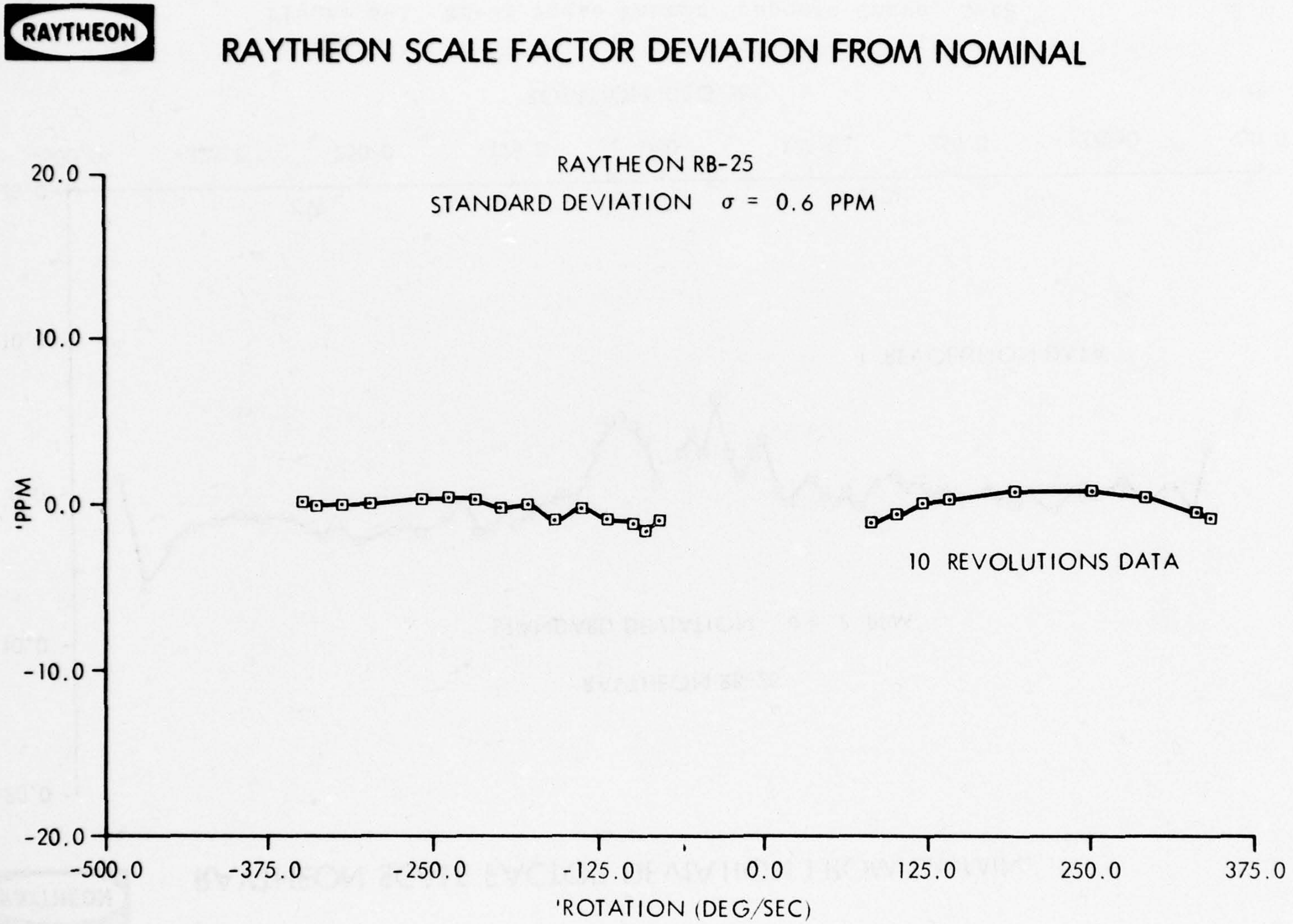

Figure 6-2 RB-25 Scale Factor Response Curve, Data per 10 Revolutions

representing the four-frequency differences) with the pre-calibrated bias removed. This bias was the same for each run (namely 28.35 pulses per second), except for three of the runs in which the anode current unbalance was set by a 60K-ohm resistor, in which case a constant bias of 17.00 pulses per second was removed. Ten turn-on repeatability runs were made in this series.

A typical warm-up trend is shown in Figure 6-3. The initial bias error of about $+3^{\circ}$ per hour was typical of all the runs, followed by a trend toward zero with about a 10-minute time constant. For each of the runs, the average drift following the warm-up transient was computed for the data between one and two hours after turn-on. The standard deviation of the biases so computed was 0.05°/hour. This number is believed to be indicative of the turn-on repeatability of the instrument at one hour after turn-on.

Data indicating the random drift capability of the RB-25 gyro are plotted in Figure 6-4. For this data we follow the customary practice of considering a series of 100-second sums. If these show no obvious trends nor point-to-point correlation, as is the case with the data of Figure 6-4, then the variations are attributed to the combined influence of quantization and random drift, from which the random drift component is readily inferred. For the set of points of Figure 6-4, the computed random drift level is $0.003^{\circ}/(\text{hour})^{\frac{1}{2}}$.

Bias stability is based on the variation of the mean value of gyro output while stationary. The individual mean values are computed using the usual one-hour sample of 100 sec sums. The standard deviation of these mean values over the duration of the

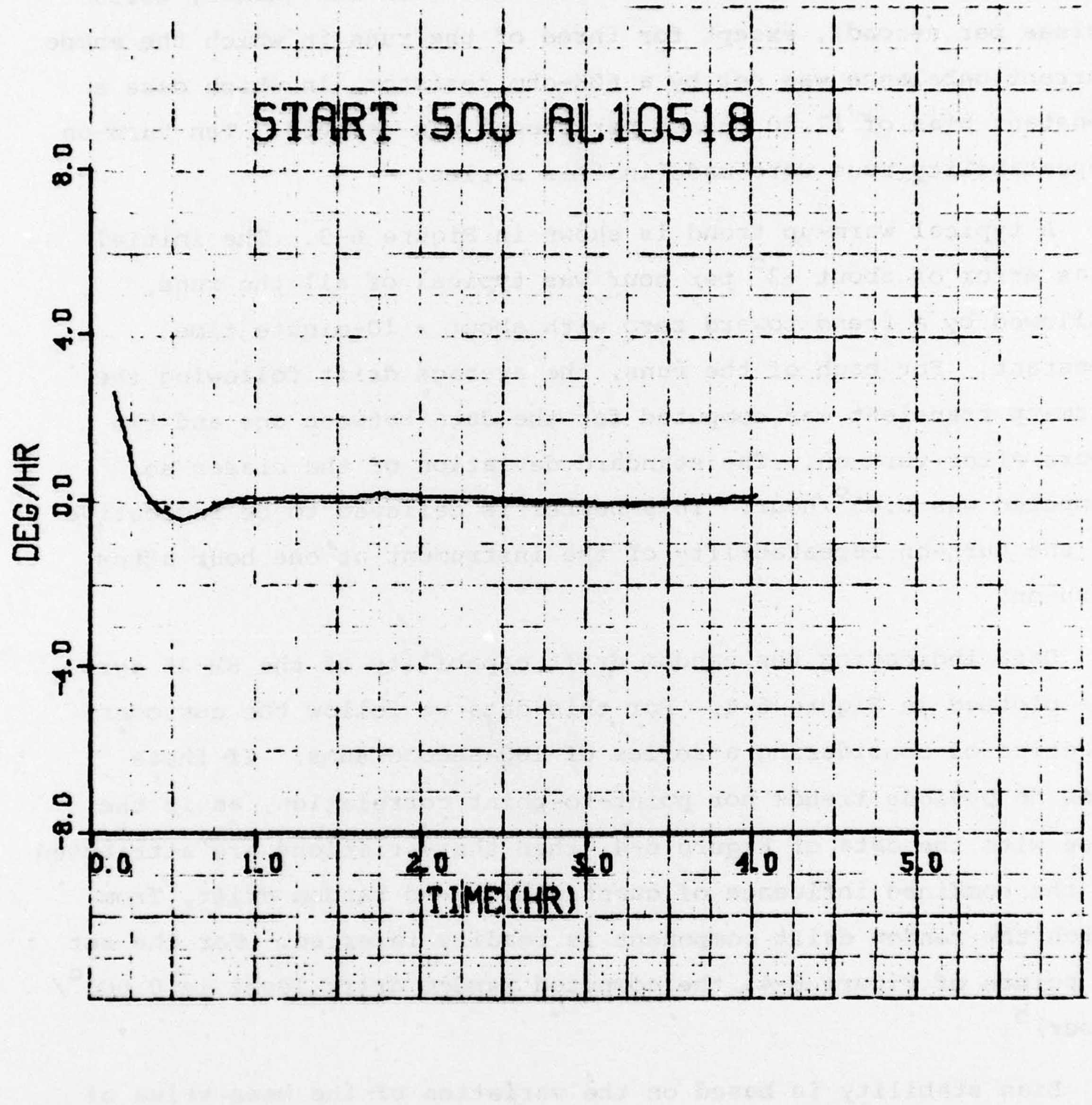

Figure 6-3 RB-25 Warm-Up Data

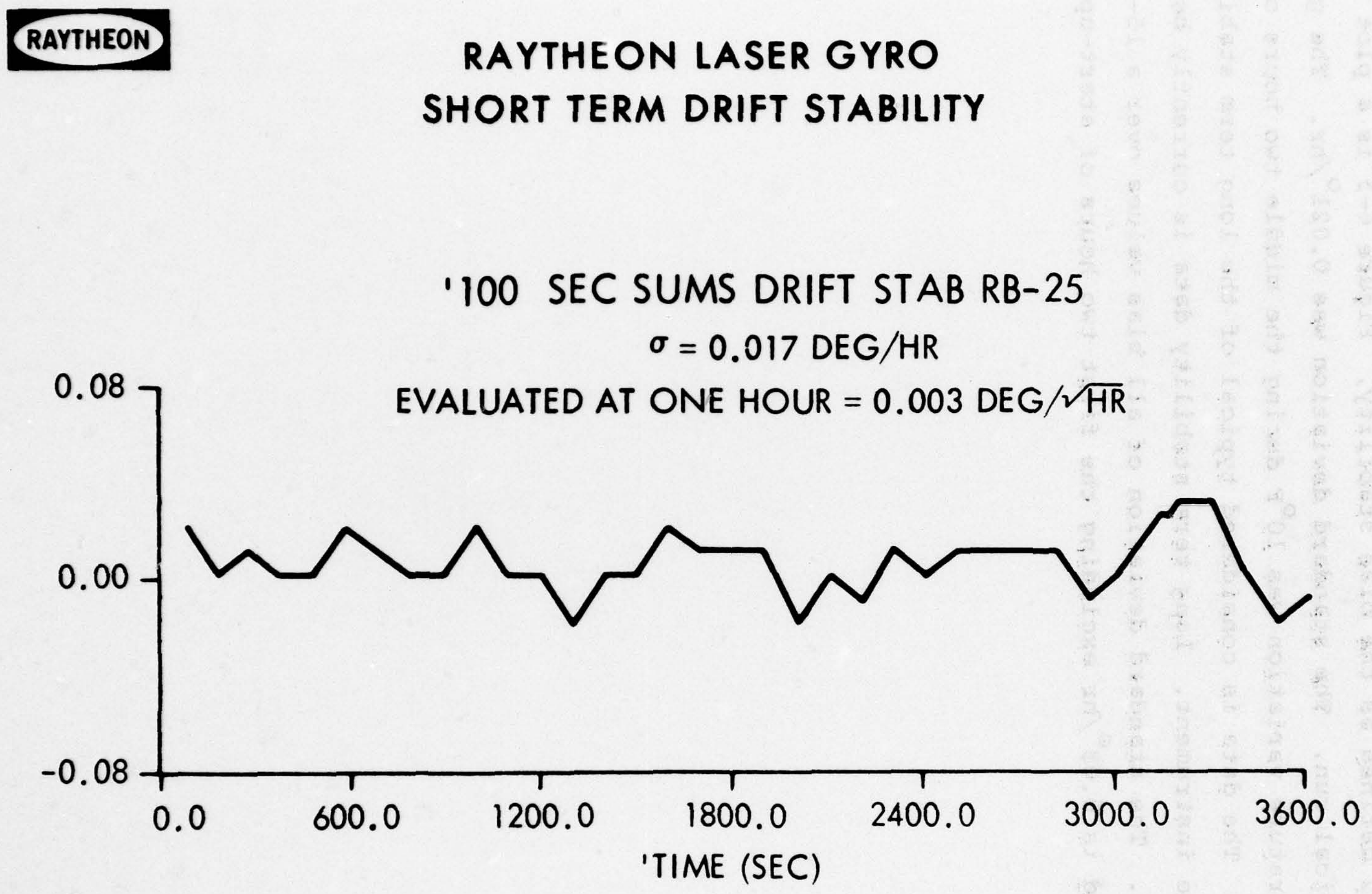

Figure 6-4 RB-25 Random Drift Data

run is defined as the bias stability. Figure 6-5 is a plot of a typical run. The standard deviation was 0.021°/hr. The gyro temperature variation was 10°F during the middle two hours of the plot. The data is considered typical of the long term stability of the instrument. Long term stability data is currently being taken. The standard deviation of all bias values over a 15-day period is 0.03°/hr excluding the first two hours of start-up.

REFERENCES

4-1 P. W. Smith and T. Hansch, Phys. Rev. Lett. 26, 740 (1971).

4-2 P. W. Smith, IEEE JQE, QE-8, 704 (1972).

4-3 P. W. Smith, IEEE JQE, QE-2, 77 (1966).

4-4 R. L. Field, Jr., Rev. Sci. Inst. 38, 1720 (1967).

4-5 W. R. Bennett, Jr., "Gaseous Optical Masers," in Appl. Optics Supp. on Optical Masers, Ed. O. S. Heavens, pp. 24-61 (1962).

5-1 I. Langmuir, J. Franklin Inst. 196, (1923).

5-2 Landau and Lifshitz, Electrodynamics of Continuous Media, p. 272 (1960).

*U.S.Government Printing Office: 1978 — 657-002/208